POLITECNICO DI MILANO
Dipartimento di Energia
Sezione di Ingegneria Nucleare – CeSNEF

Dottorato di ricerca in
Scienze e Tecnologie Energetiche e Nucleari

A NOVEL DETECTION SYSTEM FOR DIRECT AND HIGH RESOLUTION SPECTROMETRY OF INTENSE NEUTRON FIELDS

Tesi di Dottorato di:
Michele LORENZOLI

Relatori: Dott. Andrea POLA
Prof. Alberto FAZZI
Tutor: Prof. Stefano AGOSTEO

Coordinatore: Prof. Carlo Enrico BOTTANI

XXVI ciclo 2011 – 2013

CONTENTS

INTRODUCTION

Neutron spectrometry has contributed to the development of nuclear physics since the discovery of neutron in 1932, and has also become an important tool in several other fields, notably nuclear technology, fusion plasma diagnostics, radiotherapy and radiation protection.

Most neutron spectrometers used nowadays are based on methods that were introduced before 1960, like recoil-nuclei spectrometers or Time-of-Flight methods, while other important techniques as Bonner spheres were developed in the 1960-1979 period. After the 1980 the impact of computers on neutron spectrometry has improved this research field as a result of the comprehensive methods of calculation that are now available, firstly to generate the response functions or to calculate the neutron detection efficiency of the detector system, e.g. by Monte Carlo simulation, and secondly to unfold the spectral neutron fluence from the spectrometer readings.

Chapter I presents a review of the present status of neutron spectrometry, including a recoil spectrometer for low-energy neutron fields based on a monolithic silicon telescope coupled to a polyethylene converter, studied by Agosteo et al.

The aim of this PhD Thesis is to study, develop and characterize an innovative system compact, transportable and able to perform real-time neutron spectrometry with high resolution. At the present status, no proposed instruments are able to combine these characteristics.

The spectrometer proposed by this work is based on the recoil-proton detection methodology, but with a completely innovative geometrical structure and data processing which allow to obtain a direct measurement of the impinging neutron fields.

The device is composed by a plastic scintillator and a residual energy measurement stage constituted by a monolithic silicon telescope (MST). The scintillator works as an “active” converter, which converts neutrons into recoil-protons via elastic scattering and measure the energy loss of the recoil-protons inside the converter itself at the same time, while the silicon device measures the residual energy protons have at the outer converter interface and effectively discriminate them from photons associated to the neutron field.

The first step of the development was the design of the system structure and the study of its performances in terms of response function features. To do this, a detailed analytical model was developed and used to derive the best detection geometry of the system. The model and its results are presented in Chapter II.

The main feature of the system layout is the introduction of the “active” converter. In order to study the best device which permits to do so by keeping the whole detecting system as compact as possible, two different solutions were studied (Chapter III): a compact commercial photomultiplier tube (PMT) and a silicon photomultiplier (SiPM).

Chapter IV describes the overall optimized layout of the spectrometer, as well as the experimental layout and the calibration procedure, while Chapter V presents the dedicated LabVIEW software developed to acquire and process the data related to the three stages of the device in order to calculate in real-time the neutron spectra.

The complete Active Converter Spectrometer was characterized with mono-energetic neutrons and tested with multi-peak continuously distributed neutrons fields. The irradiations were performed at the Van De Graaff accelerator of the INFN-Laboratori Nazionali di Legnaro (Legnaro, Italy). The spectra obtained with the spectrometer were compared with Time-of-Flight literature data and simulated distributions. The results of irradiations and comparisons are proposed in Chapter VI.

Chapter I

NEUTRON SPECTROMETRY: PRESENT STATUS

Methods of neutron spectrometry [1] can be classified into several groups based on the principle used to obtain neutron energy: methods based on measurements of the energies of charged particles released in neutron-induced nuclear reactions; methods in which the neutron velocity is measured; threshold methods, in which a minimum neutron energy is indicated by the appearance of a neutron-induced effect such as radioactivity, a specific gamma-ray energy or a phase transition; methods in which the neutron energy distribution is determined by unfolding a set of readings of different detectors or of different detector geometries which differ in the energy-dependence of their response to neutrons; methods in which the neutron is scattered and the energy of a recoiling nucleus is measured.

I.1 Neutron time-of-flight methods

In this technique neutron energy is determined by measuring the neutron flight time over a known distance. Two methods are typically used to do this. In the first method the neutron is scattered in a start detector, for example an organic scintillator, and the time of flight to a second detector positioned at a known distance and angle is measured. In the second method the start signal is provided by an associated particle or quantum that is emitted from the neutron source at the same time as the neutron.

The associated particle time-of-flight method has been employed, for example, to measure the spectrum of neutrons from the spontaneous fission of ^{252}Cf [2,3] or to characterize neutron time-of-flight detectors [3,4]. The scatter detector method has been used in neutron scattering studies and to measure neutrons emitted from nuclear reactions and nuclear fusion [5-9].

Fig.I.1 shows a schematic view of a typical time-of-flight system.

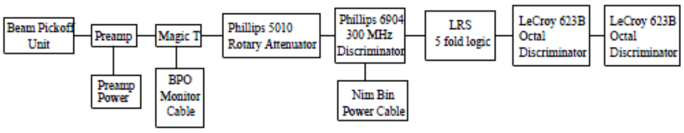

Beam Pickoff Electronics

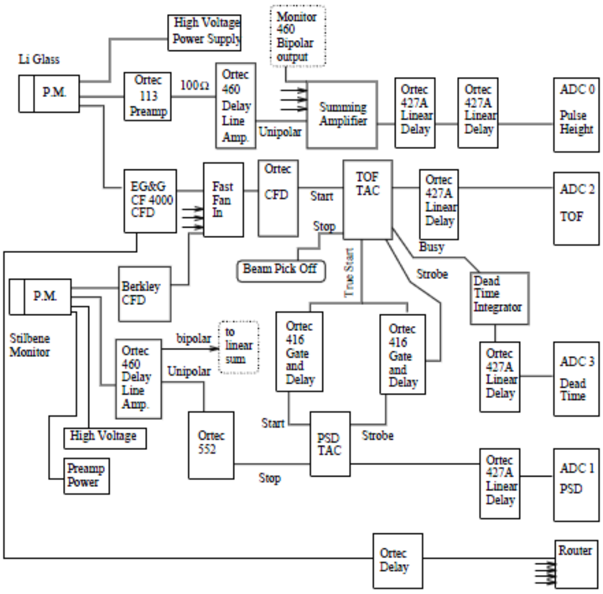

Li Glass Electronics

Fig.I.1: Schematic view of a time-of-flight system [10].

I.2 Multisphere systems

The prototype multisphere system, known as the Bonner Sphere Spectrometer (BSS), was the neutron spectrometer introduced by Bramblett, Ewing and Bonner [11]. The original BSS comprised a small thermal neutron detector (cylindrical ^{6}LiI(Eu) crystal, 4 mm in diameter and x 4 mm in height), positioned in the centre of a polyethylene sphere. Five spheres of different diameters between 2 and 12 inches were used to produce five detector geometries with distinctively different response functions.

The BSS can determine neutron spectra over a wide energy range but with relatively poor energy resolution. A neutron spectrum is derived by measuring the detector count rate with sphere geometries and then unfolding these measurements using the associated response matrix. Bonner sphere spectrometers are widely used in radiation protection applications.

An innovative approach among new designs that have evolved from the BSS consists of using a spherical moderator containing several passive thermal neutron detectors [12], or a number of small active thermal neutron detectors [13-16] placed at a proper position. The position of neutron detection then replaces the sphere diameter as a variable in the response matrix and all measurements are made simultaneously.

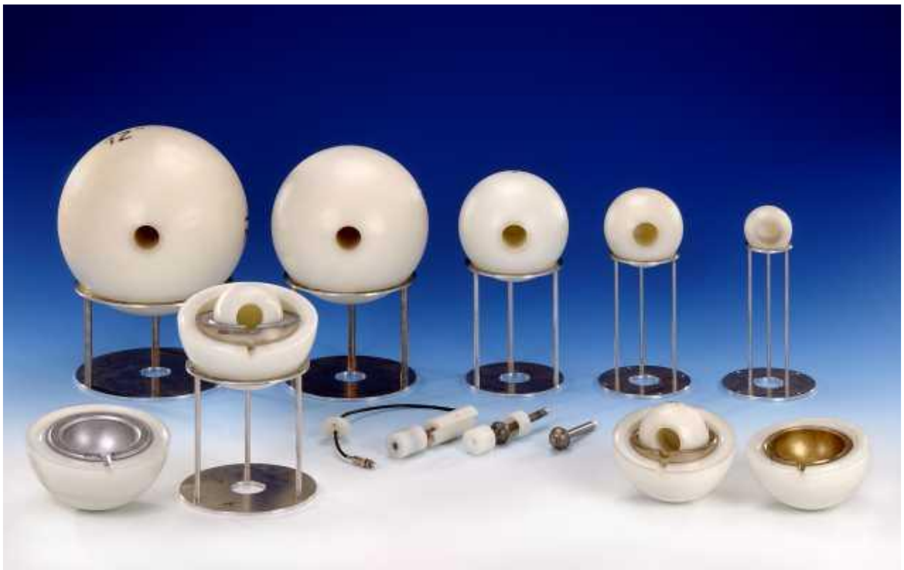

Fig.I.2: The Bonner sphere spectrometer NEMUS (NEutron MUltisphere Spectrometer) [17-18].

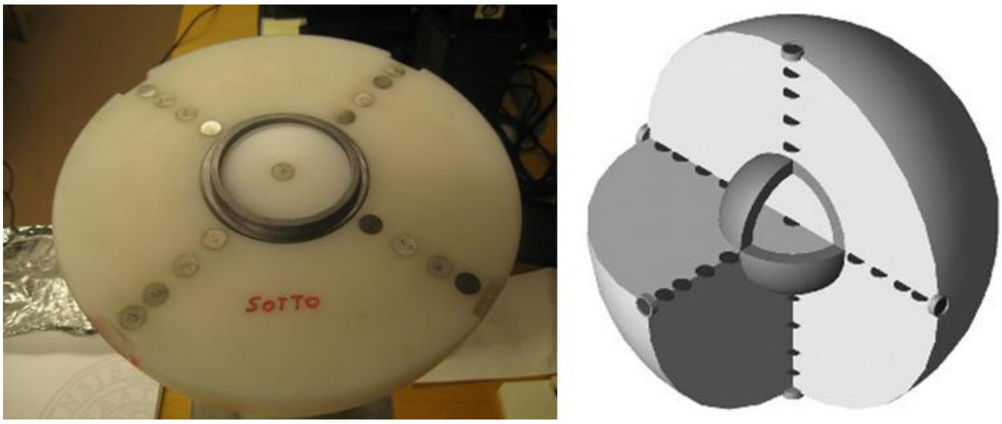

Fig.I.3: The multidetector neutron SPherical SPectrometer (SP^2) [14-16].

I.3 Spectrometry of recoil nuclei

Recoil spectrometers are either detectors in which recoil nuclei emitted at all angles with respect to the incident neutron direction are accepted for measurement, or recoil telescopes, in which recoils at a particular angle (preferably 0°) are selected for analysis. The spectrometer response function (pulse height spectrum of secondaries resulting from bombardment with monoenergetic neutrons) is typically a broad continuum for the former category and a narrow function for the latter one. Recoil nuclei spectrometers based on proportional counters are widely used in the energy range 50 keV to a few MeV [19-21]. Pulse height resolution varies chiefly as the square root of the recoil nucleus energy and is typically about 10% (FWHM) for 1 MeV recoil ions. For neutron energies above about 5 MeV proton escape (wall effect) limits the usefulness of proton recoil proportional counters. Although ^{4}He recoil devices can extend the energy range upwards (to about 15 MeV), organic scintillators are usually the preferred detector medium for spectrometers at higher energies [22,23], in particular stilbene crystals and liquid scintillators, due to their capability of discriminating between neutron and photon events by pulse-shape analysis. The response functions of these detectors are dominated by n–p elastic scattering in this energy range. Since the n–p cross-section is well-known, response matrices and detection efficiencies can be computed accurately and neutron spectra can be reliably unfolded from measured pulse height spectra. Charged particles produced by neutron interactions with the carbon nuclei in the scintillator give significant contributions to the response functions of organic scintillators at incident neutron energies above about 8 MeV, but are adequately accounted for in simulated response functions for energies up to about 15 MeV [23]. For higher incident energies [5,24-26] to simulate these contributions becomes increasingly difficult because the cross-section data that are required are either not available or not accurate enough. Moreover the generation of recoils which do not fully stop in the scintillator affects the n/γ-discrimination.

Ideally a narrow response function to monoenergetic neutrons should be the desired for neutron spectrometers. A wide variety of designs have been proposed to do this. Recoil telescopes can provide simple response functions but the price of doing that is usually a very low neutron detection efficiency, typically <0.01%. Another approach that is used to achieve a simple response function is the capture-gated neutron spectrometer [27-

32]. This is a recoil detector spectrometer, usually a liquid or plastic scintillator, which selects events in which neutrons transfer all their energy by elastic and inelastic scattering within the scintillator. A delayed coincidence between the summed pulse height signal and the subsequent (0.2–50 ms) signal due to capture of the neutron after moderation to a low energy (<10 eV) is required. Neutron capture is detected by doping the organic scintillator (liquid or plastic) with ^{10}B or ^{6}Li, or by incorporating a separate low-energy neutron detector in the system. The neutron energy is obtained from the summed pulse height signals which in general generate a broad distribution (FWHM ~50%). Detection efficiencies of about 10% are achievable.

I.4 A recoil-proton spectrometer based on a monolithic silicon telescope

A monolithic silicon telescope coupled to a polyethylene converter was studied by Agosteo et al. [33,34] as a recoil-proton spectrometer for low-energy neutron fields. The device consists of a surface ΔE stage, about 2 μm in thickness, and an E stage, 500 μm in thickness, made out of a single silicon wafer. The sensitive area of the detector is about 1 mm^2. The two stages share a deep electrode obtained through an high-energy boron implantation [35].

The neutron spectrometer is assembled by placing a 1 mm thick polyethylene layer in contact with the ΔE stage of the monolithic silicon telescope. This device accomplishes the role of detecting the recoil-protons generated in the converter by neutrons through elastic scattering. The spectra acquired by the silicon detector correspond to the distribution of energy deposited within the sensitive volume by recoil-protons only (apart from the secondary electrons generated by background photons interacting with the detector assembly).

Since the ΔE stage measures a LET-related quantity, the acquisition of the time-correlated distribution of events which deposit an energy ΔE in the ΔE stage and a total energy E_{TOT} in the whole detector (the so called ΔE- E_{TOT} scatter plot) allows a particle-related event discrimination.

As an example, a typical ΔE–E_{TOT} scatter plot obtained by irradiating with neutrons generated through the bombardment of a thick beryllium target with 5 MeV protons is shown in Fig.I.4. The distribution is characterized by three different populations: 1) recoil-protons capable of reaching the E stage, which give rise to events at high $E_{\Delta E}$ and E_{TOT} values (black solid arrow); 2) secondary electrons generated by photons associated with the neutron field, which are concentrated at low $E_{\Delta E}$ and E_{TOT} values (grey solid arrow); 3) recoil-protons stopping in the ΔE stage, for which $E_{\Delta E}$ must be equal to E_{TOT} (black dashed arrow).

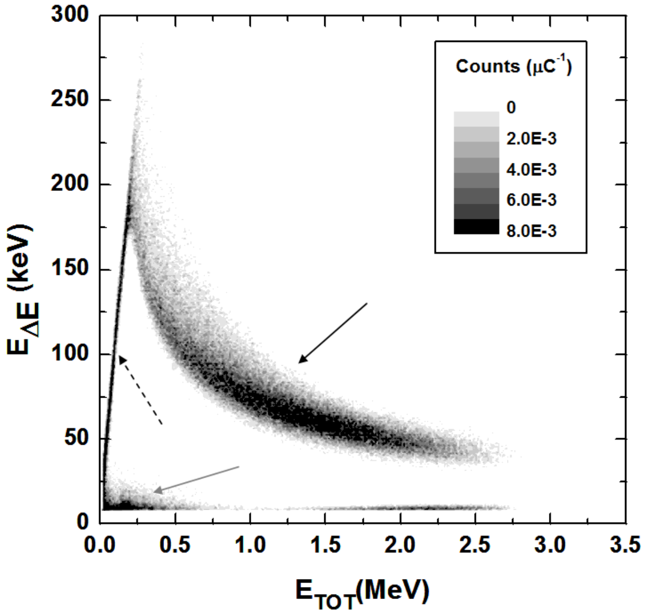

Fig.I.4: ΔE-E_{TOT} scatter plot obtained by irradiating with neutrons generated by 5 MeV protons striking a thick-beryllium target [34].

The neutron fluence spectral distributions are reconstructed with an unfolding algorithm based on a non-linear least-squares method. The response matrix was calculated by using an analytical model developed by Agosteo and Pola [36]. The initial guess for the iterative unfolding procedure is uniform in energy. The results are compared with the data obtained by Howard et al. [10] with time-of-flight techniques (ToF) in Fig.I.5.

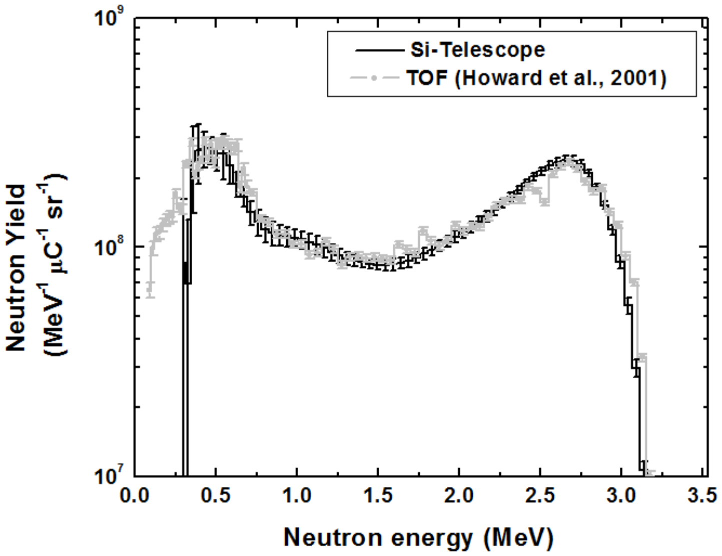

Fig.I.5: Distributions of neutron yield (5 MeV protons on Be), comparison with the work by Howard et al. [10,34].

The aim of the research activity carried out in the framework of this PhD thesis was to develop a simple and compact device able to perform real-time neutron spectrometry with high resolution. The instruments described in the previous paragraphs do not allow to reach this objectives. TOF systems are typically very large and complex. On the other hand, the multisphere and recoil nuclei devices need the use of dedicated unfolding procedures to obtain neutron spectra, and these i) limit the simplicity, ii) deteriorate their energy resolution and iii) prevent the possibility of a real-time measurement of neutron spectra

In order to achieve the research goals, a new design for an active converter spectrometer based on the recoil-proton method has been studied, as described in the next chapters.

Chapter II

ANALYTICAL MODEL AND FEASIBILITY STUDY

The aim of this PhD Thesis is to study, develop and characterize an innovative system compact, transportable and able to perform real-time neutron spectrometry with high resolution.

The first step of the research activity was the design of the system structure and the study of its performances in terms of response function features. To do this, a detailed analytical model was developed and used to derive the best detection geometry of the system proposed.

The numerical study based on the analytical model led to a new spectrometer based on the recoil-proton spectrometry technique, but with a completely innovative geometrical structure and data processing which allow to performed a real-time characterization of neutron fields.

The detection system consists of a plastic scintillator coupled to a photomultiplier and a residual energy measurement stage constituted by a monolithic silicon telescope (MST). The scintillator acts as an “active” converter while the silicon device measures the residual energy protons have at the outer converter interface and effectively discriminate them from photons associated to the neutron field.

II.1 Spectrometer Design

The detection system already proposed in literature by Agosteo et al. consisted of a MST directly coupled to a polyethylene layer 1 mm thick (Fig.II.1). As mentioned in Chapter 1, the silicon device is a device characterized by a dead layer of titanium (about 0.24 µm thick), a thin ΔE stage (about 2 µm thick), and a 500 µm thick E stage.

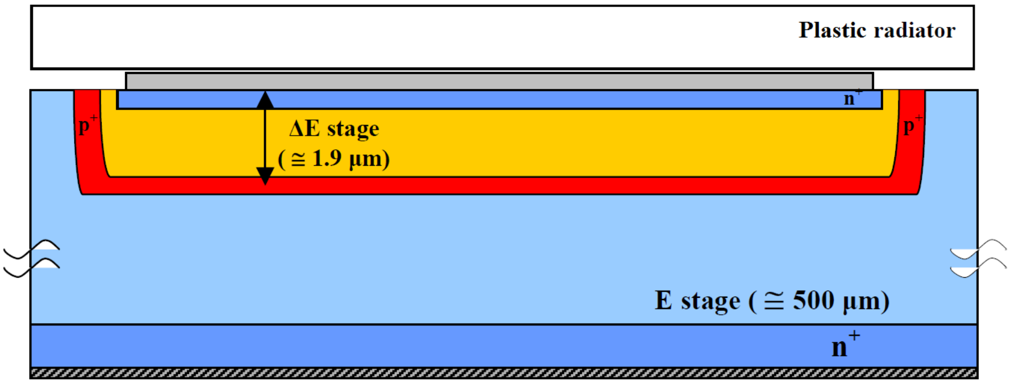

Fig.II.1: The Monolithic Silicon Telescope coupled with a plastic layer.

The role of the MST was to measure the distribution of the residual energy of recoil-proton generated at all emission angles by the neutron field via elastic scattering in the polyethylene radiator. The term residual refers to the attenuation process that protons undergo before exiting the radiator.

Generally, for a neutron of energy E_n, the energy transferred to a nucleus of mass A through an elastic collision is given by:

$$E_{RN} = \frac{4A}{(A+1)^2} \cdot cos^2(\theta) \cdot E_n \, , \tag{II.1}$$

where θ is the scattering angle of the recoil-nucleus with respect to the neutron direction of incidence in the laboratory system.

As mentioned, recoil-protons are attenuated inside the converter, so part of the information about their starting energy is lost. The first solution proposed consists in replacing the plastic converter with a plastic scintillator, i.e. a polyvinyltoluene-based scintillator. By doing that it is possible to measure the energy lost in the converter. By summing this energy to the one measured by the silicon detector, the total recoil-proton energy can be calculated.

From equation (II.1), we can obtain the recoil-proton energy by assuming A=1 so that:

$$E_p = E_n \cdot cos^2(\theta). \qquad \text{(II.2)}$$

Then, by measuring the recoil-proton energy at all emission angles, the obtained spectrum is distributed from 0 to the neutron energy E_n, making necessary the use of unfolding procedures. In order to reduce the distribution to a narrow peak response, it is necessary to reduce the emission angle range. Therefore, the second solution proposed is to move the converter far from the silicon detector. In order to avoid the attenuation of recoil protons in the air gap created between the scintillator and the MST, the system must work in vacuum.

II.2 Particle trajectory and energy deposition

The analytical approach described in the following is based on the energy-range and energy-stopping power relations taken from ICRU 49 report [37] and SRIM code [38,39].

The model, based on that proposed by Agosteo and Pola [36,40-41], calculates the energy deposited in all stages of the system by recoil protons set in motion in the converter by the neutron field. Fig.II.2 shows a sketch of the detection geometry of the model. The original version of the model was developed for the configuration with the converter placed in contact with the telescope (distR equal to 0).

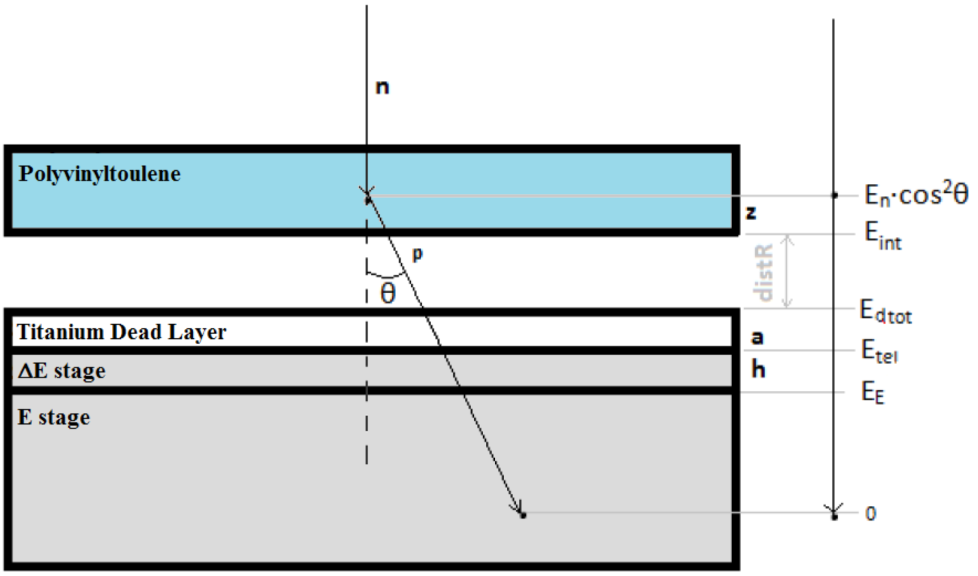

Fig.II.2: Interaction geometry for a neutron with energy E_n [42].

Recoil-protons must exit the polyvinyltoluene converter, cross the titanium dead layer, reach the ΔE stage and possibly enter the E stage. The chance of reaching the ΔE stage depends both on geometry and energy deposition.

From a starting position inside the converter (x,y,z), by defining L_{riv} the half of the detector side, the recoil-proton has to enter the titanium layer with coordinates $|X_{riv}|$ and $|Y_{riv}|$ both less than L_{riv}, where:

$$\begin{aligned} X_{riv} &= x + (z + distR + a) \cdot tg(\theta) \cdot cos(\varphi) \\ Y_{riv} &= y + (z + distR + a) \cdot tg(\theta) \cdot sin(\varphi) \ , \end{aligned} \tag{II.3}$$

being θ and φ the recoil-proton emission angles and a the dead layer thickness (Fig.II.3).

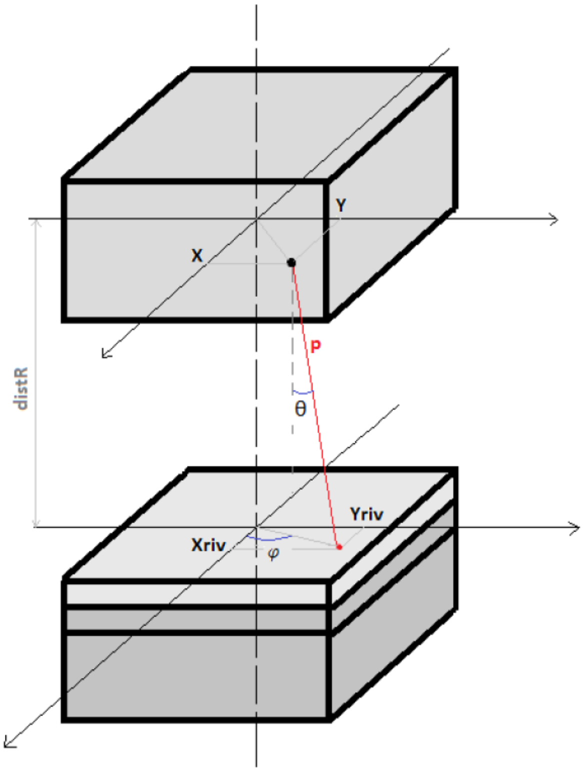

Fig.II.3: Interaction geometry: 3D description of the recoil-proton trajectory [42].

As indicated in (II.2) the recoil-proton is set in motion with $E_p = E_n \cdot \cos^2(\theta)$. It must start from a depth z lower than $R^{poly}(E_p) \cdot \cos(\theta)$ in order to have an energy sufficient to exit the polyvinyltoluene converter.

The projected range $R^{poly}(E_{int})$ of the recoil proton at the converter-MST interface is then the difference between the initial range and the traveled distance:

$$R^{poly}(E_{int}) = R^{poly}(E_n \cdot cos^2(\theta)) - \frac{z}{cos(\theta)} \,. \tag{II.4}$$

By inverting the range-energy relation, the energy E_{int} can be obtained:

$$E_{int}(\theta, z) = E^{poly}\left(R^{poly}(E_n \cdot cos^2(\theta)) - \frac{z}{cos(\theta)}\right), \tag{II.5}$$

and the energy deposited in the converter is:

$$E_{conv}(\theta, z) = E_n \cdot cos^2(\theta) - E_{int}(\theta, z) \,. \tag{II.6}$$

The analytical model proposed in this work has been modified in order to take into account also the air volume between the converter and the silicon telescope. To reach the titanium dead layer, the proton must have $R^{Air}(E_{int}) > \frac{distR}{cos(\theta)}$. By using the same procedure as for the previous layer, the residual range and energy in air are:

$$R^{Air}(E_{dtot}) = R^{Air}\big(E_{int}(\theta,z)\big) - \frac{distR}{cos(\theta)}\,, \tag{II.7}$$

$$E_{dtot}(\theta,z) = E^{Air}\left(R^{Air}\big(E_{int}(\theta,z)\big) - \frac{distR}{cos(\theta)}\right). \tag{II.8}$$

Since, to be revealed, the proton must cross the titanium dead layer and release energy inside the ΔE stage, the range in titanium must be $R^{Ti}(E_{dtot}) > \frac{a}{cos(\theta)}$. The range and energy of the exiting proton are then:

$$R^{Ti}(E_{tel}) = R^{Ti}\big(E_{dtot}(\theta,z)\big) - \frac{a}{cos(\theta)}\,, \tag{II.9}$$

$$E_{tel}(\theta,z) = E^{Ti}\left(R^{Ti}\big(E_{dtot}(\theta,z)\big) - \frac{a}{cos(\theta)}\right). \tag{II.10}$$

A proton reaching the ΔE stage is revealed by the telescope, regardless of its ability to reach the E stage. The residual proton range and energy after the ΔE stage are:

$$R^{Si}(E_E) = R^{Si}\big(E_{tel}(\theta,z)\big) - \frac{h}{cos(\theta)}\,, \tag{II.11}$$

$$E_E(\theta,z) = E^{Si}\left(R^{Si}\big(E_{tel}(\theta,z)\big) - \frac{h}{cos(\theta)}\right). \tag{II.12}$$

The (II.11) and (II.12) are valid for protons which cross the ΔE stage (“crossers”). If the recoil-proton range after the dead layer is $R^{Si}(E_{tel}) \leq \frac{h}{cos(\theta)}$, it stops in the ΔE stage (“stoppers”), and E_E is equal to 0. In both cases, the energy released in the ΔE stage is:

$$E_{\Delta E}(\theta,z) = E_{tel}(\theta,z) - E_E(\theta,z). \tag{II.13}$$

II.3 Neutron interaction probability in the radiator

The simulations described in the following paragraph are calculated by normalizing the neutron distributions to a single neutron interaction. Therefore, for a quantitative evaluation of the fluence response functions, these distributions must be multiplied by the probability $\pi(E_n)$ of generating a recoil-proton in the polyvinyltoluene radiator per unit neutron fluence. This probability must take into account the attenuation of the neutron field inside polyvinyltoluene, which increases for decreasing neutron energies.

The probability $\pi(E_n)$ was calculated by assuming the exponential attenuation of the neutron fluence and neglecting multiple scattering. By integrating the probability of undergoing an interaction with hydrogen nuclei per unit path length over the layer of interest, the following expression derives:

$$\pi(E_n) = A \cdot \int_{L-R^{poly}(E_n)}^{L} e^{-\Sigma_{tot} \cdot x} \cdot \Sigma_H \cdot dx\ , \qquad \text{(II.14)}$$

where A is the detector sensitive area, L is the thickness of the polyvinyltoluene layer (2 mm), Σ_H is the macroscopic cross section of hydrogen, Σ_{tot} is the total macroscopic cross section (hydrogen plus carbon) at the energy E_n and R^{poly} (E_n) is the maximum range in polyvinyltoluene of recoil-protons, i.e. the thickness of the layer of interest.

II.4 Monte Carlo simulations

The analytical model described in Paragraph II was used for the analytical calculation of the spectrometer response functions. It should be underlined that Monte Carlo method was used to calculate numerically the integrals of the model.

For each neutron event, the energy of the particle is sampled from a given distribution, taking into account the neutron scattering probability. The coordinates x and y are sampled from uniform distributions inside the converter area (both rectangular and circular area models were implemented), while the z coordinate is sampled from a uniform distribution between 0 and $R^{Poly}(E_n)$.

The scattering angle φ is sampled from a distribution between 0 and 2π.

Below 10 MeV, only s-wave neutrons can interact with the nucleus, and the scattering angular distribution can be considered isotropic in the center-of-mass system.

In the laboratory system, recoil-protons are distributed uniformly from θ = 0° to θ = 90° in each [d $\cos^2\theta$] element. Since the recoil-proton energy E_p is given by $E_n \cdot cos^2(\theta)$ (II.2), the uniform distribution of $\cos^2(\theta)$ corresponds to the uniform distribution of E_p.

Since:

$$pdf(cos^2\theta)d\,cos^2\theta = pdf(\theta)d\theta, \qquad \text{(II.15)}$$

$$pdf(\theta) = pdf(cos^2\theta)\frac{d\,cos^2\theta}{d\theta} = 2\cdot sin\,\theta, \qquad \text{(II.16)}$$

it is possible to sample the angle θ:

$$cdf(\theta) = \int_0^\theta 2\cdot sin\,\theta' d\theta' = \frac{1-cos\,2\theta}{2}. \qquad \text{(II.17)}$$

From the six quantities energy, starting coordinates, θ and φ, the arrival point of the proton and the deposited energies are calculated. Protons which do not reach the ΔE stage are discarded.

II.5 Results

The system was firstly simulated in the classical configuration, with the plastic converter close to the MST. Starting from a monoenergetic source, the effect of the scattering reaction together with the energy loss of the proton inside the converter lead to a broad continuum response of the silicon detector, with energy between 0 and En (see Fig.II.4 and Fig.II.5).

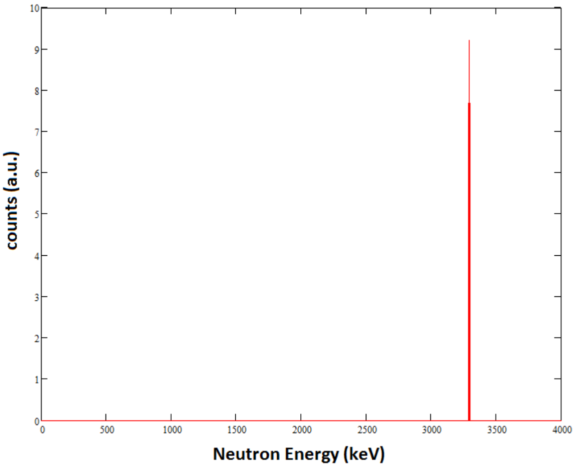

Fig.II.4: Source: monoenergetic neutrons of 3.31 MeV.

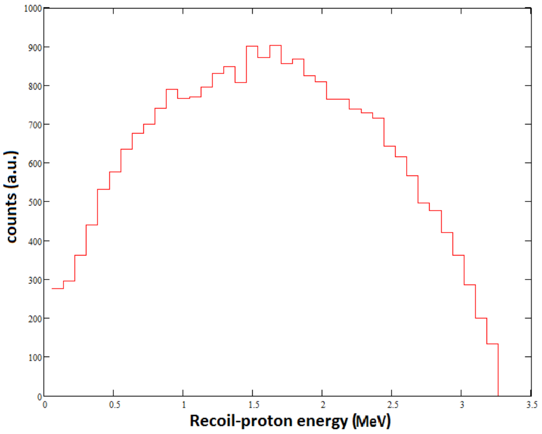

Fig.II.5: Response of the silicon detector to monoenergetic neutrons of 3.31 MeV.

The energy deposited by the proton in the converter was then summed to the one measured by the silicon detector in order to calculate the total recoil-proton energy.

As shown in Fig.II.6, a quasi-triangular distribution is obtained, with a maximum value which correspond to the impinging neutron energy. The broadening of this distribution is due to the angular distribution of the recoil proton (II.2).

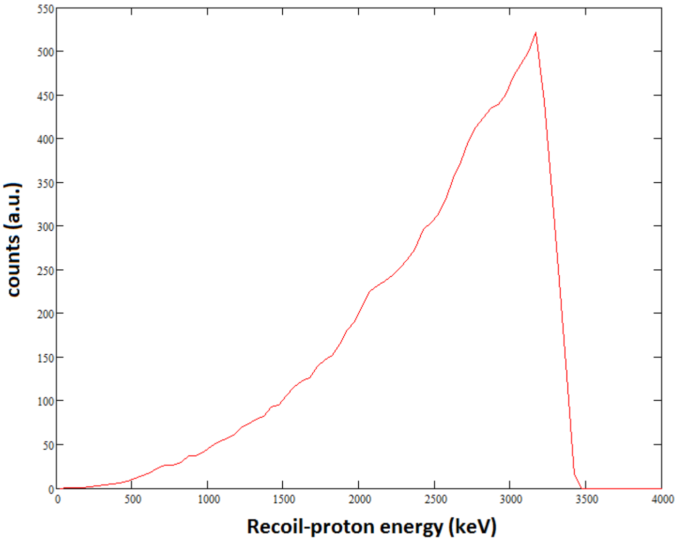

Fig.II.6: 3.31 MeV neutrons: distribution of the sum of the energy deposited in the converter and that released in the silicon detector.

In order to reduce this distribution to a narrow peak response, the second idea was implemented by separating the converter from the silicon detector and by considering the gap between to the made of vacuum.

The calculated distributions show the effect that moving the converter far from the silicon detector has on the width of the response function. At a distance of 20 mm, corresponding to an emission angle $\theta_{max} \approx 7°$, the response results to have an energy width of ~50 keV FWHM.

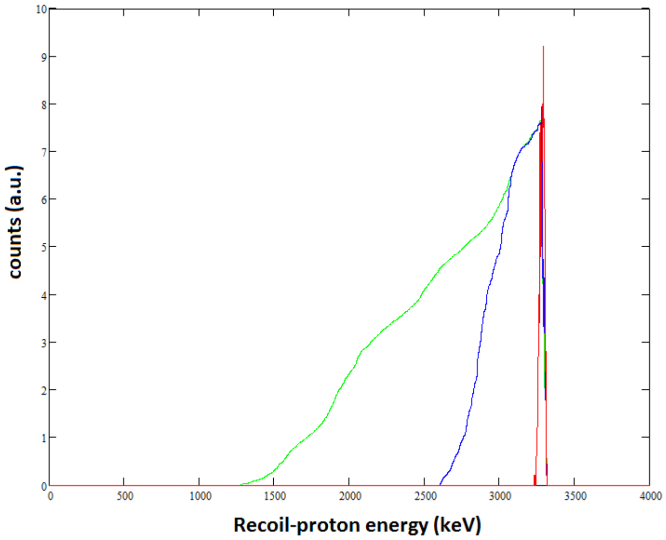

Fig.II.7: 3.31 MeV neutron source: distribution of the sum of the energy deposited in the converter in the silicon detector at a converter –MST distance of 5 mm (green), 10 mm (blue) and 20 mm (red).

Fig.II.8, Fig.II.9 and Fig.II.10 show the calculated spectra of the energy deposited by recoil-protons in the converter energy, ΔE stage deposition and total deposition in the MST respectively.

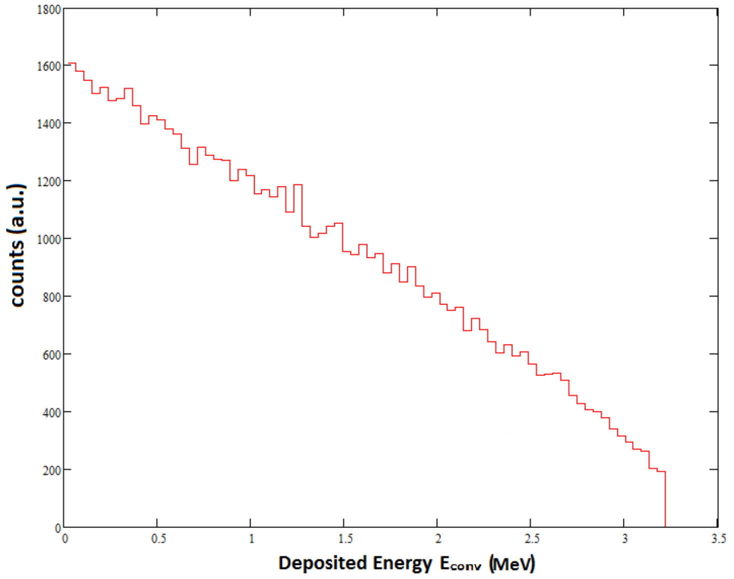

Fig.II.8: Spectrum of the energy deposited in the converter for 3.31 MeV neutrons.

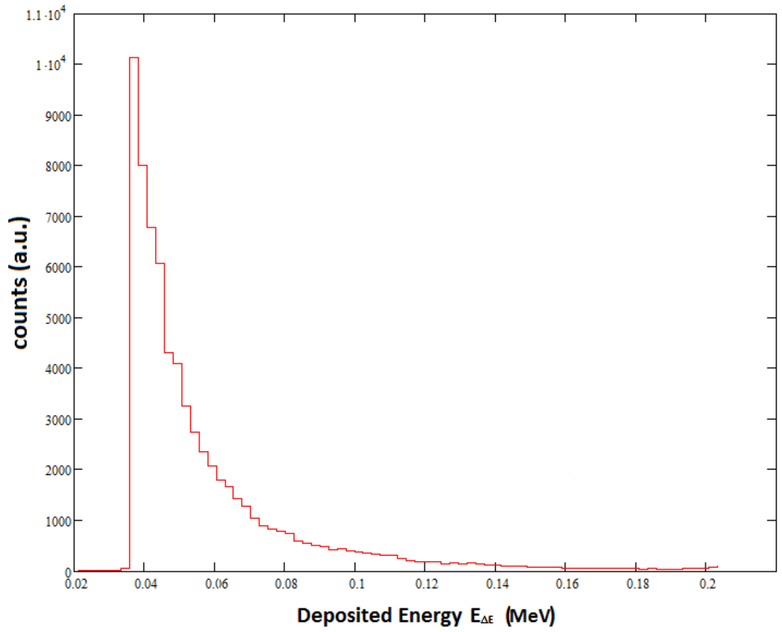

Fig.II.9: Spectrum of the energy deposited in the ΔE stage for 3.31 MeV neutrons.

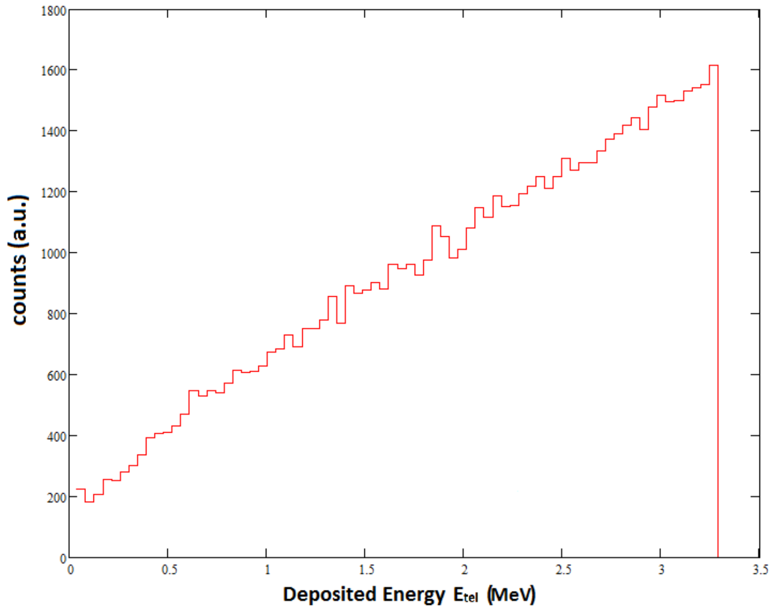

Fig.II.10: Spectrum of the total energy deposited in the whole MST for 3.31 MeV neutrons.

Fig.II.11 shows the scatter plot of the energy $E_{\Delta E}$ deposited in the ΔE stage and that released in the whole telescope E_{tel}. At lower energies all protons are stoppers and $E_{\Delta E}$ = $E_{tel.}$ Therefore the distribution follows a straight line of unit slope. At energies higher than about 200 keV protons cross the ΔE stage and the scatter plot assumes the trend shown.

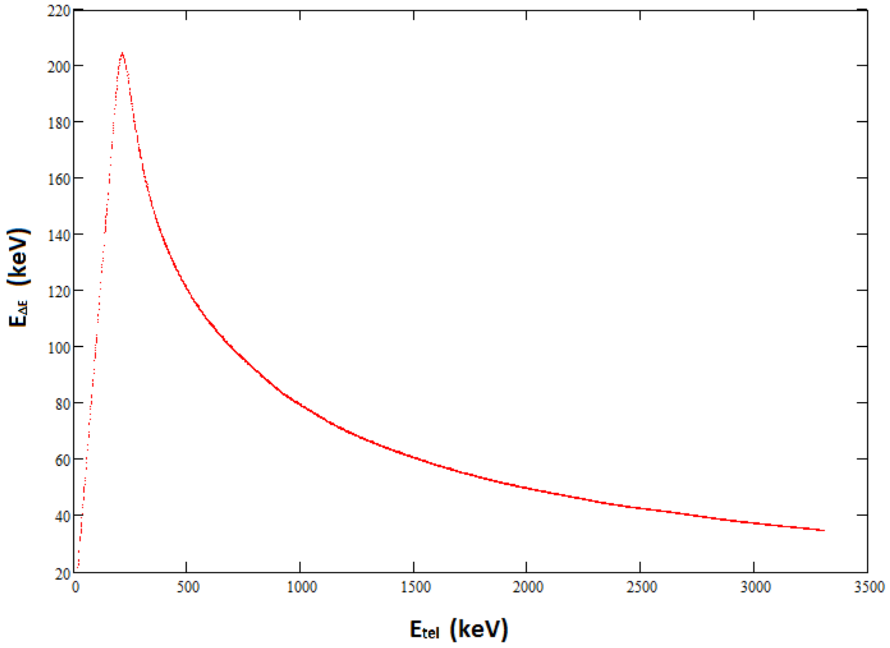

Fig.II.11: $E_{\Delta E}$-E_{tel} Scatter plot for 3.31 MeV neutrons.

Fig.II.12 shows the scatter plot of the energy deposited E_{conv} in the converter and that released in the whole telescope E_{tel}. Apart from the contribution due to the titanium layer, all the energy is divided between the converter and the MST, so that the relation is linear with a negative unit slope.

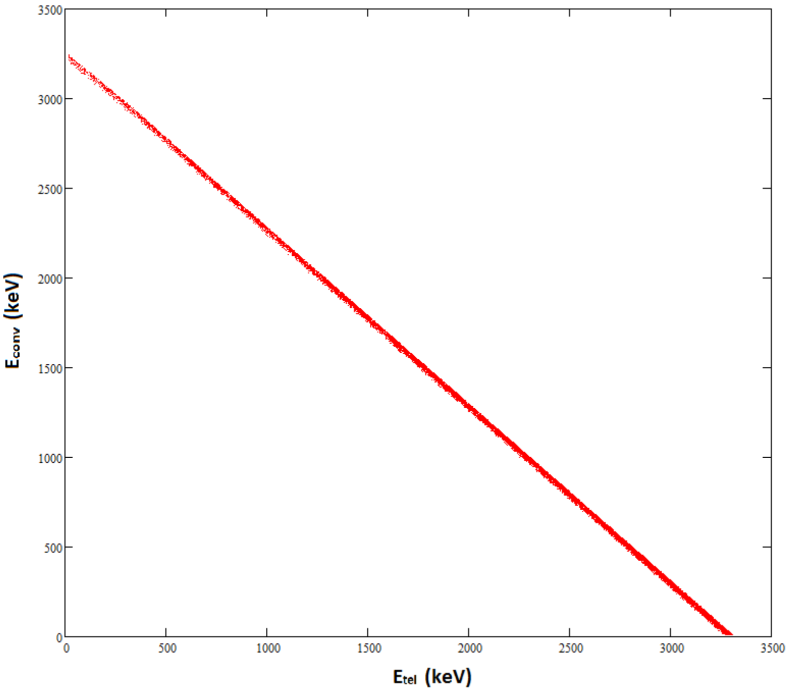

Fig.II.12: E_{conv}-E_{tel} scatter plot for 3.31 MeV neutrons.

With a response function to monoenergetic neutrons as narrow as demonstrated by the analytical model, an unknown neutron spectrum can be reconstructed from that of the recoil-protons just by taking into account the energy-dependent neutron interaction probability, without the need of an unfolding procedure. This should allow to performed real-time spectrometer.

Chapter III

CHARACTERIZATION AND OPTIMIZATION OF THE ACTIVE CONVERTER

The numerical study described in Chapter II allowed to design a detection system with response functions to monoenergetic neutrons rather narrow. This result gave confidence about the possibility of developing a spectrometer able to measure neutron spectra in real-time, without the need of unfolding procedures.

The main feature of the new system is the introduction of an “active” converter which i) converts neutrons into recoil-protons via elastic scattering and ii) measures the energy loss of recoil-protons inside the converter. The latter information can be derived by using an adequate photomultiplier stage coupled to a selected plastic scintillator.

In order to study the best solution which allows to acquire the scintillation light by keeping the whole detecting system as compact as possible, two different devices were studied: a compact commercial photomultiplier tube (PMT) and a silicon photomultiplier (SiPM).

III.1 Active converter: BC-404 plastic scintillator

The active converter spectrometer (ACSpect) is based on the use of a plastic scintillator as a fast neutron converter.

The commercial product selected to this aim has been the BC-404 scintillator fabricated by Saint-Gobain Crystals [43,44], a blue-emitting polyvinyltoluene based scintillator. This material was chosen by taking into account i) the high light output (68% of Anthracene), ii) the fast response (0.7 ns of rise time, 1.8 ns of decay time), iii) the maximum emission wavelength (408 nm).

Table III.1 shows the main data about the BC-404 scintillator, while Fig.III.1 shows the emission spectrum of the scintillator.

Light output (%Anthracene)	68
Rise Time (ns)	0.7
Decay Time (ns)	1.8
Pulse Width in FWHM (ns)	2.2
Wavelength of Maximum Emission (nm)	408
Light Attenuation Lenght (cm)	140
Bulk Light Attenuation Lenght (cm)	160
Number of H atoms (cm^{-3})	$5.21\ 10^{22}$
Number of C atoms (cm^{-3})	$4.47\ 10^{22}$
Ratio H:C Atoms	1.1
Density (g cm^{-3})	1.032
Refractive Index	1.58
Expansion Coefficient ($°C^{-1}$ (<67°C))	$7.8\ 10^{-5}$
Softening Point (°C)	70
Vapor Pressure	May be used in vacuum
Light Output	-60°C to +20°C independent form temperature, at 60°C it is 95% of that at 20°C

Table III.1: Main data of the BC-404 scintillator [44].

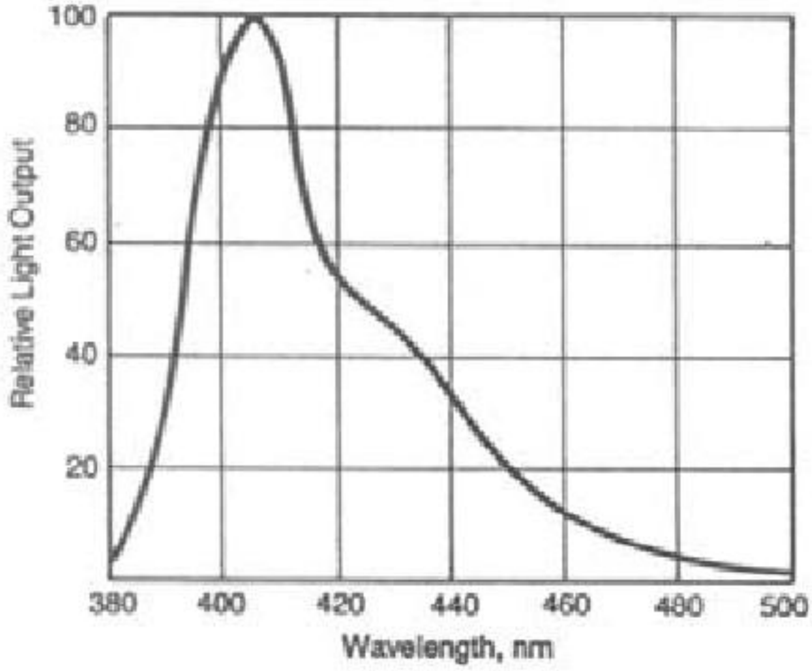

Fig.III.1: Nominal emission spectrum of the BC-404 scintillator [44].

Fig.III.2 shows the dependence of the scintillation light output on the interacting particle energy for different kind of particles. As can be observed the light output for protons is generally quite low and one order of magnitude lower than that of electrons. At energies lower than 1 MeV the total number of optical photons generated are lower than a thousand. This affect the uncertainty of the information provided by the scintillator.

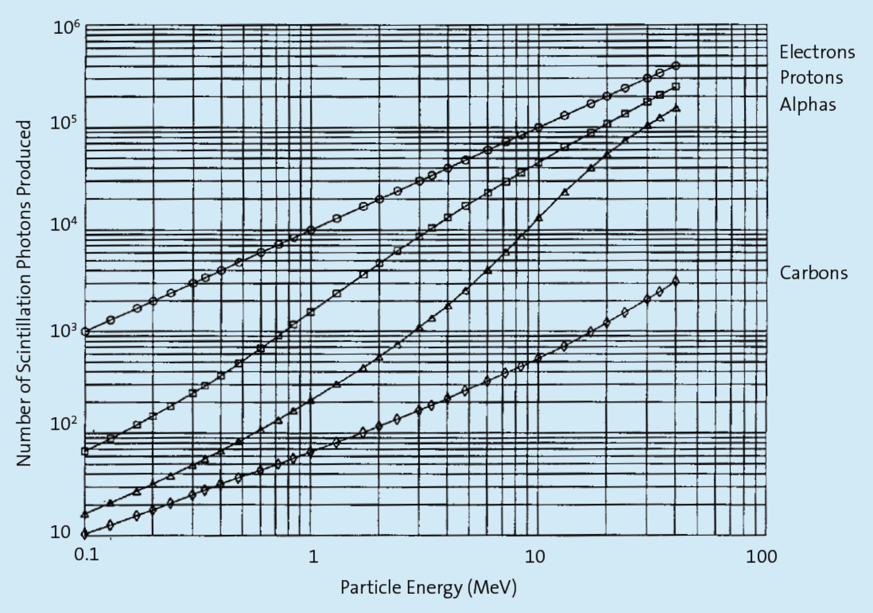

Fig.III.2: Scintillation Light Produced vs. Particle Energy in the BC-404 scintillator [43].

The scintillator was shaped from a sheet 2 mm in thickness, obtaining dimensions of 7.3 mm x 9.5 mm. The lateral and the top faces (the neutron entrance) were covered with BC-620 paint [41], a reflector based on titanium dioxide. A sample of the obtained converter is shown Fig.III.3.

Fig.III.3: A sample of the BC-404 scintillator –based converter covered with BC-620 reflective paint.

The scintillator interface was coupled to a PMT using a BC-630 silicone optical grease [43], a low evaporation compound with a density of 1.06 g cm^{-3} and refractive index of 1.465, both close to that of the scintillator.

IV.2 Photomultiplier tube: H10720-110

The selection of the best photomultiplier tube for the active converter was based on the following needs: i) small size to keep the whole system as simple as possible; ii) high sensitivity in the visible range to match the weak scintillator response; iii) high speed response to manage high count rates (mainly due to photons).

By taking into account these requirements, the photomultiplier tube H10720-110 fabricated by Hamamatsu was adopted [45]. This device is a module containing a high-voltage power supply circuit and a photomultiplier tube R9880U-110 [46].

Fig.III.4 shows the device with its power supply circuit, while Table III.2 shows the main data about the PMT package.

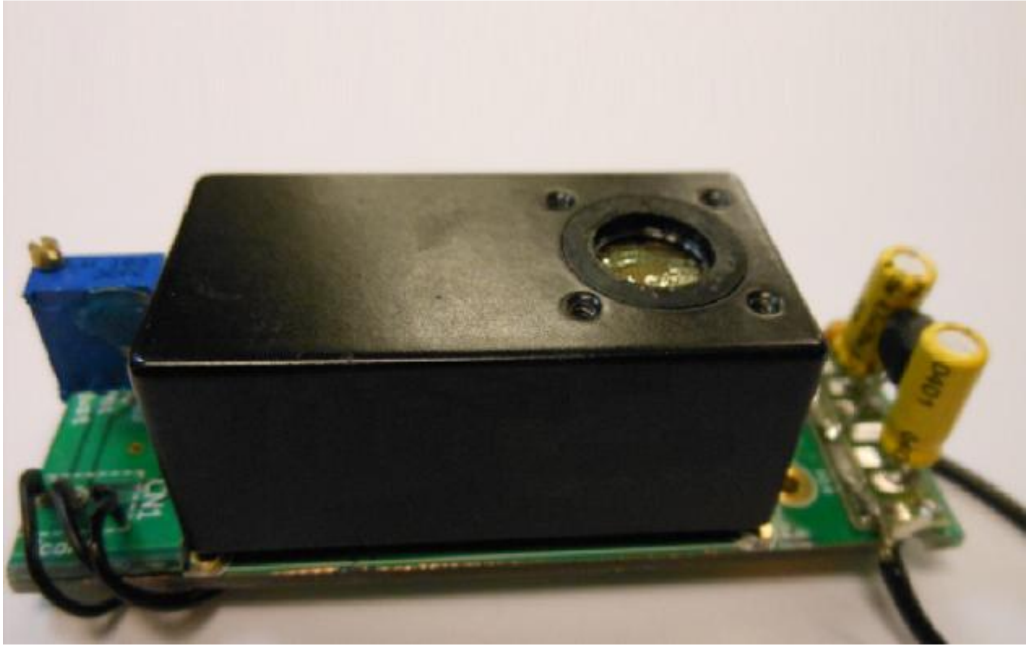

Fig.III.4: H10720-110 PMT with its power supply circuit.

Spectral Response (nm)	230 - 700
Input Voltage (V)	+4.5 - +5.5
Max. Input Current (mA)	2.7
Max. Output Current (μA)	100
Control Voltage (V)	+0.5 to +1.1
Effective Area Ø (mm)	8
Peak Sensitivity Wavelength (nm)	400
Rise Time (ns)	0.57
Operating Temperature (°C)	+5 to +50
Weight (g)	45
Width x Height x Depth (mm)	25 x 18 x 50
Cathode	
Luminous Sensitivity (μA/lm)	105
Blue Sensitivity Index	13.5
Radiant Sensitivity (mA/W)	110
Anode	
Luminous Sensitivity (A/lm)	210
Radiant Sensitivity (A/W)	$2.2 \cdot 10^5$
Dark Current (nA)	1

Table III.2: Features of the H10720-110 PMT [45].

Fig.III.5 shows the quantum efficiency and the radiant sensitivity as a function of the wavelength (left). The maximum value of the quantum efficiency is located in the 300-400 nm interval, matching the 408 nm maximum emission value of the BC-404 scintillator. Fig.III.5 right side shows also the gain of the photomultiplier as a function of the control voltage (voltage that must be provided to the module to set the PMT gain).

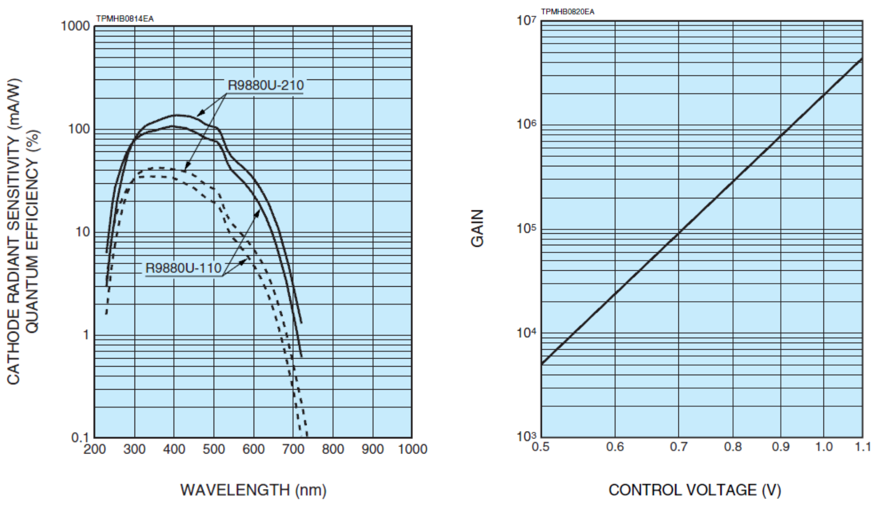

Fig.III.5: Dependence of the quantum efficiency and radiant sensitivity of the R9880U-110 PMT on the incoming photon wavelength (left). PMT gain as a function of the control voltage (right) [46].

The power supply circuit was set to provide +5 V as input voltage, and the control voltage was set at 1.05 V, corresponding to a gain of about $2.8 \cdot 10^6$.

This PMT package is not designed to work in vacuum, so the layout of the system was conceived to place the device outside the vacuum volume.

III.3 Silicon Photomultipliers

Although the photomultiplier tubes (PMT) remain at the present time the most commonly used devices for scintillation light acquisition, recently new compact solutions based on silicon devices has been proposed. With respect to standard PMT these semiconductor devices offer a higher quantum efficiency (defined as the average number of emitted photoelectrons per incident photon), fast response, lower power requirements, reduced size and immunity to magnetic fields.

The SiPM consists of an array of independent and identical microcells working together as digital photon counters [47] on a common load.

Essentially, every cell is a Geiger-mode avalanche photodiode (G-APD), a p–n junctions biased at a voltage above the breakdown threshold [48]. At this bias, the electric field is so high ($>3 \times 10^5$ V/cm) that a single charge carrier injected in the depletion layer can trigger a self-sustaining avalanche [49]. Current continues to flow until the avalanche is quenched, by lowering the bias voltage down to or below the breakdown threshold.

The number of cells that produce a discharge in a scintillation event is then proportional to the number of incident optical photons. Each cell produces a pulse at the same time (in coincidence), leading to an output signal given by the pile-up of all pulses. Since in a typical scintillation event thousands of photons are produced, the number of cells of a SiPM should be approximately that order of magnitude.

The SiPM has a high sensitivity with respect to both single electron produced by scintillation photons (the signal) and electrons promoted to the conduction band due to thermal excitation (the background). In particular, the latter generate random pulses, called darkcount, which are constantly added to the scintillation signal. The darkcount rate at room temperature for a SiPM can reach values of 10^6 pulses per second per mm^2 [50]. Most of darkcount events are generated by single cells, therefore the contribution due to darkcount may be reduced a few orders of magnitude by applying an acquisition threshold to the SiPM output signal. The proper threshold level must be selected experimentally and typically corresponds to the amplitude of signals due to pile up of a few cells (three or four).

The darkcount rate could also be reduced by cooling the device, but this can be done at the cost of an higher noise level due to the afterpulsing, a phenomenon associated to the delayed emission of electrons trapped by impurities in silicon. This electron emission can trigger a delayed avalanche inside the cell some microseconds after the main signal (Fig.III.6). The contribution of an afterpulsing event to the output signal depends on its delay of occurrence, that grows by a factor of 3 for a temperature reduction of 25 ° C [51].

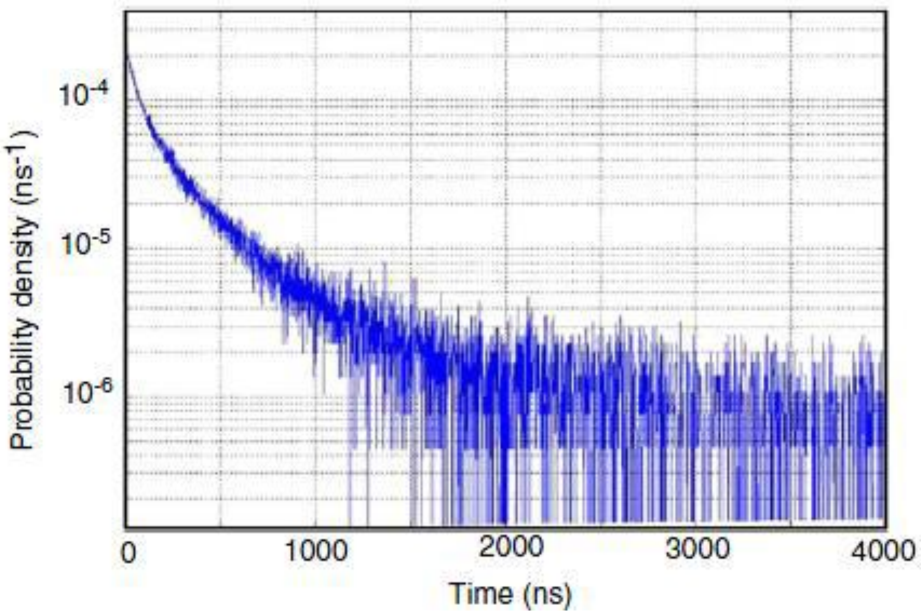

Fig.III.6: Probability of a delayed release of carriers as a function of the time after a breakdown event [52].

Avalanches triggered with a short delay contribute only partially because the cells in which they occur are not yet fully charged. However, these events affect the charging time of the device. The time required for a cell to recharge after the avalanche process is interrupted depends mainly on the size of the cell. Afterpulsing events can prolong the charging time of the cell because the process must start again after every discharge, even partially. Some SiPMs require hundreds of microseconds for a new signal to reach the 95%

of their performance. The charging time can be reduced by using small cells and by operating at low gains.

During an avalanche, every 10^5 charge carriers 3 photons on average are emitted with energy greater than 1.14 eV (silicon E_{gap}) [49]. It is therefore possible that these photons escape from their original cell and interact with the closest cells, triggering another avalanche (Fig.III.7).

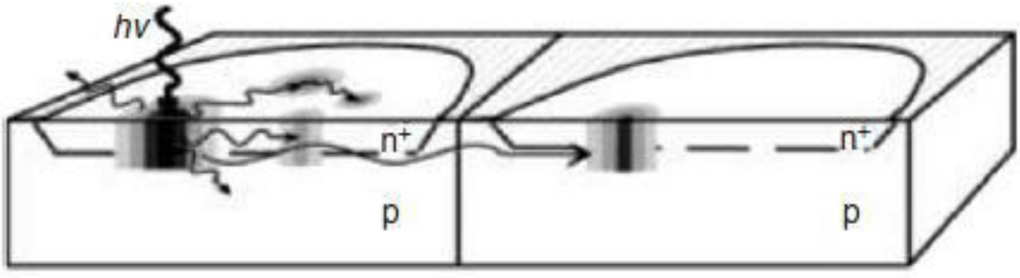

Fig.III.7: Crosstalk event in multi-cells SiPM [51].

This is a stochastic phenomenon, known as crosstalk, which introduces an additional statistical fluctuation of the output signal. It can be reduced by placing opaque septa between adjacent cells, though photons emitted during the avalanche can be reflected in the scintillator and overcome the septa between the individual cells.

III.4 SiPM characterization

In order to study the possibility of using a SiPM device as the active converter of the ACSpect, a thorough characterization of its response was carried out.

The adopted specimen was a SiPM constituted by matrix of 60x60 cells, with a total active area of 10 mm^2. Fig.III.8 shows the device coupled with a BC-404 plastic scintillator (polyvinyltoluene) and the associated front-end electronics.

The data acquisition and analysis were performed through a dedicated software for digital data acquisition developed in LabVIEW environment [53] in the framework of this thesis.

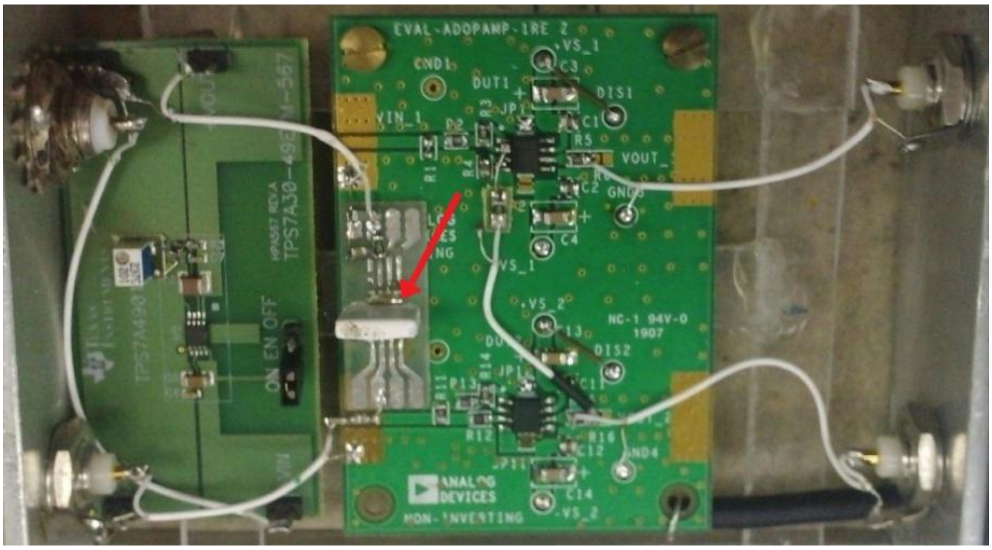

Fig.III.8: Picture of the set-up used to test the SiPM coupled with a BC-404 scintillator.

The first tests concerned the darkcount analysis. Since the SiPM output signals are pulses of exponentially decaying shape with a time constant of 70 ns which can pile up, a dedicated signal identification and filtering procedure was developed. This procedure is based on the digitalization of trains of darkcount signals and the subsequent deconvolution of this data with the pulse response of the SiPM (found to be an exponential function). Fig.III.9 shows the results of the darkcount signal analysis after the deconvolution procedure and after filtering with a triangular filter (final).

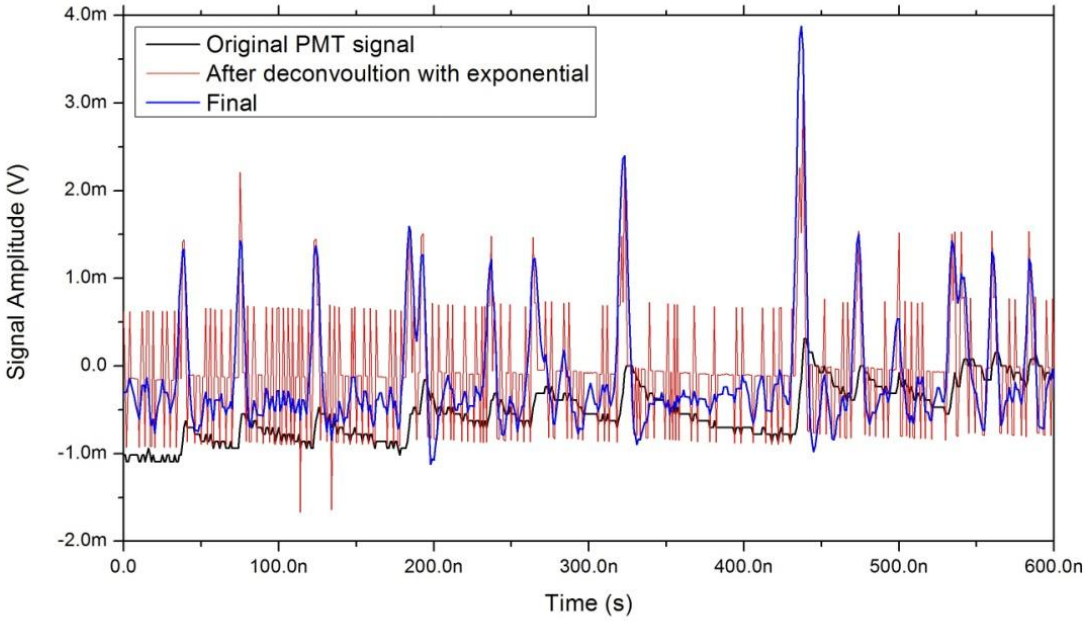

Fig.III.9: Darkcount signals from PMT (black), after deconvolution (red) and triangular filtering (blue).

The filtered signal was then analyzed through two different peak search routines: one based on a quadratic peak fitting procedure and a second one which employs a gated integrator algorithm.

Fig.III.10 shows the darkcount spectra obtained at different bias voltages (from 28 V to 33 V) through the quadratic peak fitting routine. By a thorough analysis of these results a breakdown voltage of about 29.2 V was determined.

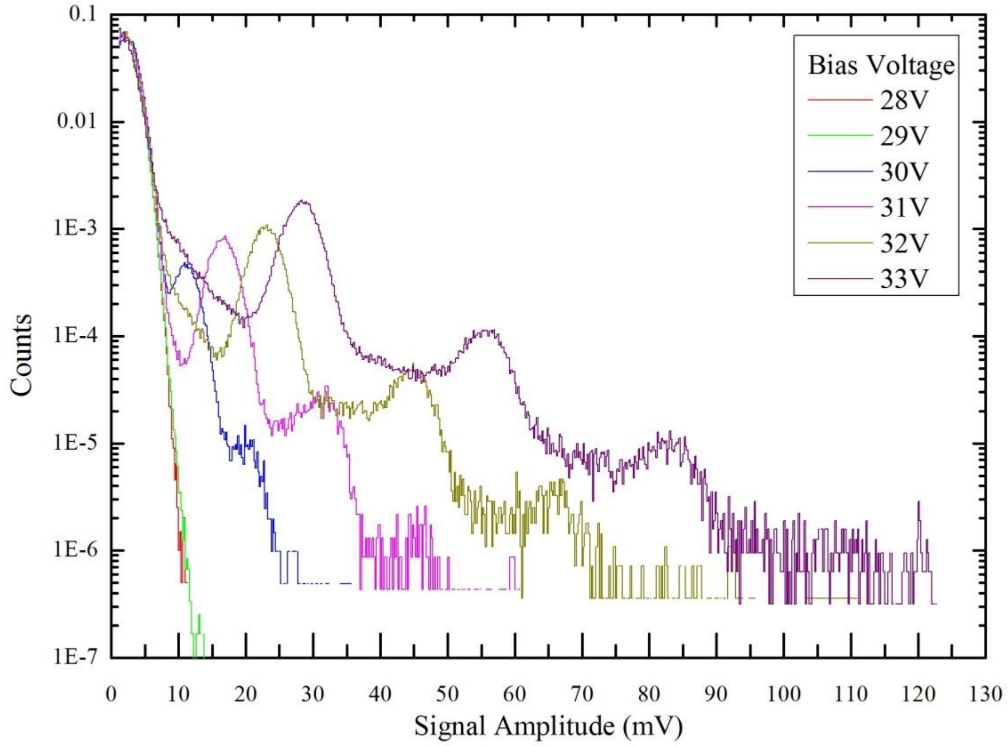

Fig.III.10: Darkcount spectra at different bias voltages. Spectra obtained by means of a quadratic polynomial peak fitting. Spectra were normalized to unit area.

Spectra at 28 V and 29 V show only noise signal being the SiPM below the breakdown voltage, where the avalanche process cannot be triggered. Above the breakdown threshold the avalanche can occur and the darkcount rate increases with the bias voltage. Nevertheless, higher voltages lead to higher gain and better signal-noise ratios.

The darkcount rate distribution at 33V was studied also with the gated integrator routine, by setting the discrimination threshold in order to exclude the background noise. Fig.III.11 shows the differential and the integral distribution of pulses obtained. In Fig.III.12 the single-cell and the double-cell darkcount event peaks are fitted with

Gaussian curves. The single cell area was found to be 51.25 pVs, with a standard deviation of 4.67 pVs, corresponding to a signal-noise ratio of 10.97.

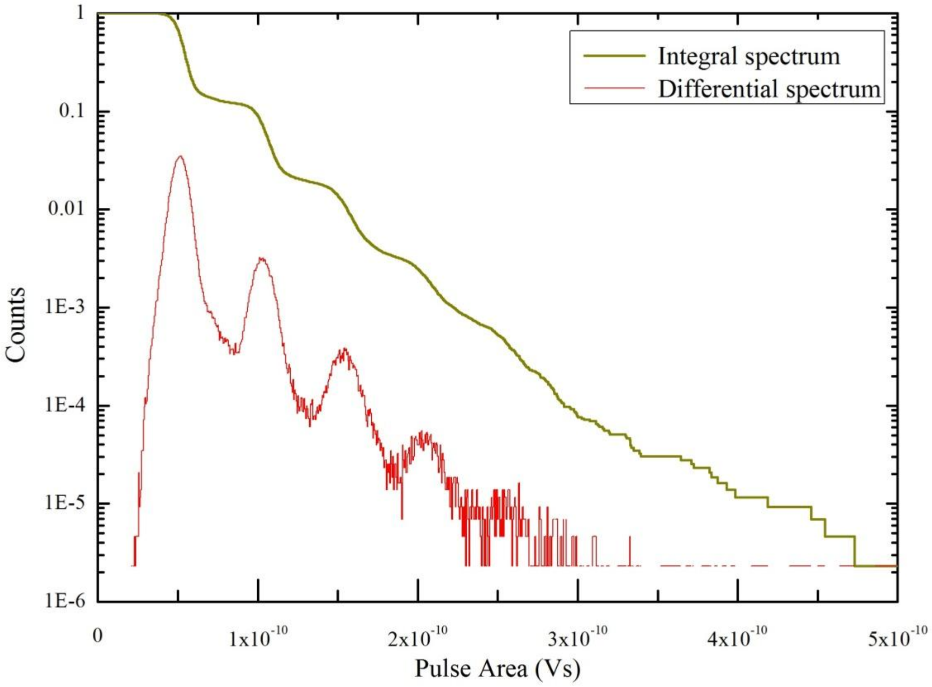

Fig.III.11: Darkcount differential and integral spectra at 33V of bias voltage.
Spectra obtained with a gated integrator algorithm. Spectra normalized to unit area.

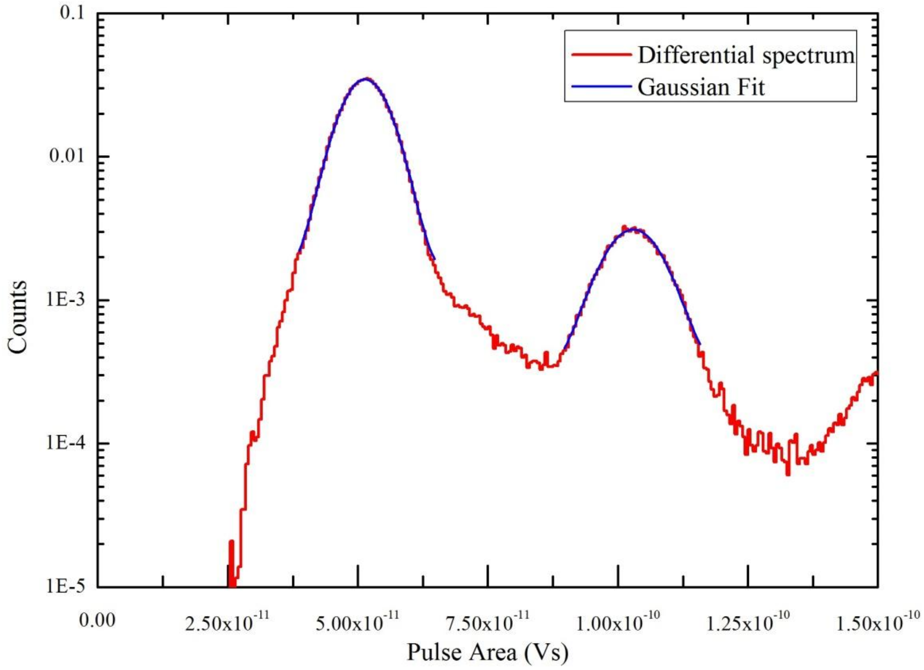

Fig.III.12: Darkcount differential spectra at 33V of bias voltage.
Gaussian fit of the single-cell and double-cell darkcount events peaks.

The time intervals between two subsequent pulses were also studied. The distribution in Fig.III.13 was fitted with an exponential function having mean value of τ = 75 ns. The good agreement of the exponential curves confirms the Poisson statistics of pulses, while the small additional contribution below 100 ns can be attributed to afterpulsing phenomena.

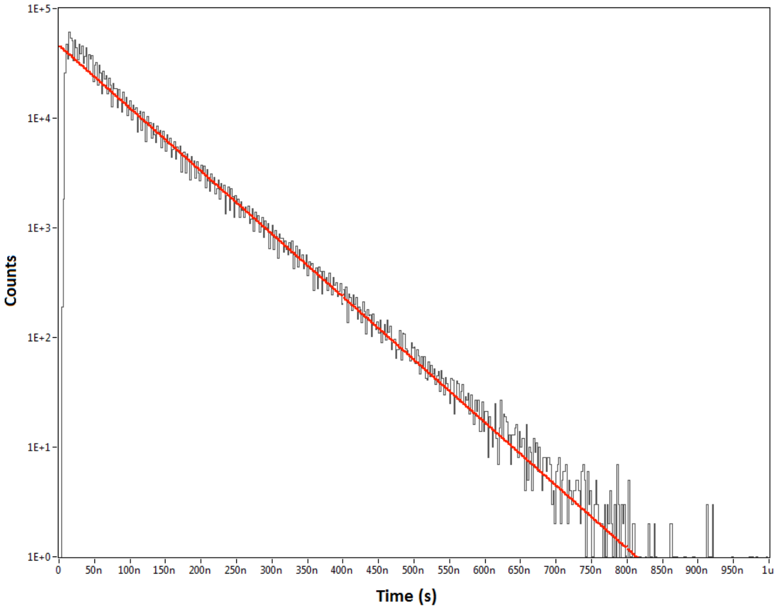

Fig.III.13: Spectrum of time intervals between subsequent darkcount pulses; exponential fit (red) with time constant τ = 75 ns.

The mean darkcount rate DCR can be evaluated as the inverse of the mean time interval value: DCR = $1.32 \cdot 10^7$ counts/s. By multiplying the darkcount intergral spectrum by the mean darkcount rate, the so called "staircase function" is obtained (Fig.III.14).This is characterized by a series of plateaus (each corresponding to N-cells events) whose value decreases sharply (typically an order of magnitude in frequency) for defined thresholds.

The staircase function is useful to select the discrimination threshold according to the corresponding darkcount rate.

Setting the threshold at 0.5 photo-electron ("half-photon threshold"), and counting the number of pulses that exceed this value, it gives the number of times that one or more photons are detected. By counting the number of pulses that exceed the threshold at a number N-0.5 photo-electrons gives the number of times that N or more photons are detected.

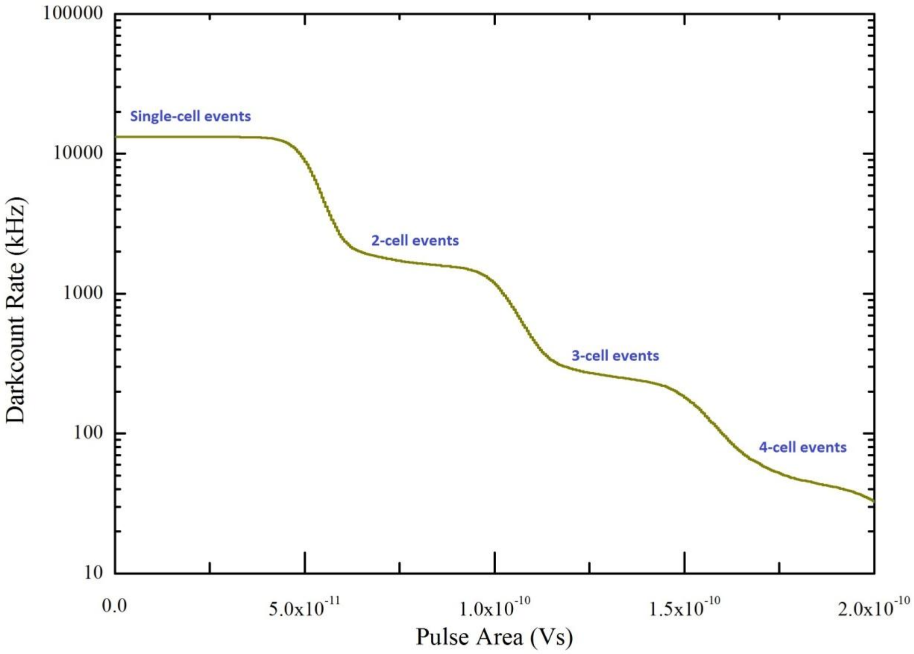

Fig.III.14: Obtained darkcount rate staircase function.

Fig.III.15 shows the correlation distribution of the time between a darkcount pulse (center line) of any amplitude and the previous (left half) and following (right half) events. On the right half, in the single-cell events part, the circle highlights events with increasing pulse area in function of the time elapsed: these events are generated during the recharging of a cell, therefore due to afterpulsing.

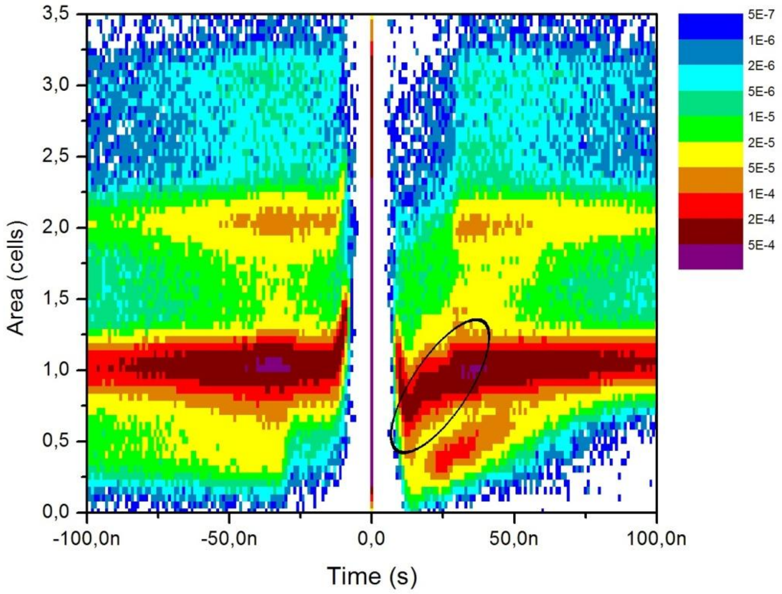

Fig.III.15: 2D spectrum of the correlation between a pulse and the previous and next; in the circle the recharging of the cells.

The SiPM coupled with the BC-404 scintillator was tested with ^{241}Am and ^{137}Cs sources. Fig.III.16 shows the signal filtering of a registered pulse.

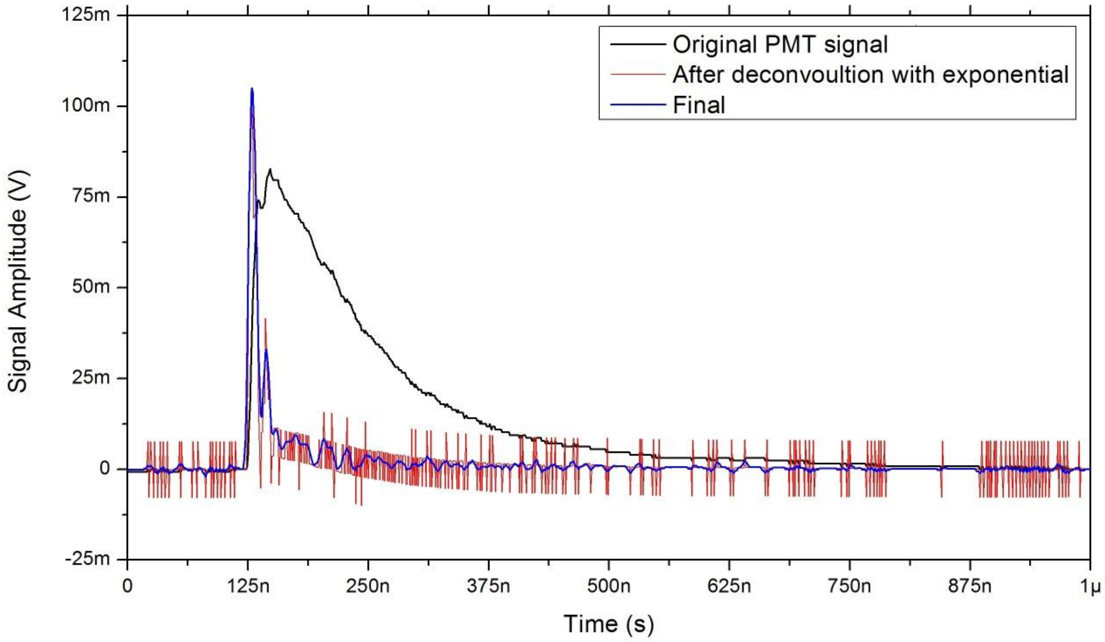

Fig.III.16: Signals obtained by irradiating the SiPM coupled with a BC-404 scintillator.

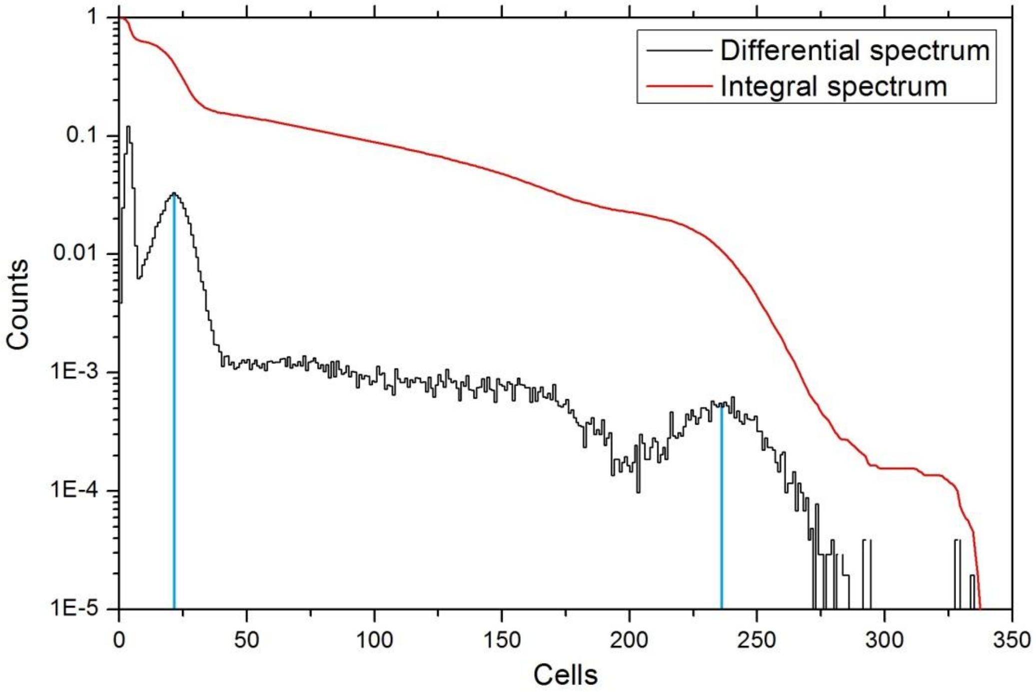

Fig.III.17: Spectrum obtained by irradiating the SiPM coupled with a BC-404 scintillator with ^{241}Am and ^{137}Cs sources.

The spectra of the two sources obtained with the SiPM is shown in Fig.III.17. The peak corresponding to the 59.5 keV photons from ^{241}Am resulted to be generated by about 21 cells, while the 661.7 keV photons from ^{137}Cs correspond to 233 cells, suggesting a linear behavior of the device.

The BC-404 datasheet (Fig.III.2) provides a photon generation of about 10 photons/keV. This leads to a ratio between the collected and the generated photons (collection efficiency) of 3.5%. It must be underlined that in these tests the SiPM-scintillator coupling was not optimized and the scintillator surface was not protected by reflecting materials.

III.5 SiPM-PMT comparison

A direct comparison was also performed between the studied SiPM and the commercial photomultiplier tube H10720-110 (made by Hamamtsu). The two devices were coupled with a BC-404 scintillator and irradiated at the same time with a ^{137}Cs source.

The two spectra, normalized to unit area, are compared in Fig.III.18. As can be observed, the PMT resolution is definitely better: the γ peak of the ^{137}Cs at 661.7 keV has a FWHM of 29.4% for the SiPM and 5.2% for the PMT.

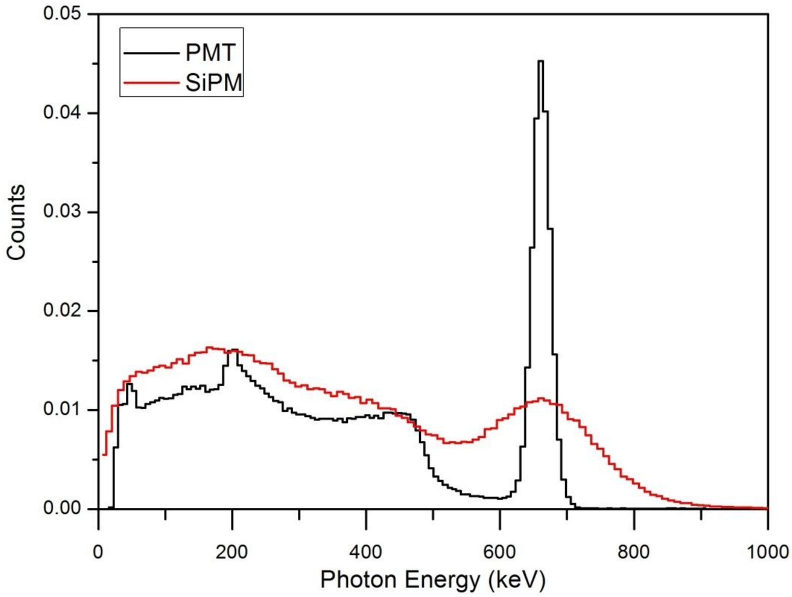

Fig.III.18: Spectra obtained by irradiating the SiPM and the PMT, coupled with BC-404 scintillators, with a ^{137}Cs source.

A first version of the whole Active Converter Spectrometer was developed to characterize the performances of both photomultipliers in coincidence with the Monolithic Silicon Telescope (Fig.III.19). Tests were performed at INFN Laboratori Nazionali di Legnaro (LNL) with 3.31 MeV monoenergetic neutrons generated by 5 MeV protons delivered on a thin LiF target (700 ug/cm^2).

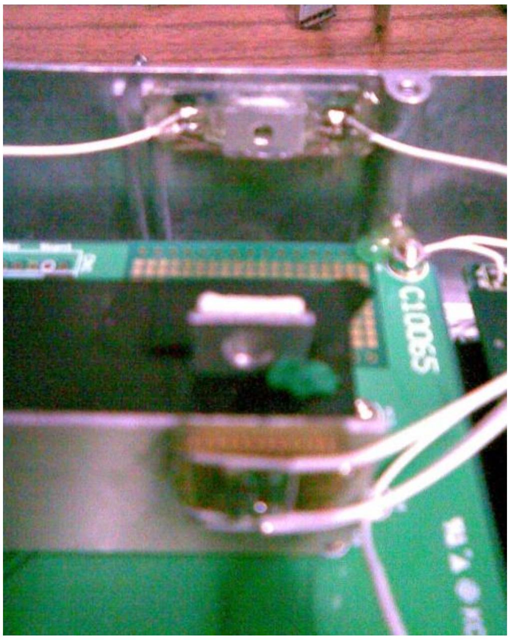

Fig.III.19: A test version of the Active Converter Spectrometer: on the case wall the SiPM, in the centre (black) the PMT, both with scintillator and collimator, on the bottom the MST (rear).

After being irradiated with a total fluence of $2.22 \cdot 10^{8}\ \mathrm{n \cdot cm^{-2}}$, the SiPM device resulted to be damage by neutrons. Therefore it demonstrated to be unsuited for working in fast neutron fields.

III.6 PMT photon collection efficiency

The PMT was selected as the best solution for collecting the scintillation light of the active converter.

Test measurements were performed in order to study the efficiency of the scintillator-PMT coupling in terms of photon collection.

A preliminary test was conducted by irradiating the device with a ^{137}Cs source and by acquiring directly the output of the PMT.

The number of detected photons was calculated from the pulses area:

$$Photons = \frac{Area}{R \cdot e \cdot G \cdot QE}, \tag{III.1}$$

where Area is expressed in V·s, R is the termination impedance of the output signal (50 Ω), e is the charge of the electron ($1.602 \cdot 10^{-19}$ C), G is the PMT gain ($2.8 \cdot 10^{6}$) and QE is its nominal quantum efficiency (30%).

The resulting spectrum is shown in Fig.III.20. The ^{137}Cs 661.7 keV peak corresponds to 1800 photons. The BC-404 datasheet (Fig.III.2) provides for this energy a photon generation of 6600 photons, so the collected photons are the 27.3% of the generated ones.

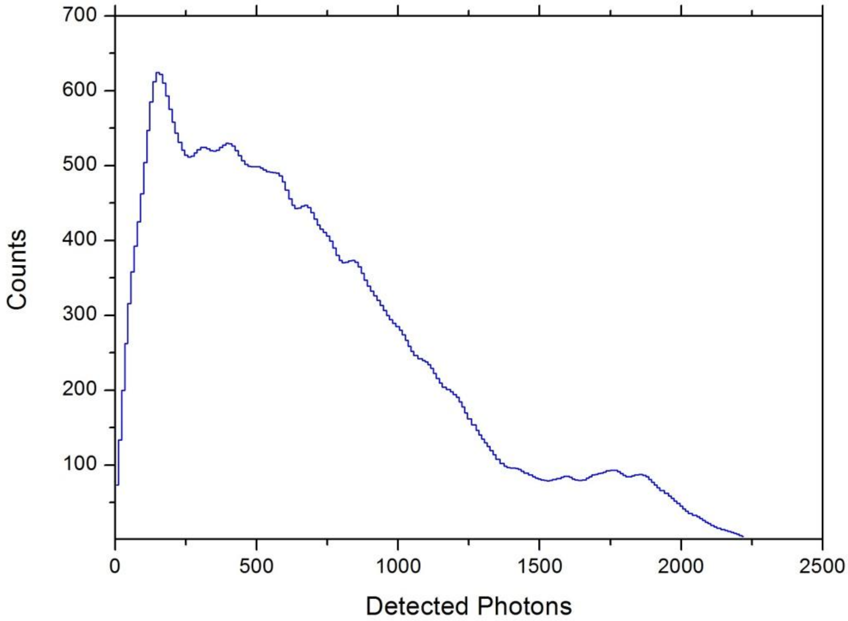

Fig.III.20: Spectrum of a ^{137}Cs source from direct PMT output.

In order to measure the light generation and collection efficiency of the system scintillator-PMT irradiated with neutrons, the same procedure was repeated during the preliminary irradiations with neutrons.

The spectrum of the energy deposited in the converter was firstly acquired independently of the rest of the system, by digitizing the PMT output signals of the PMT.

In this configuration events detected by the scintillating converter were mainly due to photons associated to the neutron field. The light collection efficiency was calculated with the (III.1).

The signals generated by the scintillating converter were also acquired in coincidence with those produced by the MST in order to select only those events generated by neutrons.

Fig.III.21 shows the spectrum of the PMT output expressed in detected photons. In Fig.III.22 is shown also the spectrum with a without coincidence technique.

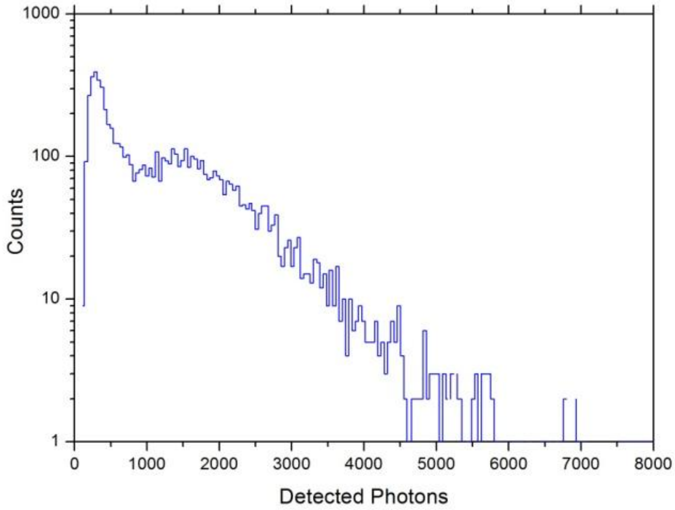

Fig.III.21: Spectrum collected with a 3.31 MeV neutron beam: PMT output.

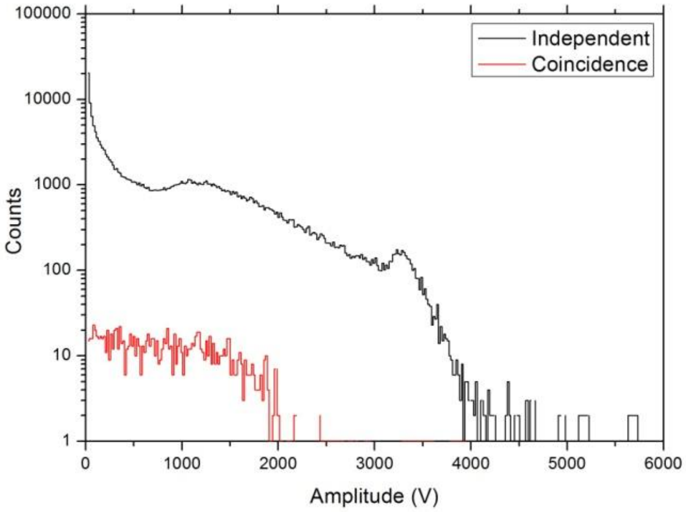

Fig.III.22: Spectra collected with a 3.31 MeV neutron beam: amplified output without coincidence (black), amplified output with coincidence (red).

The spectrum acquired with the electronic chain was then compared with the one of the PMT output in order to calibrate the amplified signal spectra in terms of detected photons. Fig.III.23 shows the results of this calibration procedure.

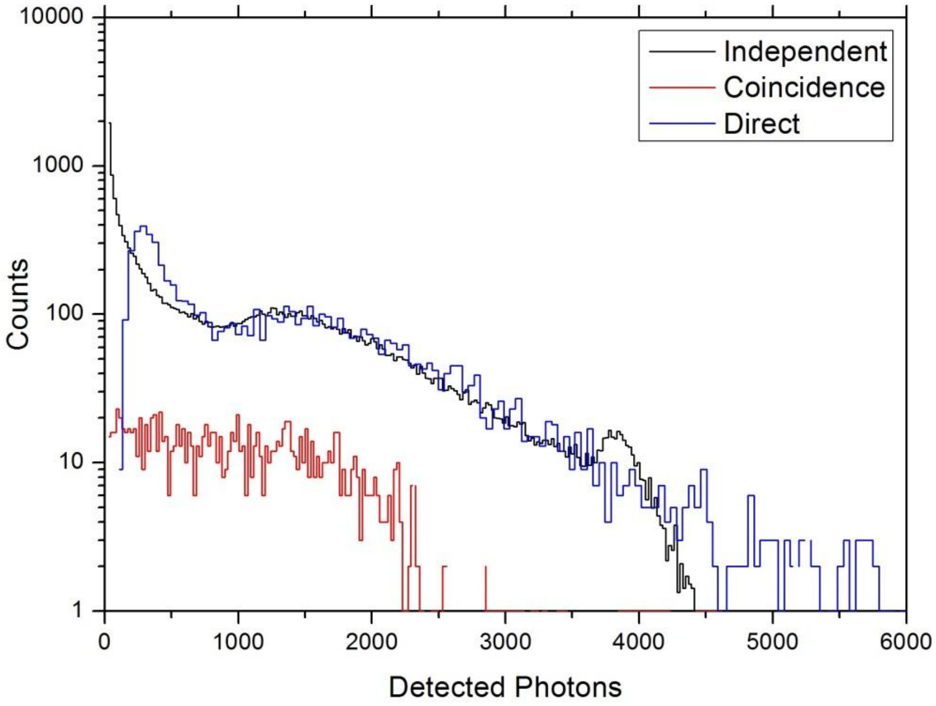

Fig.III.23: Spectra of a 3.31 MeV neutron beam; direct PMT output (blue), amplified output without coincidence (black), amplified output with coincidence (red).

The spectrum derived in coincidence has a maximum at about 2250 photons, while the scintillator datasheet provides a number of 9000 photons for the energy of the measured neutron beam. The collected photons resulted to be the 25% of the generated ones, in agreement with the preliminary test.

III.7 Non-linearity of the converter

Preliminary tests with monoenergetic neutrons highlighted a non-linearity in the behavior of the converter. The comparison between the analytical behaviour described in Chapter II and the acquired data is presented in Fig.III.24.

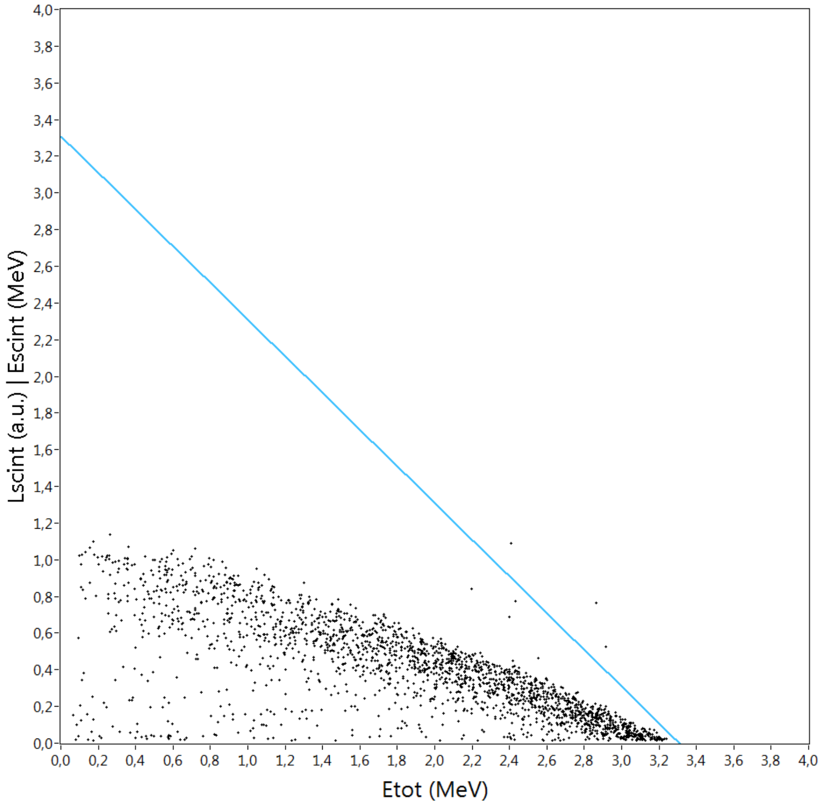

Fig.III.24: E_{scint}-E_{TOT} scatter plot obtained with a 3.31 MeV neutron beam (black) and expected trend (blue).

This non-linear behavior is due to the light generation process in the plastic scintillator. It is well known that a high ionization density alters the behavior of the molecules of the organic medium along the particle track, affecting the scintillation process by lowering the light conversion yield.

The Birks' Law [54,55] describes the dependence of the light emitted per unit length dL/dx on the energy loss per unit path dE/dx (stopping power) of the interacting particle:

$$\frac{dL}{dx} \propto \frac{\frac{dE}{dx}}{1+k_B \cdot \frac{dE}{dx}}, \qquad \text{(III.2)}$$

where k_B is the Birks' constant, which depends on the scintillating material. k_B is estimated to be 0.088 mm/keV for polyvinyltoluene based scintillators [56].

The integration of equation (III.2) gives:

$$L = \int_0^{E_p} \frac{1}{1+k_B \cdot \left(\frac{dE}{dx}\right)^{poly}(E)} dE \,, \tag{III.3}$$

where L is the generated light, E_p is the proton energy, $\left(\frac{dE}{dx}\right)^{poly}(E)$ is the proton stopping power in polyvinyltoluene as a function of the proton energy.

This model represents the light generated by a proton which stops in the converter.

Fig.III.25 shows the curves obtained with the model setting k_B = 0 mm/keV and k_B = 0.088 mm/keV.

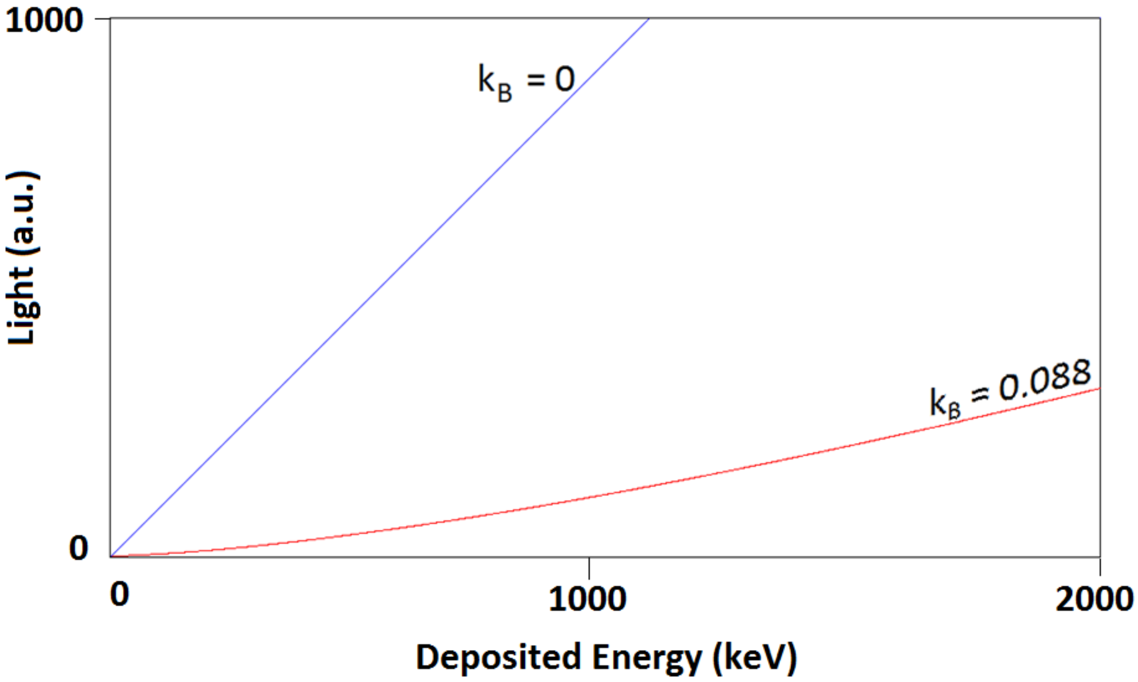

Fig.III.25: Light generation model: linear for k_B = 0 mm/keV and non-linear for k_B = 0.088 mm/keV.

III.8 Correction procedure

An analytical procedure was studied in order to test the possibility of correcting the non-linearity of the scintillator output. The procedure derives directly the total recoil-proton energy E_P from the two measured quantities: the light emitted in the scintillator L_{SCINT} and the energy deposited in silicon E_{TEL} (Fig.III.26, both in orange).

The algorithm calculates the equivalent quantity of light L_{EQ} (green) that corresponds to the residual recoil-proton energy measured by the telescope E_{TEL}.

The quantity L_{EQ} is then summed to L_{SCINT} to estimate the total light (L_P, ruby) generated by a recoil-proton of energy E_P. Finally, the total recoil proton energy E_P (ruby) is derived from L_P by applying the reverse function of equation (III.3) calculated numerically.

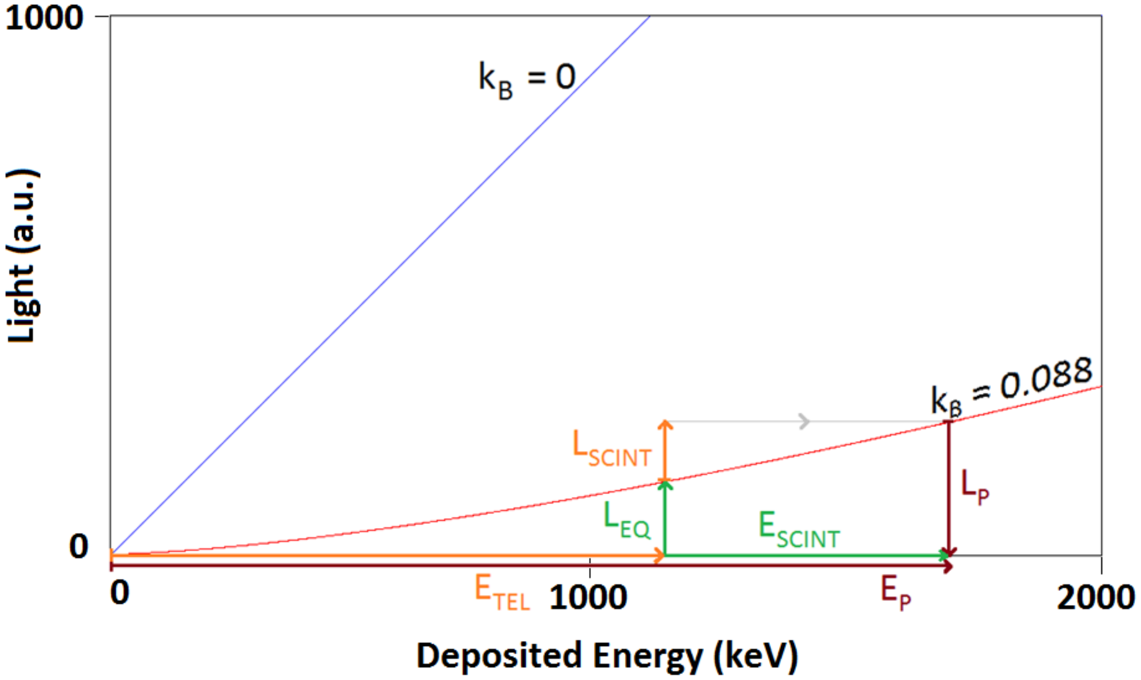

Fig.III.26: Representation of the correction procedure for the recovering of the total proton energy.

The energy deposited in the converter E_{SCINT} (green) can be calculated by subtracting E_{TEL} from E_P.

The correction procedure was directly implemented in the model described in Chapter II. Fig.III.27 shows the result obtained by applying the correction algorithm to the measured values. As can be observed, the linearization procedure demonstrates to be very effective.

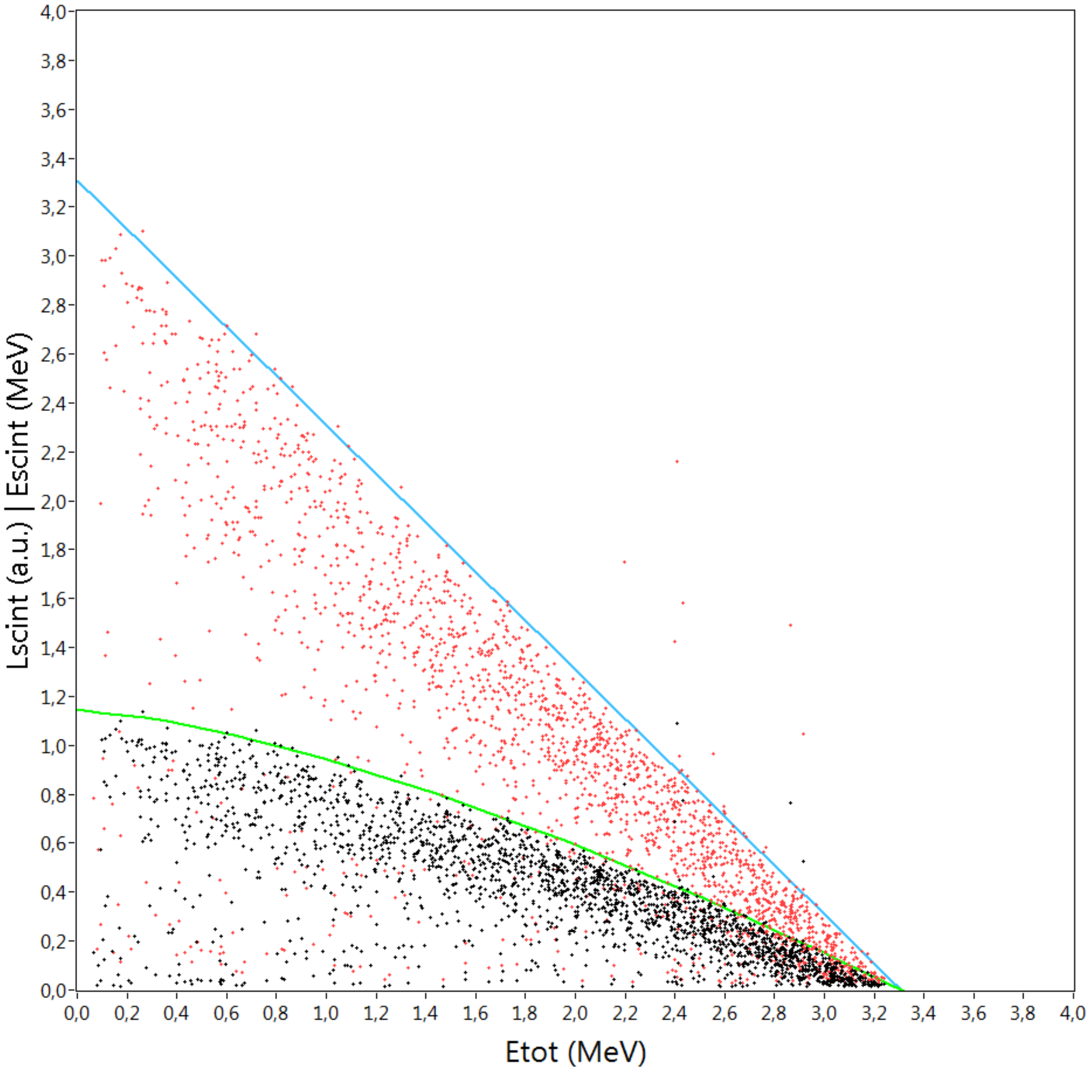

Fig.III.27: E_{scint}-E_{TOT} scatter plot obtined with a 3.31 MeV neutron beam: acquired data (black), non-linear trend (green), corrected data (red) and linear trend (blue).

Chapter IV

ACTIVE CONVERTER SPECTROMETER: SYSTEM LAYOUT

The analytical model (Chapter II) and the preliminary measurements with neutrons (Chapter III) highlighted the feasibility of the Active Converter Spectrometer ACSpect.

The test version of the complete system was designed in order to optimize the geometry and the performance of the spectrometer, in particular the need of a vacuum region between the converter and the silicon telescope. The construction was entirely carried out by the author of this thesis at the laboratories of the Nuclear Engineering Section of the Department of Energy, Politecnico di Milano.

IV.1 Complete layout of the ACSpect

The ACSpect consists of a combination of two stages: the active converter, based on a plastic scintillator, and a Monolithic Silicon Telescope, which acts as a recoil-proton residual energy measurement stage.

The selected MST is the prototype R327-12 #5 M1, a specimen characterized by a square area of 1 mm^2. Fig.IV.6 shows the MST and its assembly.

The main problem to face to assembly the actual system is the need of a vacuum layer between the converter and the MST. The final solution adopted to cope with that was to place the MST of Fig.IV.1 in a small aluminum box, 52 mm x 38 mm x 21 mm.

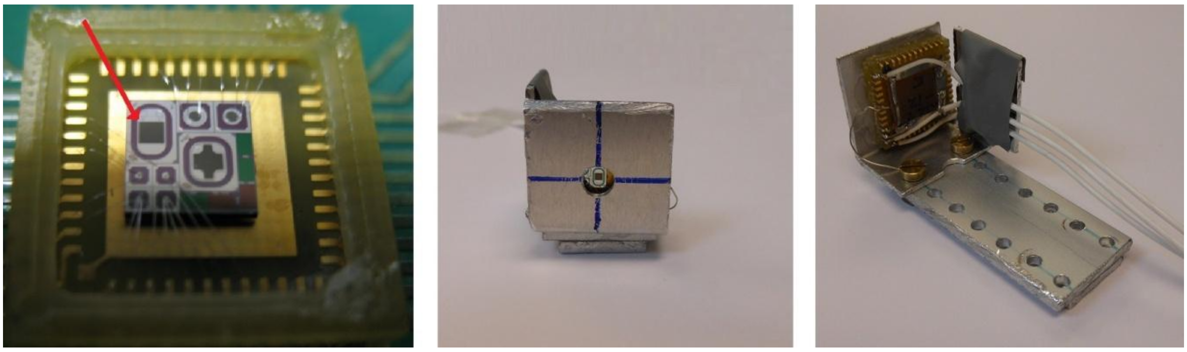

Fig.IV.1: The MST: from the left, the detector, front and rear of the assembly.

The box was equipped with a vacuum connector (Fig.IV.2, top-left) and a gasket was added to the lid in order to seal the case. An aluminum collimator (top-right) was then glued to the box to make a channel 4 mm in diameter and 2 cm in length for recoil-proton passage from the converter to the MST. The collimator was provided at one end with an o-ring. The plastic converter was finally coupled to the o-ring in order to complete the sealing of the box (bottom). Doing so recoil-protons directly enter the vacuum region, cross the collimation channel and imping on the MST. This configuration also grants the alignment between the converter and the MST.

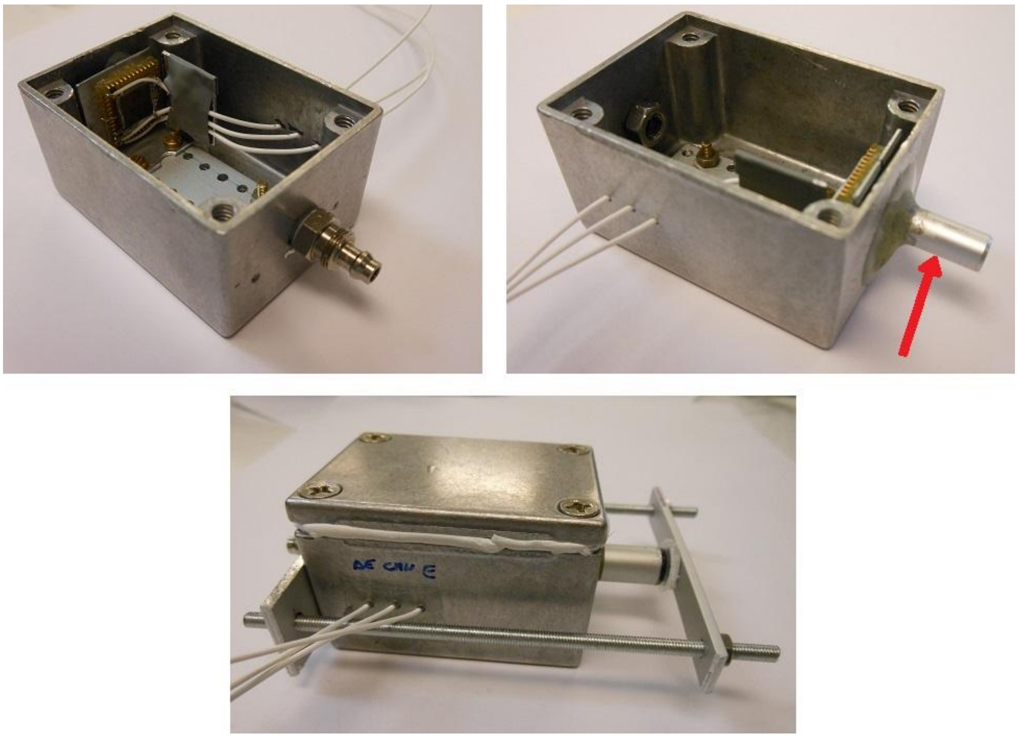

Fig.IV.2: The MST vacuum case: vacuum connector (top, left), aluminum collimator (top, right, red arrow) and the final assembly with the gasket and the converter sealing.

The actual distance between the converter and the MST resulted to be 21 mm. By considering the effective converter area, given by the collimator diameter, the maximum emitting angle of recoil-protons that reach the MST is θ = 7.35°. Therefore, being the proton energy given by $E_p = E_n \cdot \cos^2(\theta)$ (2.II), the nominal recoil-proton uncertainty due to geometrical collimation is about ±1.63%.

The ACSpect layout was completed by adding the front-end electronics of the MST. Two custom charge sensitive preamplifiers (Fig.IV.3, left) were connected to the device. These are modules entirely built in the Nuclear Electronics Laboratories of the Department of Energy, Politecnico di Milano. The boards were connected to the MST in the so called ΔE-E_{TOT} configuration, i.e. the charge is collected from the ΔE stage (to a preamplifier with an injection capacitance of 2.7 pF) and from the p^+ common layer (preamplifier C_{inj} = 10.34 pF) in order to get directly the total energy deposited inside the MST. The system was also tested with a commercial Cremat CR-110 charge sensitive preamplifier [57] mounted on a CR-150 board [58] (Fig.IV.3, right).

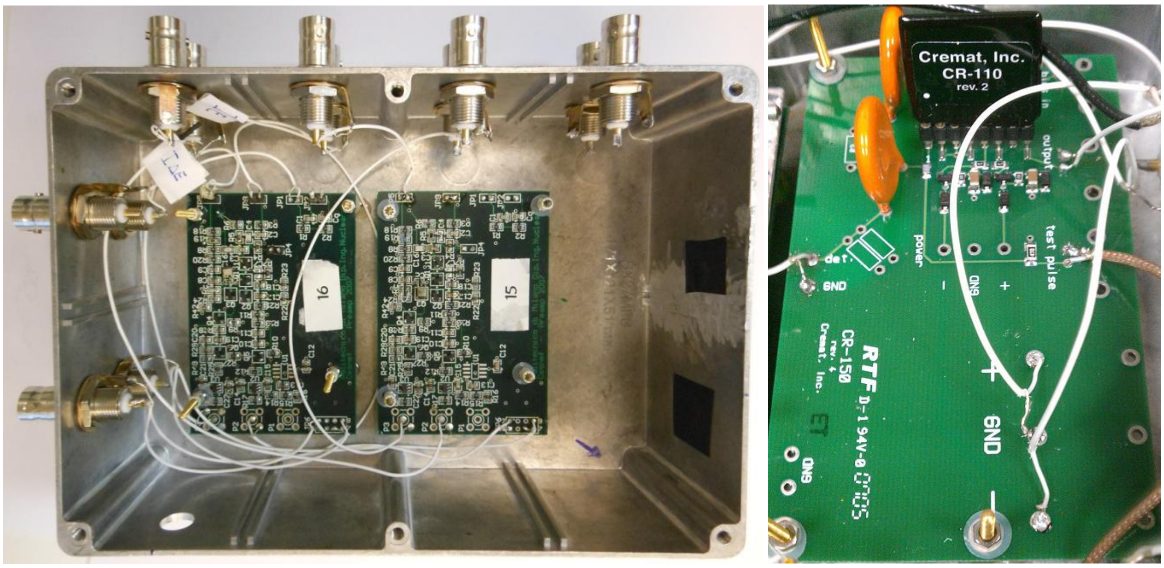

Fig.IV.3: MST front-end electronics: preamp2007 charge preamplifiers (left)
and Cremat integrated charge sensitive preamplifier CR-110 on CR-150 board (right).

All the components were placed in a 122 mm x 172 mm x 54 mm aluminum box, coupling the MST-converter vacuum case with the PMT. Fig.IV.4 shows the final ACSpect assembly.

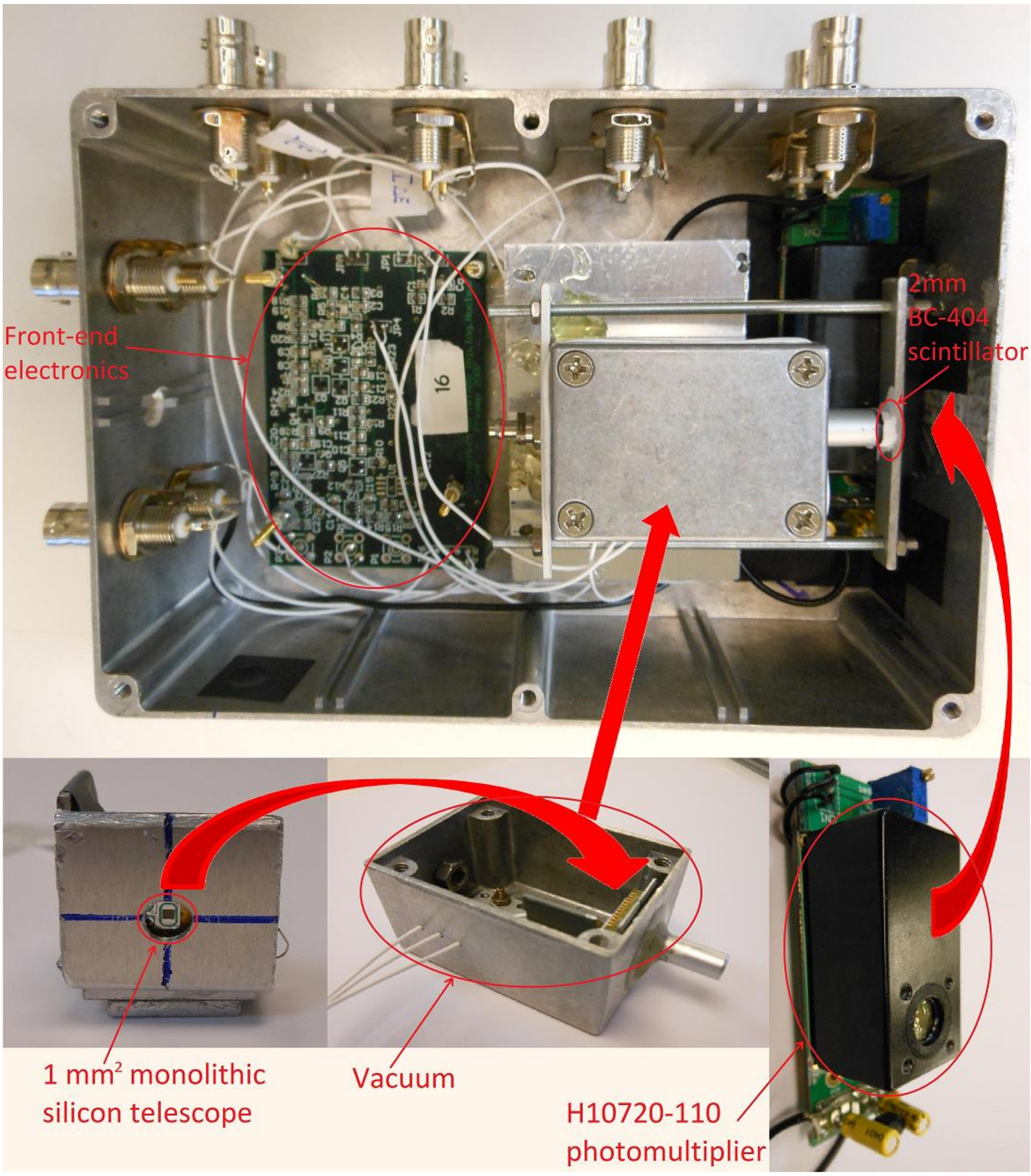

Fig.IV.4: The ACSpect: the vacuum case of the MST sealed by the converter and coupled with the PMT.

IV.2 Experimental Setup

During the measurement campaigns, the MST stages were biased and connected to two different electronic chains, utilized to amplify and shape the signals generated by the interacting radiation. In particular, the ΔE stage was connected to a standard Ortec 671 amplifier module, the common p^+ layer was biased at an operative voltage of -6 V and connected to a Ortec 671 module, and the E stage was biased with an operative voltage of +150 V. The preamplifiers were powered with a ±12 V source. The shaping times were set at 3 μs for the ΔE stage and 2 μs for the common layer, in order to maximize the signal to noise ratio.

The PMT was powered with a +5 V source, and the output signals were amplified with a Silena 7611 standard amplifier module, able to set a fast shaping time of 250 ns.

The output signals of the three chains were acquired by a commercial fast digitizer, Pico Technology's PicoScope 4424 [59], controlled by the dedicated software described in the next chapter. The device has a 12 bit resolution, and it was set to acquire signals from three input channels at a sampling frequency of 20 MS/s, using the ΔE signals as trigger events.

A scheme of the whole ACSpect chain is shown in Fig.IV.5.

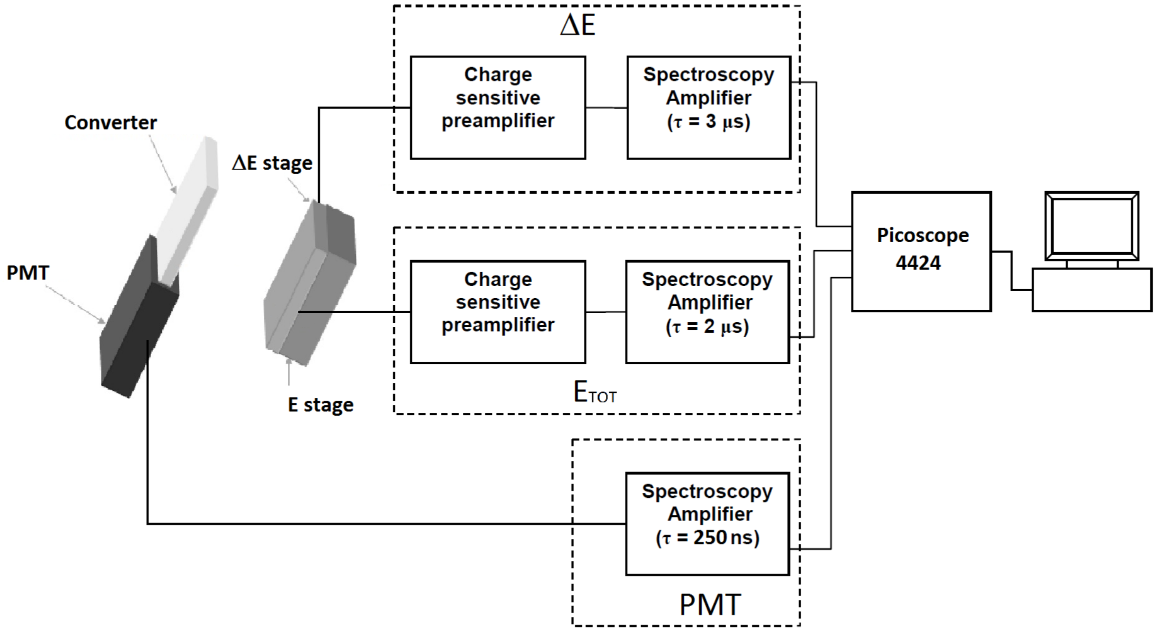

Fig.IV.5: Scheme of the ACSpect chain.

IV.3 Energy calibration

The ΔE and E_{TOT} chains were calibrated through a electronic calibration procedure. The deposited energy and the generated charge are related as follows:

$$E = \frac{Q \cdot \varepsilon_{Si}}{e} , \tag{IV.1}$$

where e is the charge of the electron ($1.602 \cdot 10^{-19}$ C), ε_{Si} is the mean energy required to create an electron-hole pair in silicon (3.62 eV).

By knowing the value of a test capacitance Cinj, the charge generated by a signal test of amplitude Vtest is:

$$Q_{test} = V_{test} \cdot C_{inj} \ . \tag{IV.2}$$

From (IV.1) and (IV.2) we can obtained the relation:

$$E_{test} = \frac{V_{test} \cdot C_{inj} \cdot \varepsilon_{Si}}{e} , \tag{IV.3}$$

which gives the equivalent energy.

With (IV.3) it is possible to calculate the energy associated to test pulses and calibrate the complete chain.

As far as the active converter chain is concerned, the light generation is not linearly related to the energy deposited in the scintillator as discussed in the previous chapter.

From the non-linearity analysis (III.3):

$$L = \int_0^{E_p} \frac{1}{1 + k_B \cdot \left(\frac{dE}{dx}\right)^{poly}(E)} dE ,$$

we can link the energy, in eV, to the light expressed in arbitrary units. By calibrating the acquired signals distribution (Fig.IV.6, black) with the non-linear simulated light curve (green), the obtained corrected events (red) are actually the events calibrated in terms of energy.

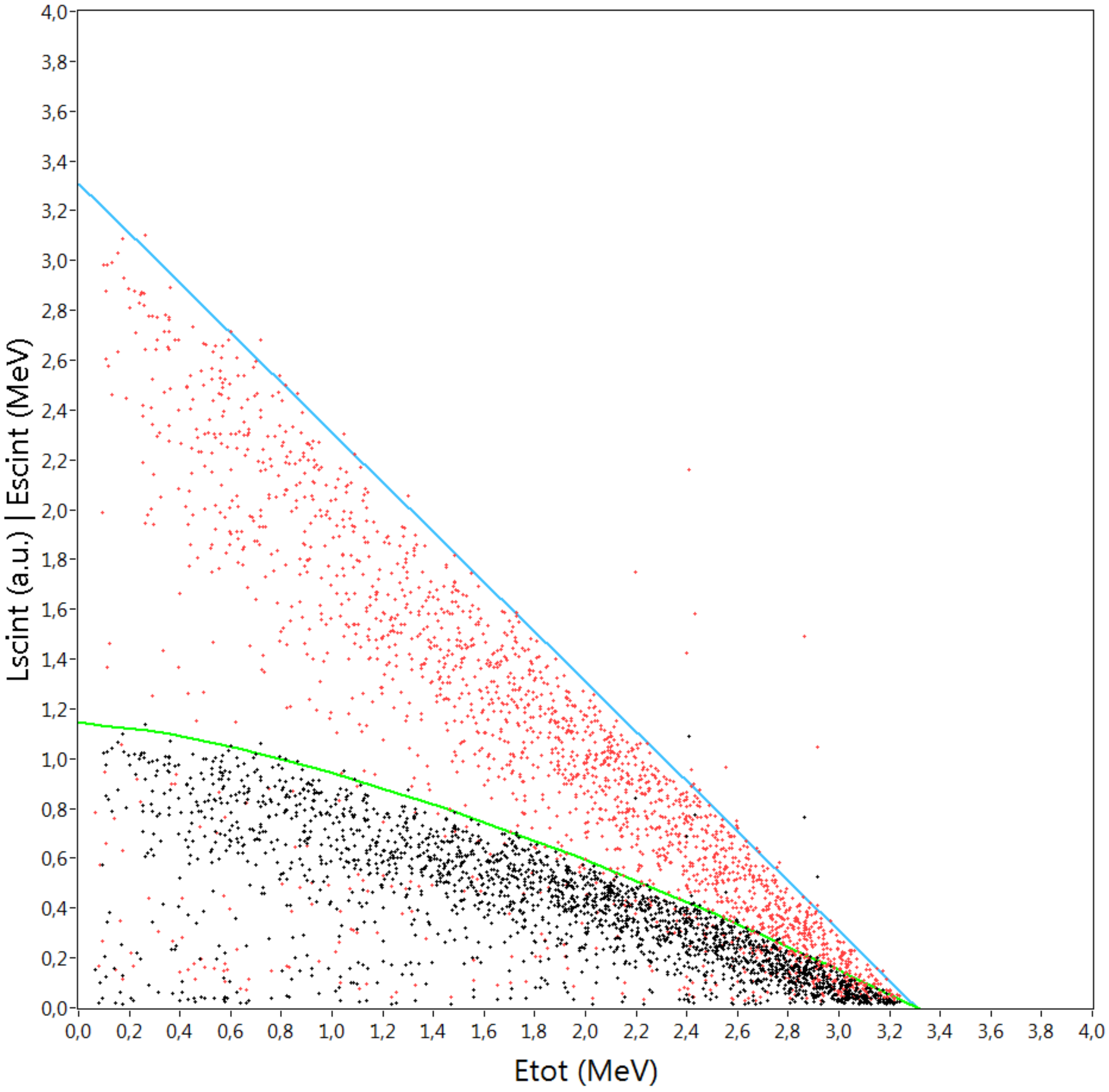

Fig.IV.6: E_{scint}-E_{TOT} scatter plot: by matching the acquired events distribution (black) with the non-linear trend (green), the corrected events (red) are properly calibrated in energy.

Chapter V

DATA ACQUISITION AND PROCESSING SOFTWARE

In order to allow the ACSpect to perform real-time spectrometry, a dedicated LabVIEW software was developed to deal with the main processing issues: data sampling and acquisition, triple timing coincidence, particle discrimination, non-linear light generation correction.

Part of the digital control routines, the whole calibration, coincidence, discrimination, correction and time analysis routines and part of the spectra and scatter plot routines were specifically developed for this software.

As mentioned in the previous chapter, the output signals of the ACSpect were acquired by a PicoScope 4424. The digitizer control and data sampling procedures have been developed on libraries provided by Pico Technology.

In real-time, the processing software manages:

- Signal peak search based on a quadratic fit;
- Energy calibration (energy for ΔE and E_{TOT} stages and arbitrary light units for the PMT);
- Triple coincidence between the three stages of the ACSpect and discrimination of the proton-related events;
- Non-linear light generation correction procedure;
- Calculation and display of spectra related to accepted and rejected events of the three stages, corrected events for the converter, total energy events for protons, neutron spectrum (by taking into account eq. (1)), and 2D scatter plots related to ΔE- E_{TOT} distribution, E_{tel}-E_{scint} distribution.

The software is able to perform post-processing for time coincidence analysis and 3D scatter plot generation.

V.1 Peak detection, energy calibration, timing coincidence and proton discrimination

The detection of signal peaks is performed by a LabVIEW built-in algorithm that fits a quadratic polynomial to sequential groups of data points when a minimum number of samples are above a selected threshold.

After the calibration, the time coincidence between the three stages events (ΔE stage, E_{TOT} stage, converter-PMT) and the associated event discrimination are performed by referring to the ΔE output, used as trigger for the data acquisition. A LabVIEW diagram of routines for peak searching (red), calibration (green) and coincidence calculation (blue) is shown in Fig.V.1.

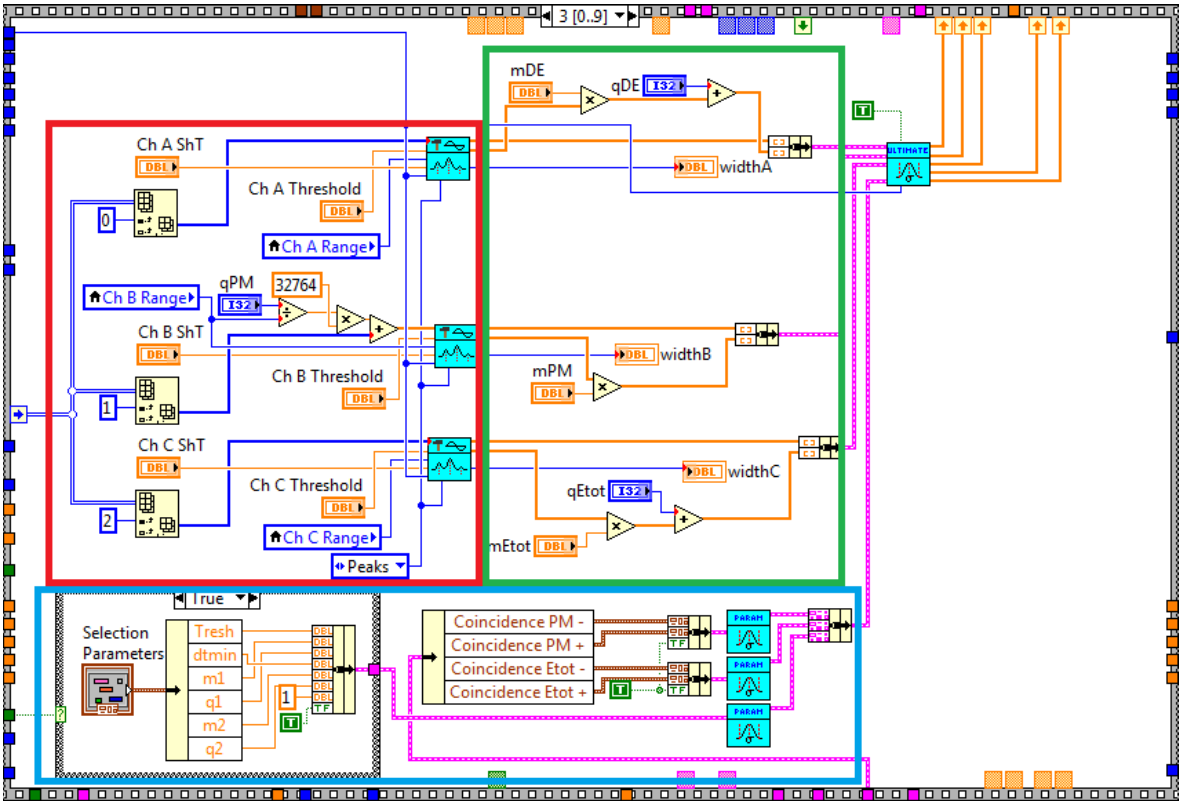

Fig.V.1: LabVIEW diagram of the peak search (red), calibration (green) and coincidence parameters calculation (blue).

The software described above was tested for the experimental characterization of the ACSpect. The ACSpect was irradiated with 3.31 MeV monoenergetic neutrons at the Legnaro National Laboratories of INFN (see preliminary tests in Chapter III and Chapter IV). Fig.V.2 shows the results of processing carried out by the time coincidence analysis routine, which calculate the distribution of events in terms of time of arrival with respect to the trigger reference. As can be observed in Fig.V.2, left side, the time distribution of events generated in PMT with respect to those in ΔE highlights the presence of a first population concentrated in a small region and a second one sparsely distributed over a wide time interval. The former is due to recoil-protons which generate in PMT and in MST pulses with a clear time correlation (an average delay of about 8 us, with a dependence on the energy deposited in the ΔE stage due to the threshold timing technique). The latter can be associated to uncorrelated events in the PMT and MST (false coincidence) generated by the strong γ background. The distribution of proton-related events can be isolated as shown in Fig.V.2, right side, by performing a time-energy shaped coincidence (gray lines). The obtained distribution still includes undesired events, mainly at low ΔE energies.

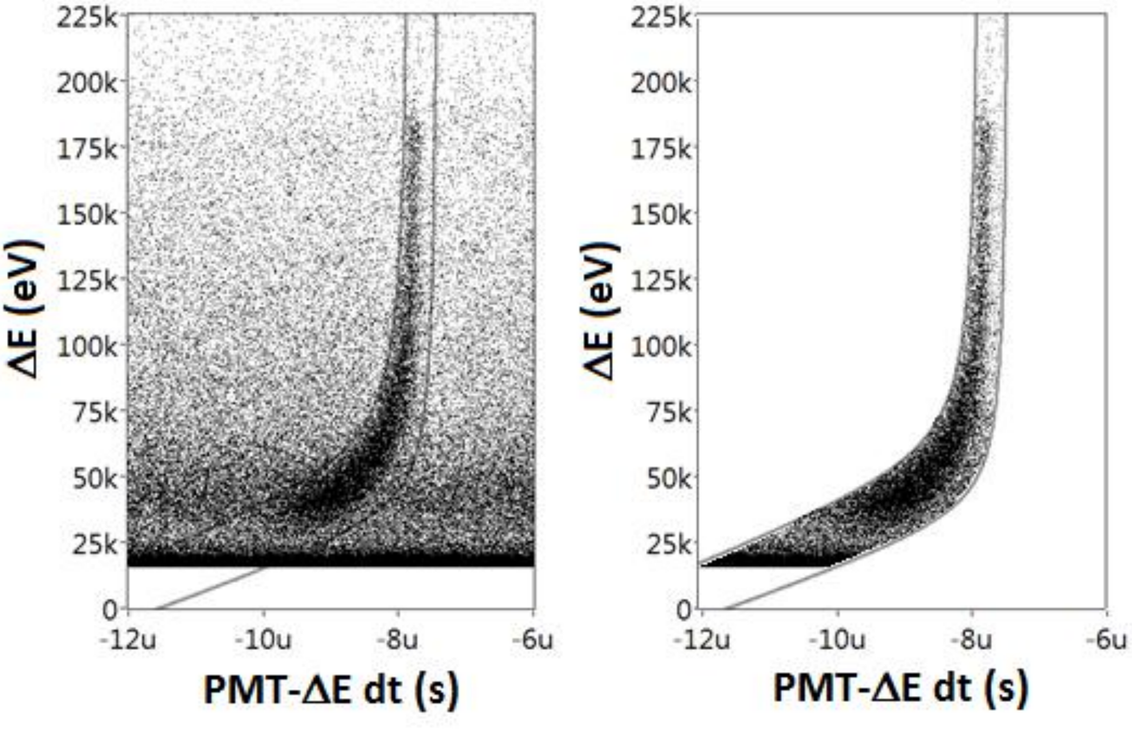

Fig.V.2: Time coincidence between events collected in the PMT and in the ΔE stage at different ΔE energy values: interval selection (left) and time-energy shaped selection (right).

The ΔE-E$_{TOT}$ events can be coupled with a simple time coincidence procedure by comparing the E$_{TOT}$ events time positions with a time interval fixed with respect to the ΔE events. After this time coincidence, by exploiting the ΔE-E$_{TOT}$ scatter plot (Fig.V.3) the protons distribution (black) can be easily discriminated (black lines) from other kind of events (gray).

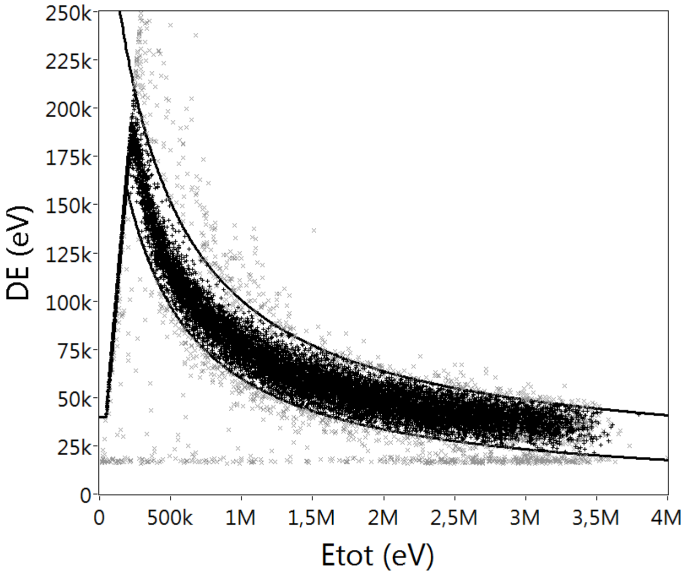

Fig.V.3: ΔE-E$_{TOT}$ scatter plot.

Diagrams of the time coincidence procedure and the proton ΔE-E$_{TOT}$ selection can be seen in Fig.V.4 and Fig.V.5 respectively.

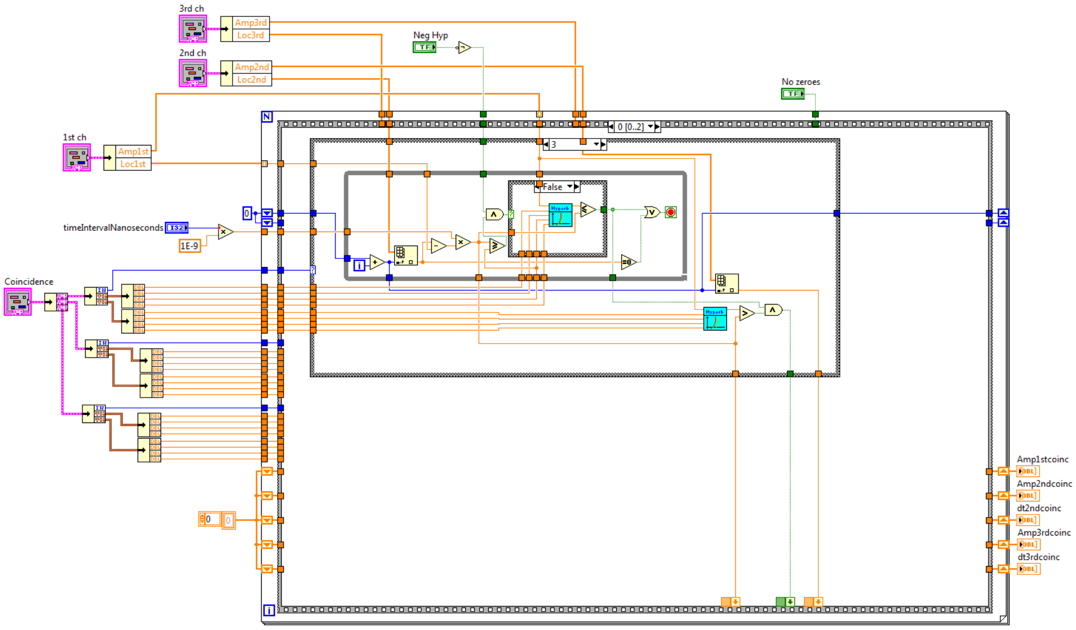

Fig.V.4: LabVIEW diagram of the timing coincidence procedure for two coupled channels.

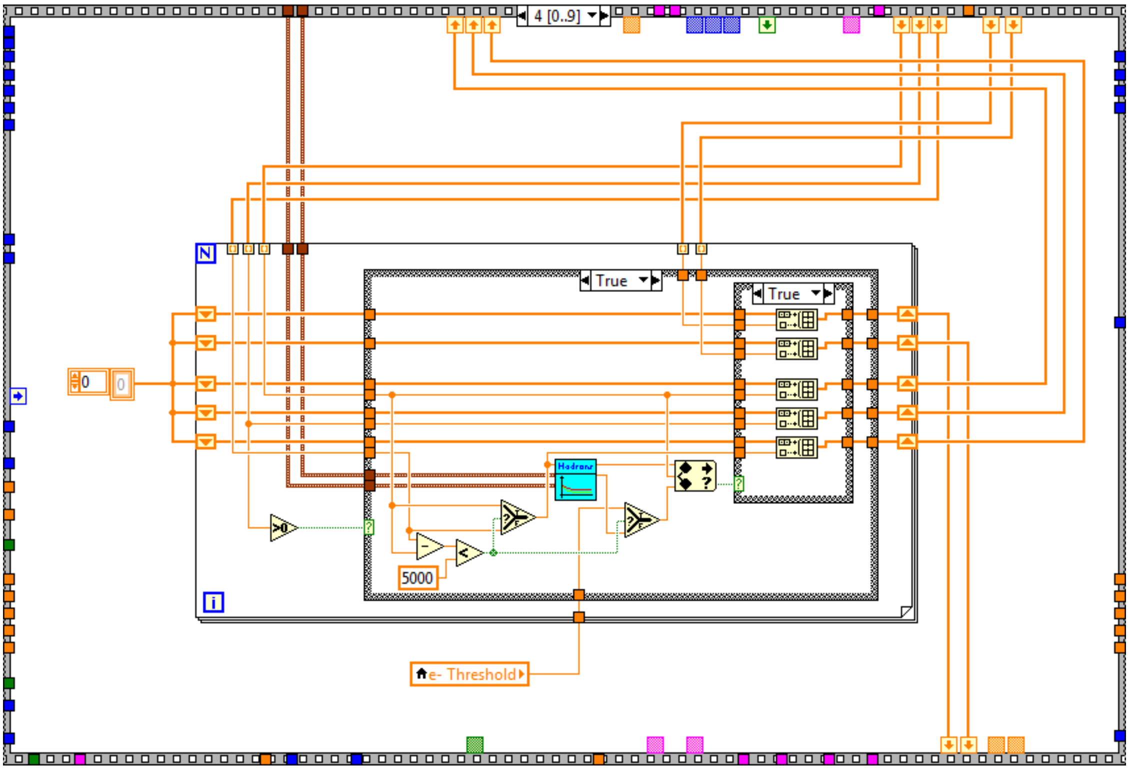

Fig.V.5: LabVIEW diagram of the ΔE-E_{TOT} proton selection.

By considering the effect of both the discrimination procedure based on the ΔE-E_{TOT} scatter plot and that based on ΔE-PMT time coincidence, the processing software allows to derive the distribution of events due to recoil-protons only in a very effective way (see Fig.V.6, right side).

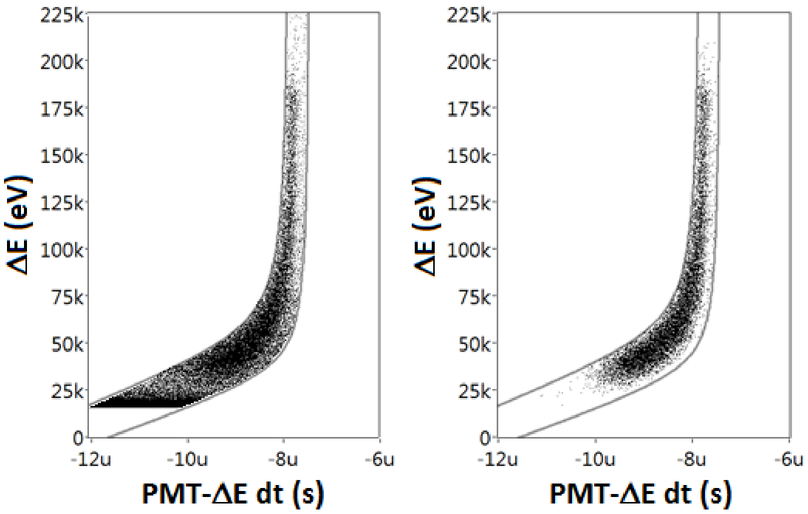

Fig.V.6: Time coincidence between events collected in the scintillator and in the ΔE stage at different ΔE energy values: before (left) and after the ΔE-E_{TOT} proton selection (right).

For a better analysis of the time-energy distributions, a procedure was developed to perform a post-processing analysis of the whole measurement. For the detected ΔE events, this algorithm calculate the time-energy distributions. The diagram of the described procedure is shown in Fig.V.7.

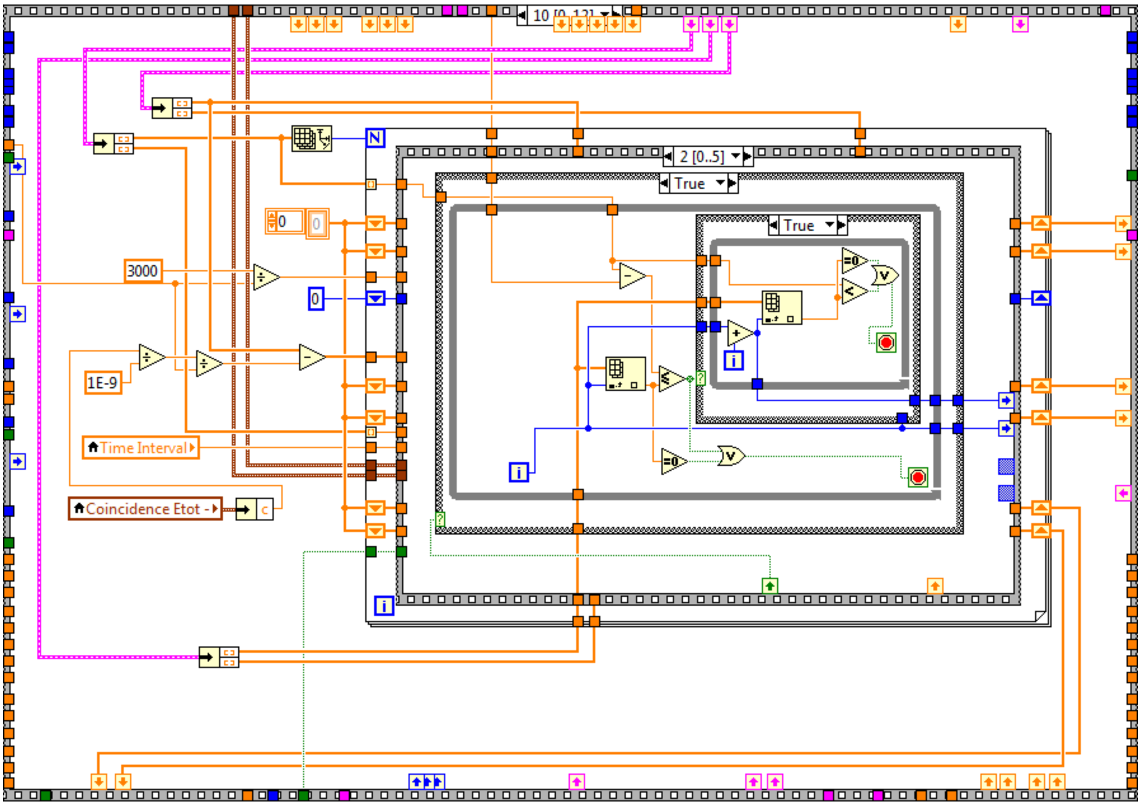

Fig.V.7: LabVIEW diagram of the time-energy distributions analysis procedure.

V.2 Non-linear light generation correction procedure

An algorithm was developed in order to recover the energy information provided by the converter starting from the non-linearity model discussed in Chapter III, Paragraphs 7-8. The correction procedure was implemented in the LabVIEW code by using the energy-dependent proton stopping power tables given by the ICRU 49 report [37]. In particular those tables was used to implement the correction procedure by interpolating them with a cubic spline curve.

The diagram of the non-linear light generation correction algorithm is shown in Fig.V.8.

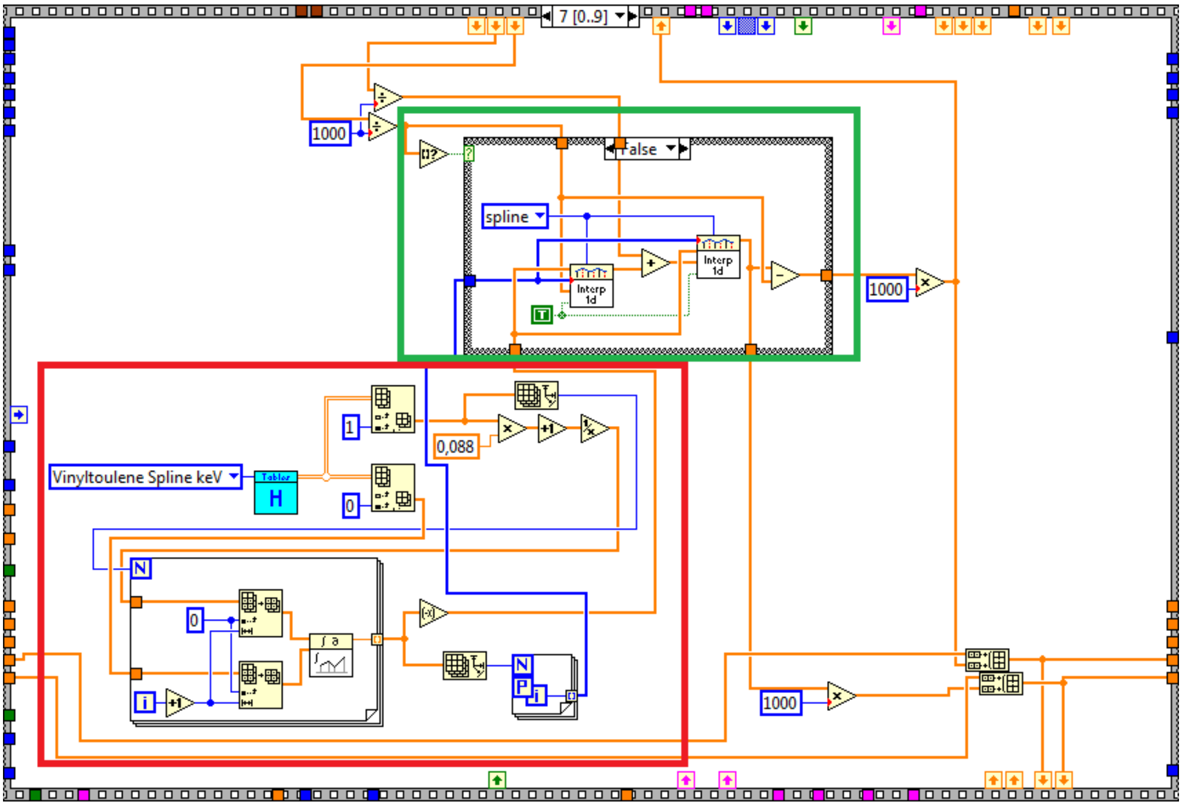

Fig.V.8: LabVIEW diagram of the non-linear light generation correction procedure: the (III.3) model (red) and the interpolation and correction algorithm (green).

V.3 Spectra and scatter plots display

The software was developed to calculate and display all measurement information of interest: spectra related to accepted and rejected events, energy distributions of accepted events, final recoil-proton spectrum and neutron spectrum. It also generates 2D scatter plots of ΔE- E_{TOT} distributions, E_{TOT}-E_{scint} distributions and, in post-processing, also 3D scatter plots for the energy and time distribution analysis.

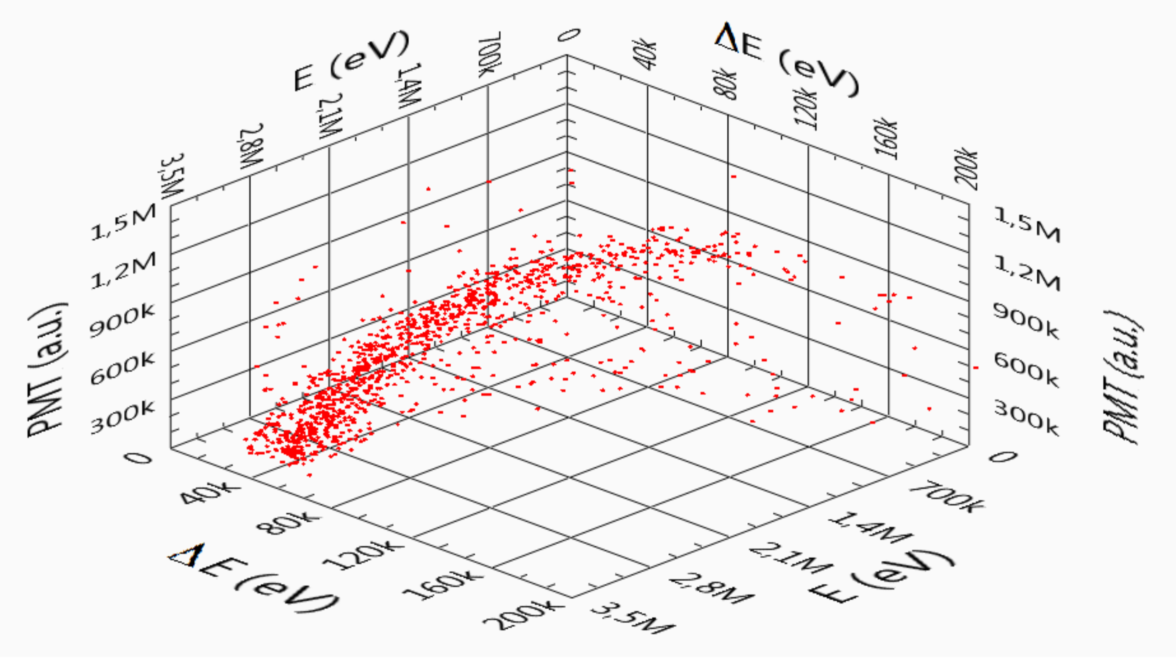

Fig.V.9: 3D scatter plot for 3.31 MeV monoenergetic neutrons.

The final neutron spectrum, i.e. the goal of the ACSpect, is obtained by dividing the recoil-proton total energy spectrum by the probability $\pi(E_n)$ of generating a recoil-proton in the polyvinyltoluene (II.14):

$$\pi(E_n) = A \cdot \int_{L-R^{poly}(E_n)}^{L} e^{-\Sigma_{tot}\cdot x} \cdot \Sigma_H \cdot dx \,,$$

By taking into account i) the distance of the measurement position with respect to the target, ii) the total charge accelerated during the measurement and iii) the geometric efficiency of the spectrometer, the neutron spectrum can be also calculated.

The software can then compare the growing spectrum with a previously loaded one.

Fig.V.10 shows the LabVIEW diagram corresponding to the neutron spectrum calculation, normalization and comparison.

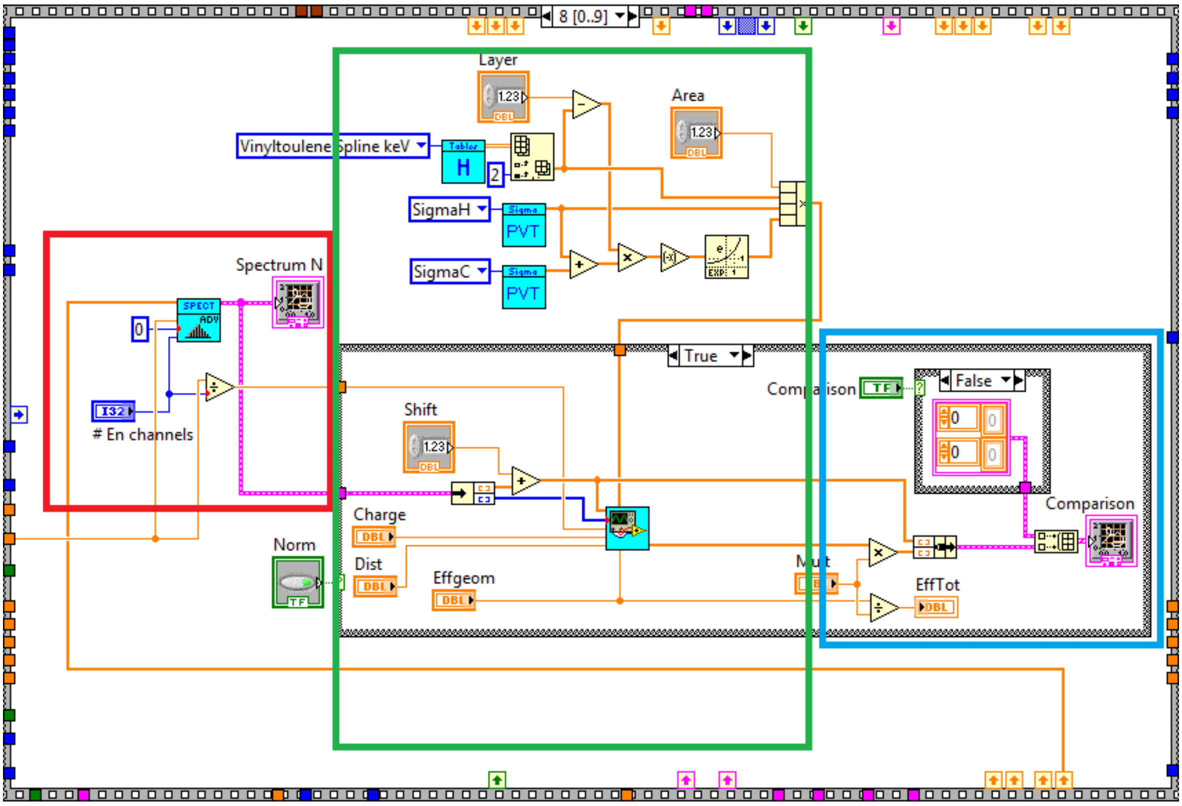

Fig.V.10: LabVIEW diagram of the neutron spectrum calculation (red), normalization (green) and comparison (blue).

It must be underlined that except for the 3D plots and the post-processing time coincidence analysis, all the described procedures (peak detection, energy calibration, timing coincidence, proton discrimination, non-linearity correction, neutron spectrum calculation, normalization and comparison) work together online during the acquisition.

In particular, the innovative algorithms implemented in the timing coincidence/proton discrimination and in the non-linearity correction constitute important achievements for the operative management of the ACSpect.

Chapter VI

EXPERIMENTAL CHARACTERIZATION AND RESULTS

The detection system (and the dedicated software for data acquisition and processing) described in details in Chapters IV and V was experimentally tested and characterized with neutron fields in order to verify its capability of measuring spectra in real-time, that is without the need of an unfolding procedure.

A first measurement campaign was performed with quasi monoenergetic neutrons generated by bombarding a thin lithium fluoride target with protons. This allowed to study the spectrometer response at energies lower than 5 MeV. The detection system was then tested in neutron fields with spectral fluence continuously distributed produced by a thick beryllium target bombarded with protons and deuterons.

All irradiations were carried out at CN Van De Graaff accelerator of the Legnaro National Laboratories of the INFN.

VI.1 Preliminary characterization of ACSpect response to monoenergetic neutrons

The ACSpect, whose experimental setup is described in Chapter IV, Paragraph 2, was characterized with monoenergetic neutron beams generated by bombarding with protons a thin LiF target (700 $\mu g \cdot cm^{-2}$). Neutrons are produced via the $^{7}Li(p,n)^{7}Be$ reaction at proton energy higher than the threshold energy E_{th} = 1.88 MeV. Another reaction channel contributes at energies higher than 1.88+0.43 MeV via the $^{7}Li(p,n)^{7}Be^{*}$ which lead to the production of neutrons from the 0.430 MeV excited level of ^{7}Be.

Table VI.1 lists the energy and fluence values of neutron fields which can be produced via the reactions mentioned above at different proton energies.

Proton Energy (MeV)	^{7}Li(p,n) ^{7}Be		^{7}Li(p,n) ^{7}Be*	
	Mean Neutron Energy (MeV)	Fluence @ 10 cm (cm^{-2}mC^{-1})	Mean Neutron Energy (MeV)	Fluence @ 10 cm (cm^{-2}mC^{-1})
2.40	0.636	$1.23 \cdot 10^{5}$	-	-
3.00	1.272	$5.02 \cdot 10^{4}$	0.794	$3.88 \cdot 10^{3}$
4.00	2.296	$3.90 \cdot 10^{4}$	1.842	$4.66 \cdot 10^{3}$
4.40	2.702	$4.55 \cdot 10^{4}$	2.251	$4.20 \cdot 10^{3}$
5.00	3.309	$7.06 \cdot 10^{4}$	2.862	$3.85 \cdot 10^{3}$
5.60	3.914	$4.83 \cdot 10^{4}$	3.470	$6.37 \cdot 10^{3}$

Table VI.1: Neutrons produced by protons on a 700 μg·cm^{-2} LiF target at 0°.

The spectrometer was placed at 0° with respect to the proton beam direction of incidence. The distance between the target and the converter was 17 mm. This resulted in a detection efficiency of the order of 10^{-6} counts per unit neutron fluence.

The accelerated charge of the proton beam was measured with a Faraday cup connected to a charge integrator.

For the first characterization series, the ACSpect was irradiated with neutrons of 0.636, 1.272, 2.702, 3.309 and 3.914 MeV.

Fig.VI.1 shows the experimental scatter plot of the energy deposited in the converter E_{conv} versus the energy E_{TOT} deposited in the whole silicon detector.

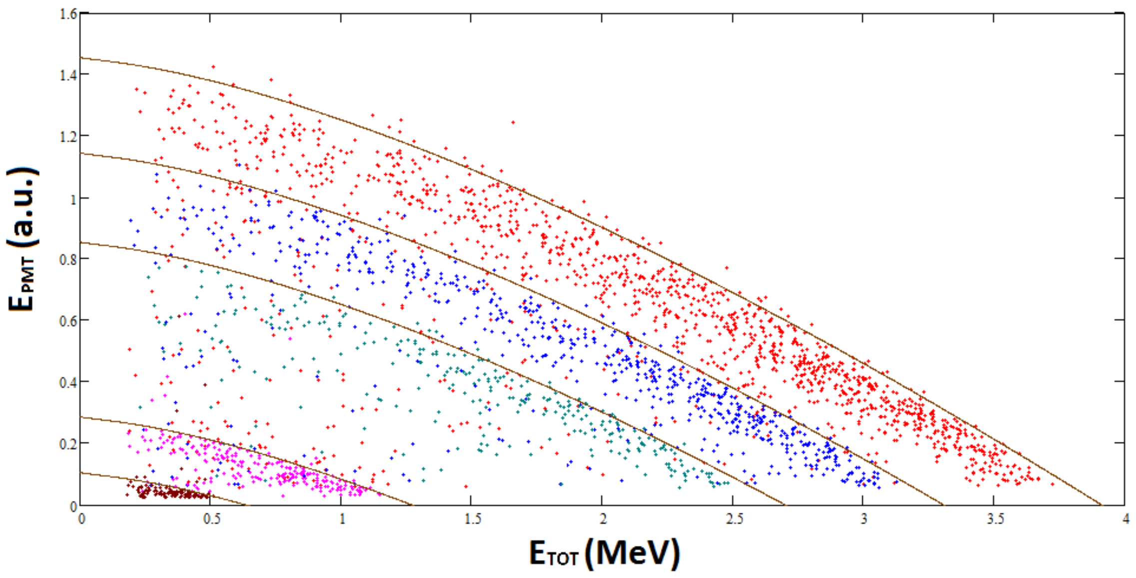

Fig.VI.1: E_{PMT}-E_{TOT} scatter plot: 0.636 MeV (ruby), 1.272 MeV (pink), 2.702 MeV (green), 3.309 MeV (blue) and 3.914 MeV (red), with the corresponding analytical curves (brawn lines).

The distributions of energy deposited in the three different stages of the ACSpect, i.e. converter, ΔE stage and E stage, are shown in Fig.VI.2, 3 and 4 together with the distributions calculated through the analytical model described in Chapter II.

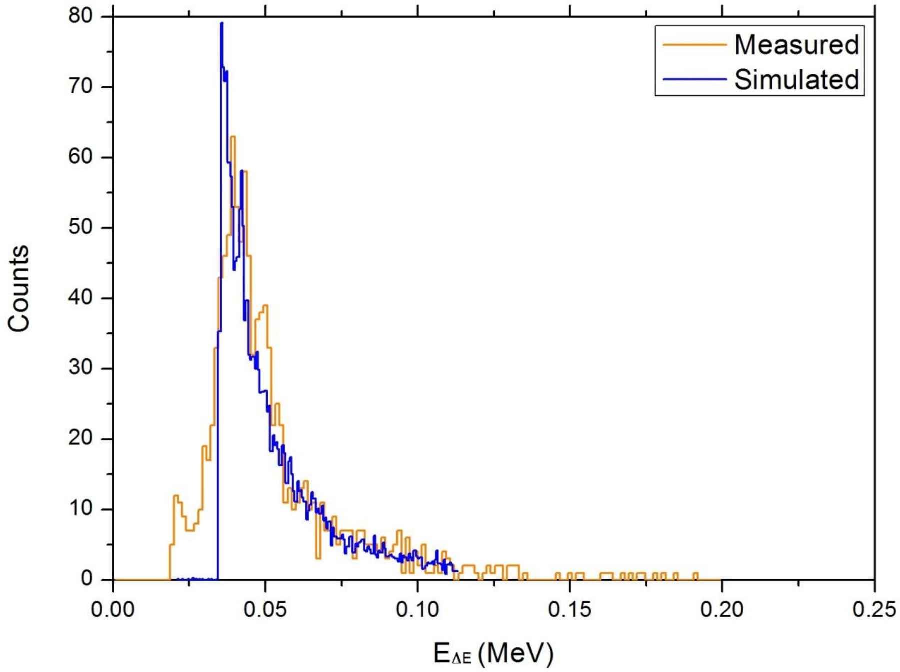

Fig.VI.2: ΔE spectra measured by the ACSpect (orange) compared with the analytical result(blue) for neutrons produced by 5 MeV protons on LiF.

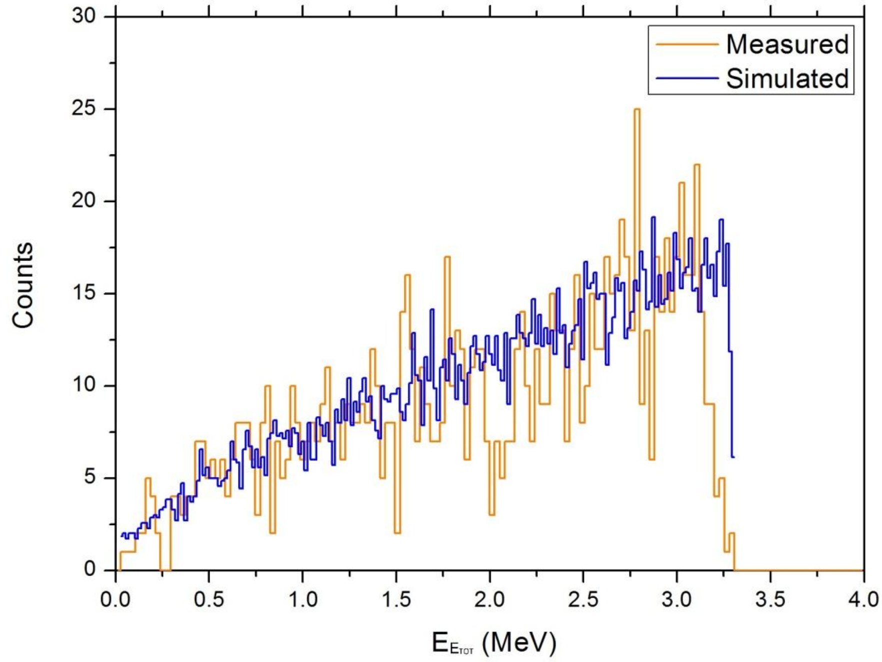

Fig.VI.3: Etot spectra measured by the ACSpect (orange) compared with the analytical result(blue) for neutrons produced by 5 MeV protons on LiF

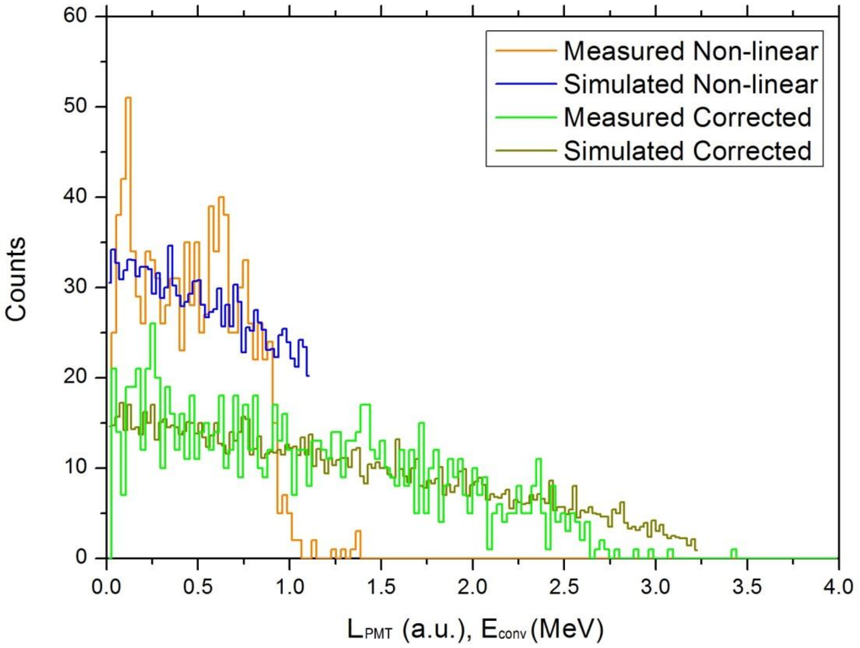

Fig.VI.4: Spectra of the energy Econv deposited in the converter measured by the ACSpect (orange) compared with the analytical result(blue) for neutrons produced by 5 MeV protons on LiF.

The spectral fluence distributions of the neutron fields were reconstructed with the correction algorithm described in Chapter IV. The final spectra obtained with 2.3 MeV neutrons is shown in Fig.VI.5.

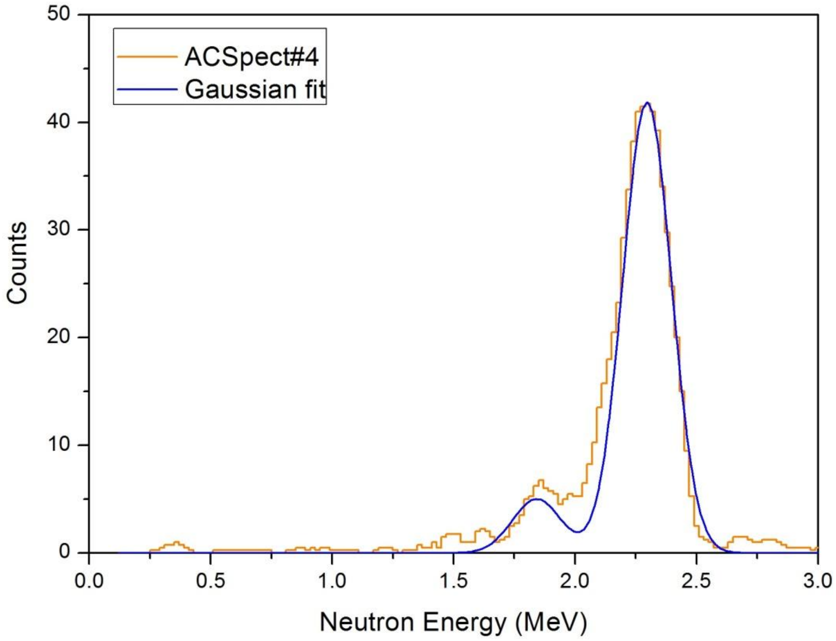

Fig.VI.5: Spectrum of 2.3 MeV monoenergetic neutrons measured with the ACSpect.

The measured energy distribution was fitted with two Gaussian curves. The fitting procedure was carried out by calculating the best Gaussian fit for the main peak (the main reaction channel) and by deriving the second fitting function (the secondary reaction channel) by assuming the same variance obtained for the main peak and by considering the expected energy difference (0.48 MeV) and fluence ratio (0.055). With respect to the fitting curve, the measured spectrum shows an asymmetry, a low energy tail. This can be due to different non idealities, mainly the not perfectly straight trajectory of recoil-protons, the roughness of the active converter surface and the actual energy distribution of accelerated protons (scattered component).

Fig.VI.6. shows the measured spectral fluence distributions of neutron fields at different energies as reconstructed by the correction algorithm in real-time.

The energy resolution of the spectrometer resulted to be about 235 keV in FWHM at 3.31 MeV, which corresponds to the a value of about 7 %.

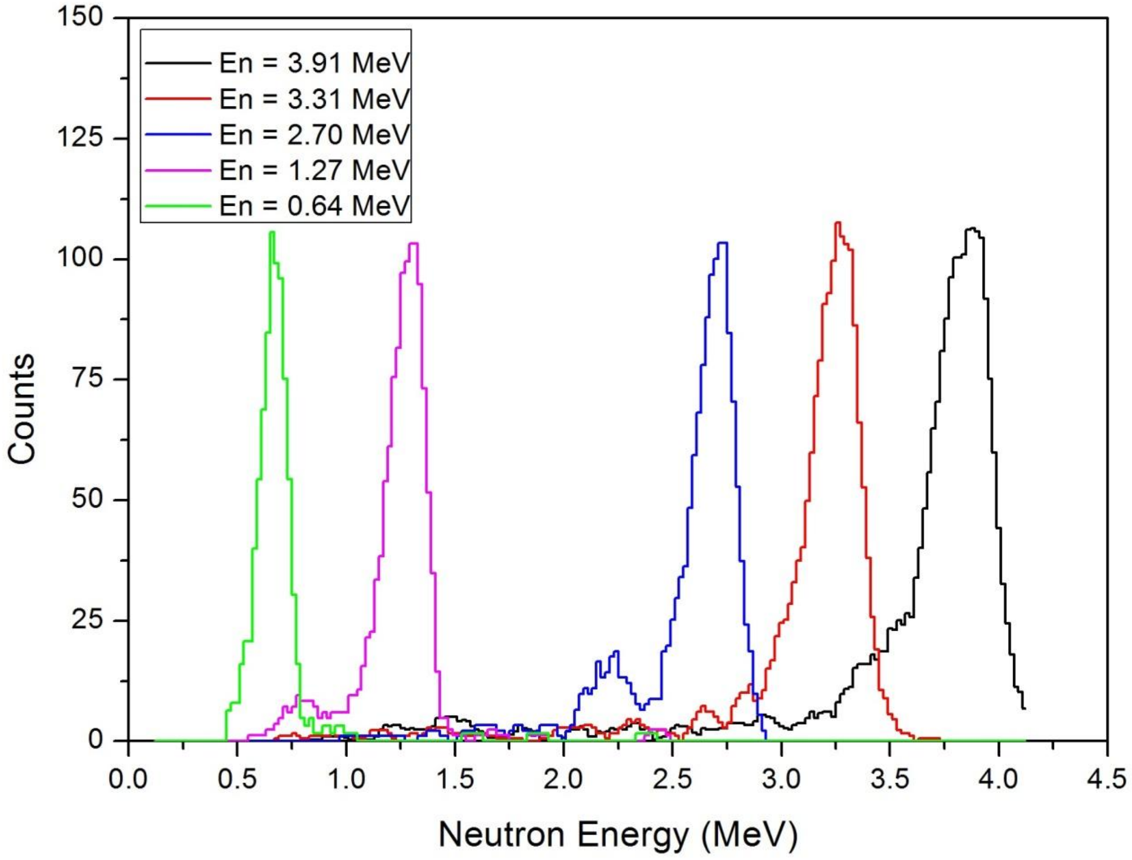

Fig.VI.6: Spectra of monoenergetic neutrons acquired with the ACSpect.

The results obtained with the ACSpect can be compared with those presented in literature by Tomita et al. [60]. The spectrometer proposed by this research group consists of a thin plastic scintillator which acts as a neutron converter, a silicon surface barrier detector (Si-SBD) used for recoil proton detection and a second thick plastic scintillator for detecting the scattered neutrons. Here, the radiator works as a ΔE detector and as fast timing detector for the time of flight measurements. To avoid recoil-protons energy loss, part of the system is set in vacuum. The energy of the recoil proton E_{rp} is given by the sum of the energy deposition in the thin plastic scintillator E_{rad} and in the Si-SBD E_{prd}, which is like a recoil proton telescope. In parallel, the energy of the scattered neutron E_{sn} is measured by ToF technique. The energy of the incident neutron E_{in} is, therefore, derived as follows:

$$E_{in} = E_{rp} + E_{sn} = \left(E_{rad} + E_{pd}\right) + \frac{1}{2} m_n \left(\frac{LT}{t_{ToF}}\right)^2 , \qquad \text{(VI.1)}$$

where m_n is the mass of the neutron, LT is the distance from the radiator to the scattered neutron detector, and t_{ToF} is the time of flight between the radiator and the scattered neutron detector.

The system studied by Tomita et al. was used to measure 2.5 MeV neutrons from the DD reaction. The measured spectrum was characterized by a resolution of 6.3% (FWHM) and a detection efficiency of $3.3 \cdot 10^{-7}$ counts per neutron generated.

Fig.VI.7 shows the scheme of experimental setup of the Japanese spectrometer.

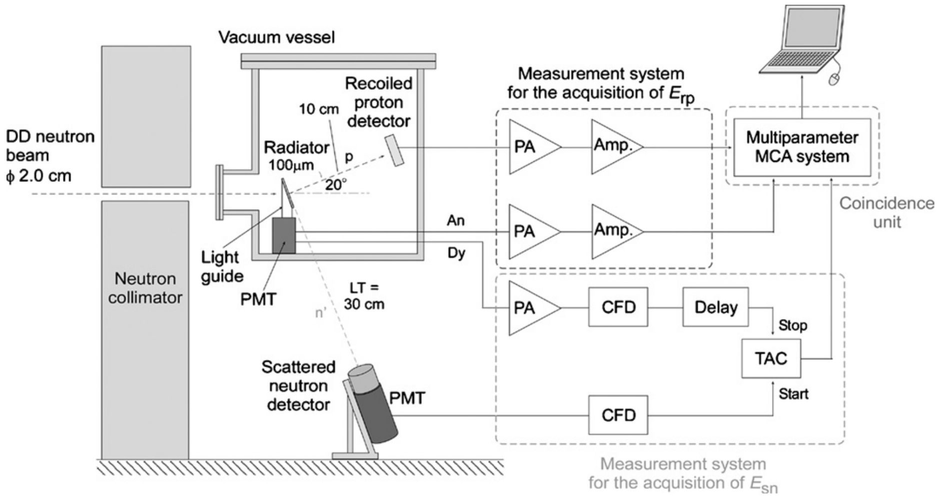

Fig.VI.7: Scheme of the experimental setup of the spectrometer proposed by Tomita et al. [60].

The ACSpect and the spectrometer developed by Tomita et al. result to have similar performance. However, the ACSpect is characterized by a simpler, transportable and more compact layout and does not require a thin (100 μm) converter.

VI.2 Irradiations with continuous spectra: Protons on Beryllium

In the last years the use of an accelerator-based high flux thermal neutron beam for Boron Neutron Capture Therapy (BNCT) treatments of shallow tumors has been studied in several works, like the SPES-BNCT project at INFN-LNL [61]. The use of ^{9}Be(p,xn)^{9}B reaction has been investigated for this application [61-77].

In order to test the capability of the ACSpect of measuring continuous neutron spectra, the detection system was irradiated at the LNL with secondary neutrons generated by protons of 4 MeV and 5 MeV striking a thick beryllium target. At a given proton energy, neutrons are produced on beryllium via the reactions ^{9}Be(p,np)2α, ^{9}Be(p,np)^{8}Be, ^{9}Be(p,n)^{9}B and ^{9}Be(p, nα)^{5}Li (threshold energy E_{th} = 1.75, 1.85, 2.06 and 3.93 MeV, respectively).

The spectrometer was placed at 0° and at a distance of about 17.5 mm from the beryllium target (Fig.VI.8).

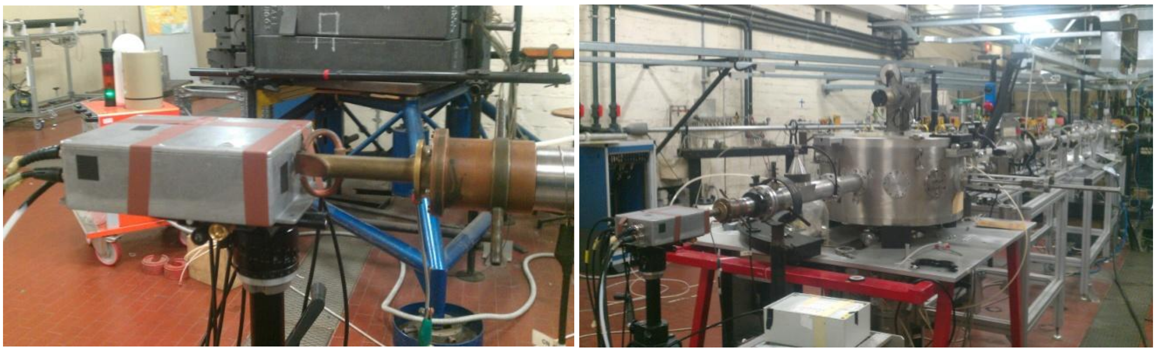

Fig.VI.8: Setup of the ACSpect at LNL: the spectrometer and the Be target (left); the beamline (right).

The spectral fluence distribution of the generated neutron field was measured and results were compared with those obtained by Howard et Al. [10] through a ToF technique. The spectra are shown in Fig.VI.9 and Fig.VI.10.

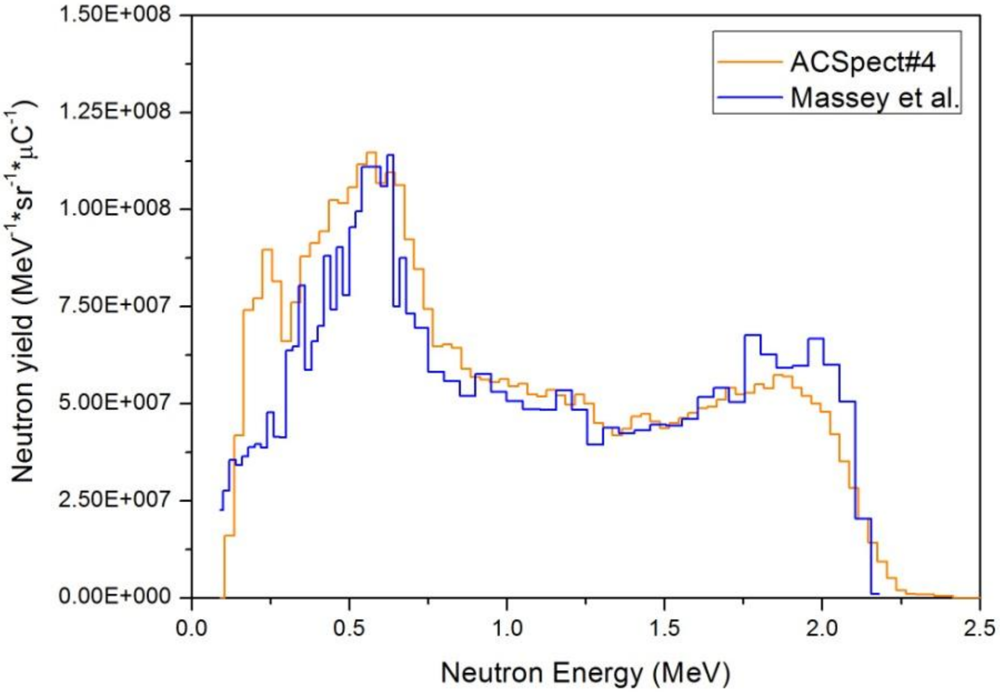

Fig.VI.9: Energy distribution of the yield of neutrons generated at 0° by 4 MeV protons on a thick beryllium target, ACSpect (orange) and ToF techniques (blue) [10].

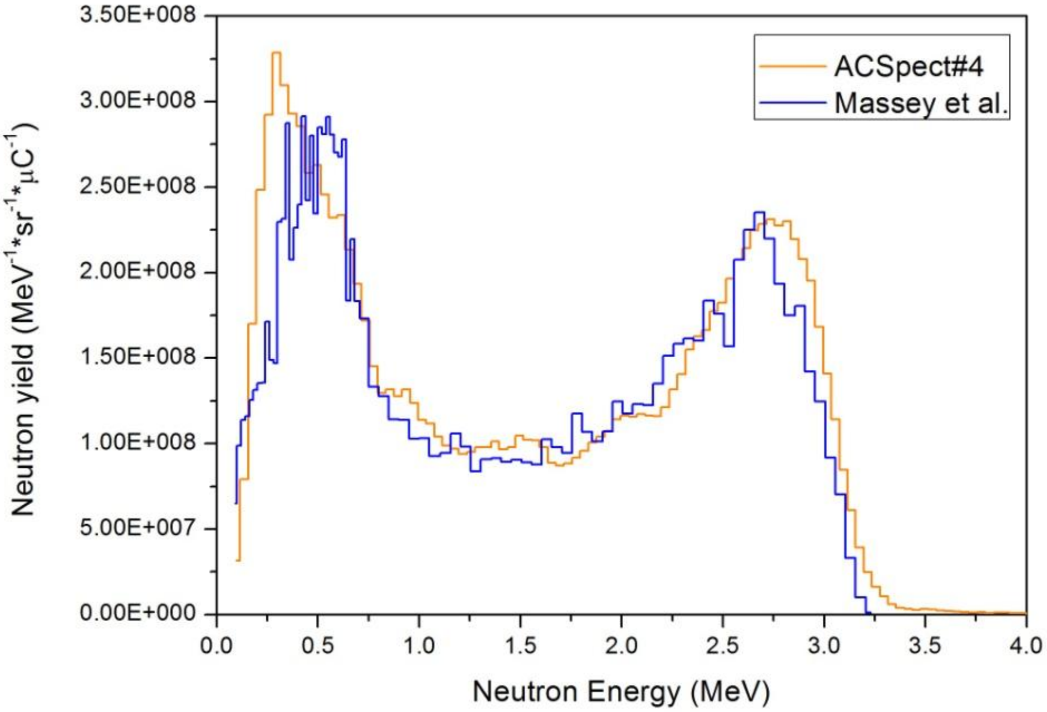

Fig.VI.10: Energy distribution of the yield of neutrons generated at 0° by 5 MeV protons on a thick beryllium target, ACSpect (orange) and ToF techniques (blue) [10].

At both considered energy, the agreement between the ToF and the ACSpect spectra is satisfactory. It should be underlined that the spectra measured by the ACSpect were acquired directly in real-time with the possibility of looking at the growing neutron distributions during the measurement time. Moreover, since the spectra are directly reconstructed from the detected events, the low detection efficiency is compensated by the necessity of only few thousand events.

VI.3 Irradiations with continuous spectra: Deuterons on Beryllium

The ^{9}Be(d,n)^{10}B reaction with deuterons incident on a thick Be target is of particular interest for applications such as activation analysis, radiography, nuclear waste assay or radiotherapy [61-77]. The reaction is exothermic with a positive Q-value of 4.36 MeV, which results in a neutron spectrum extending to quite high energies.

Neutron energy spectra and yields for the Be(d,n) reaction have been previously reported by several authors, mostly in the higher deuteron energy range.

The main characteristics of this reaction are well known but important details still have to be determined. The available data for deuteron energies $E_d < 4.0$ MeV is very fragmentary.

The ACSpect was used to measure the spectral fluence distribution of neutrons generated with deuterons of energy $E_d = 4.0$ MeV, in order to compare the results with the data measured by Guzek et Al. with ToF technique [66].

The ACSpect was placed at 0° and at the distance from target of about 22 mm.

Fig.VI.11 shows the comparison: the agreement between the ToF and the ACSpect spectra is very satisfactory.

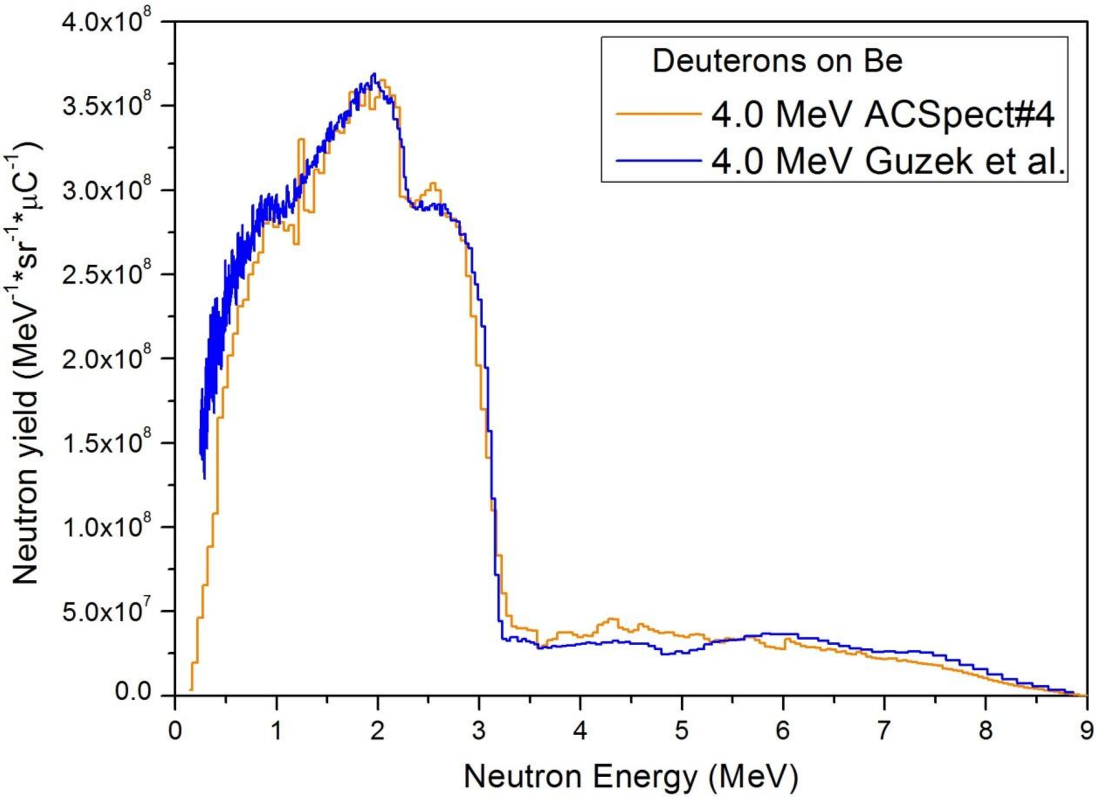

Fig.VI.11: Energy distribution of the yield of neutrons generated at 0° by 4 MeV deuterons on a thick beryllium target, ACSpect (orange) and ToF techniques (blue) [66].

The ACSpect was then employed to study the spectral fluence distribution of neutrons generated by a thick beryllium target bombarded with deuterons of energy E_d = 1.2 MeV and E_d = 1.3 MeV. The choice of these energies was mainly related to the complex structure that characterizes the spectra, so the use of a spectrometer with a good resolution becomes very important.

In order to have a qualitative comparison and to understand the general trend of the neutron yield distributions, the spectra provided by Guzek et Al. for E_d = 0.9 MeV and E_d = 1.5 MeV are reproduced in Fig.VI.12 and Fig.VI.13 respectively.

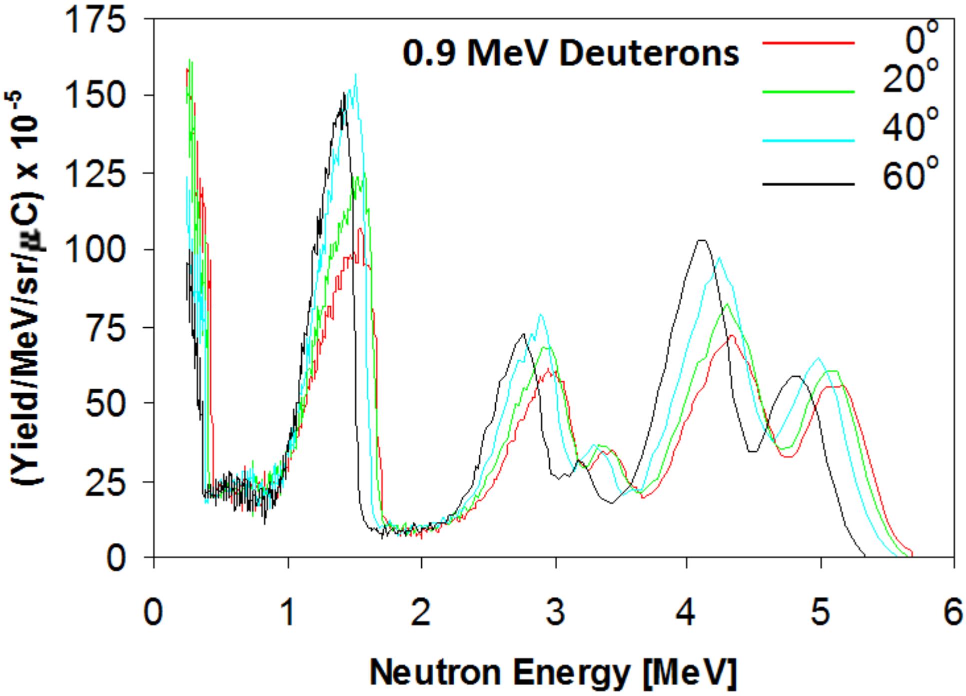

Fig.VI.12: Energy distribution of the yield of neutrons generated at several angles by 0.9 MeV deuterons on a thick beryllium target; in red the 0° spectra [66].

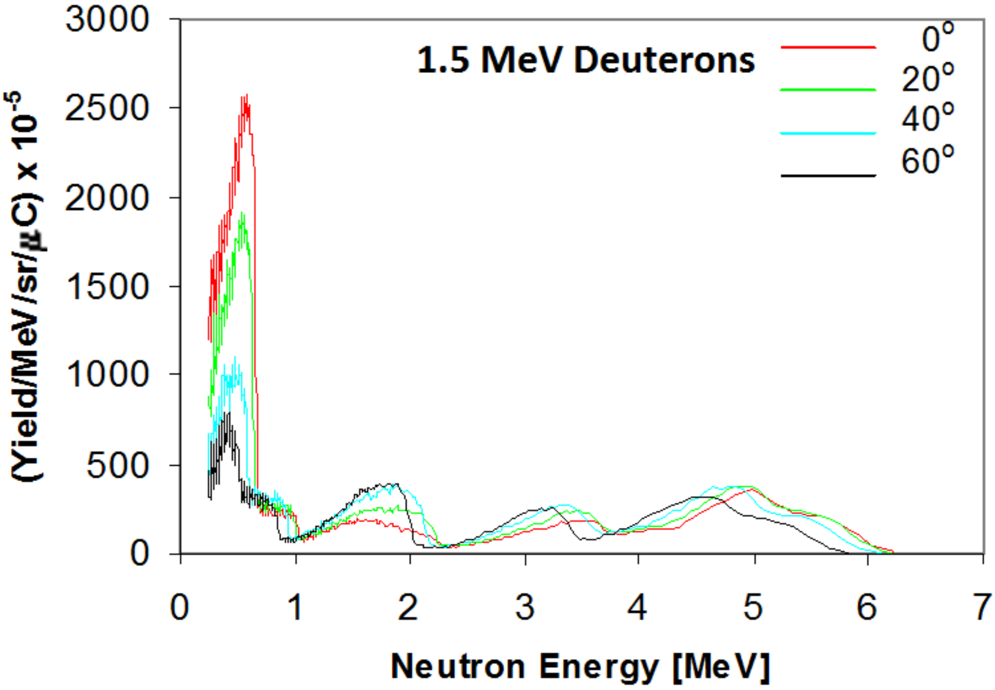

Fig.VI.13: Energy distribution of the yield of neutrons generated at several angles by 1.5 MeV deuterons on a thick beryllium target; in red the 0° spectra [66].

The complex structure of neutron spectra is mainly due to the several excited states of the ^{10}B nucleus (see Fig.VI.14).

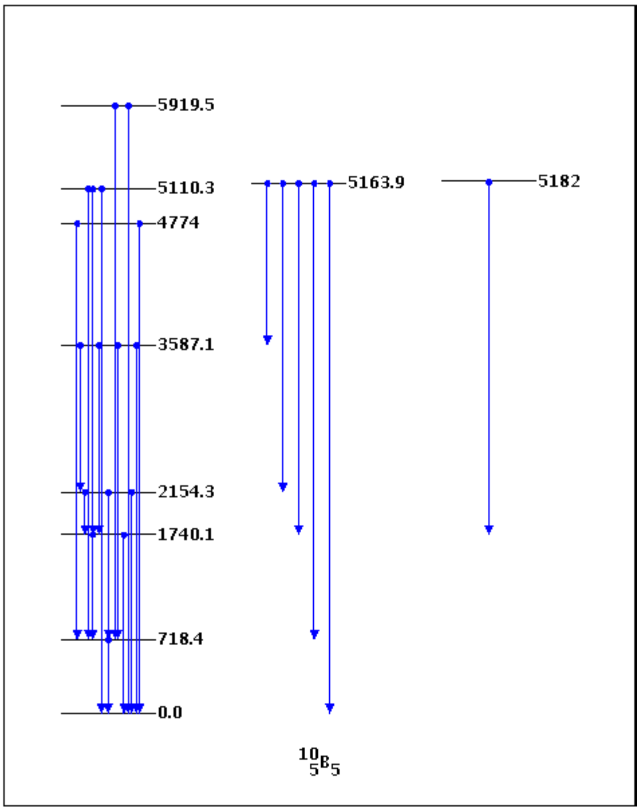

Fig.VI.14: Nuclear level structure of ^{10}B [78].

In order to simulate the response of the ACSpect, a model of the neutron source was developed. Several levels of the ^{10}B were taken into account:

Level of ^{10}B	Energy (MeV)	1.2 MeV deuterons generated neutrons (MeV)	1.3 MeV deuterons generated neutrons (MeV)
n_0	0	5,561	5,661
n_1	0,718	4,842	4,942
n_2	1,740	3,821	3,921
n_3	2,154	3,407	3,507
n_4	3,587	1,974	2,074
n_5	4,774	0,787	0,887
n_6	5,110	0,451	0,551
n_7	5,164	0,397	0,497
n_8	5,182	0,379	0,479

Table VI.2: ^{10}B energy levels and corresponding neutrons generated by the ^{9}Be(d,n)^{10}B reaction.

For every neutron group a triangular distribution was generated, with the maximum corresponding to the group energy and the minimum to the net energy of the reaction for a deuteron having E_d = 0 eV. This choice was due to take into account shape of the distributions provided by Guzek et al. A total distribution was then produced for the two considered deuterons energies by summing the groups and by convoluting the distribution with a Gaussian curve which represents the spread introduced by the system resolution. The obtained distribution was then normalized to have unitary area and used as neutron source for the ACSpect model described in Chapter II.

The simulated spectra are shown in Fig.VI.15.

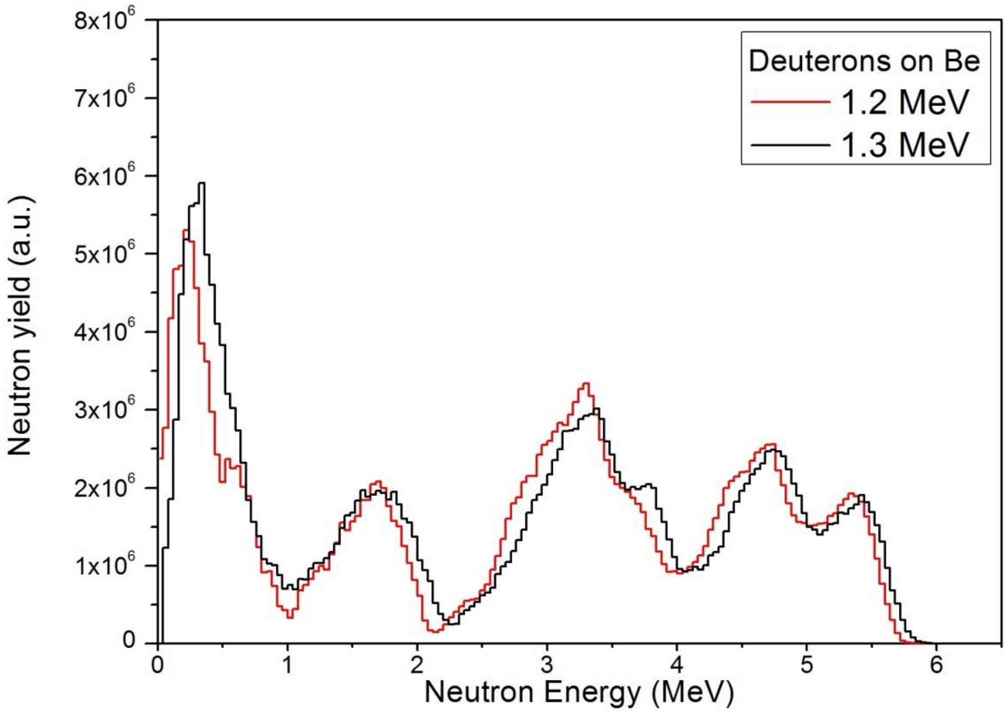

Fig.VI.15: Simulated distribution of the yield of neutrons generated at 0° by 1.2 MeV (red) and 1.3 MeV (black) deuterons on a thick beryllium target.

The ACSpect was placed at 0° and at the distance from target of about 21.5 mm. Fig.VI.16 shows the experimental results. As can be observed they are consistent with those published by Guzek et al. at energies close to that characterized in this work.

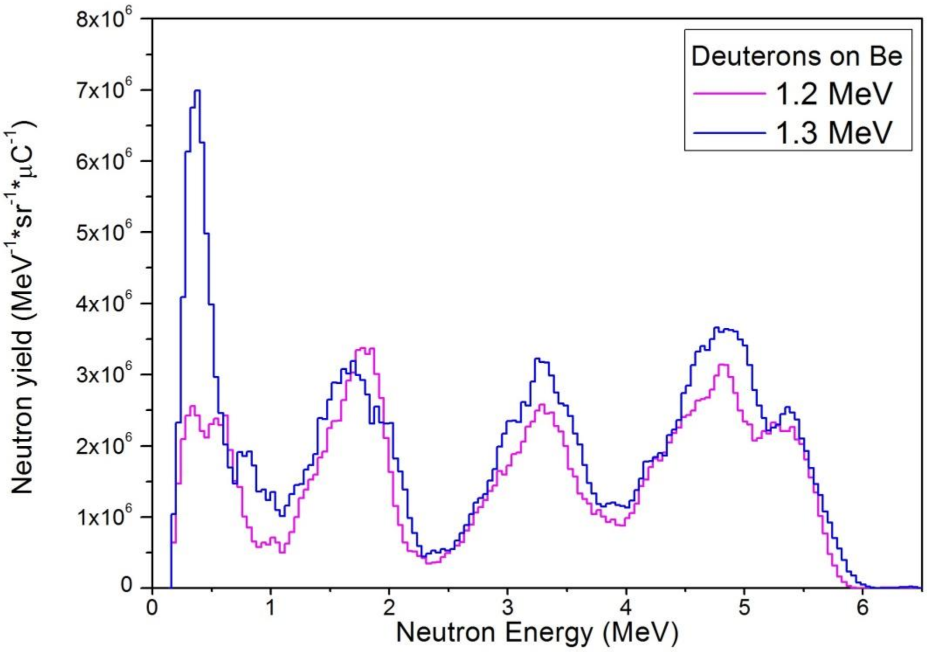

Fig.VI.16: Energy distribution of the yield of neutrons generated at 0° by 1.2 MeV (violet) and 1.3 MeV (blue) deuterons on a thick beryllium target.

Fig.VI.17 and Fig.VI.18 show the comparison between the simulated and measured distribution at the two considered deuterons energies. The agreement is very satisfactorily.

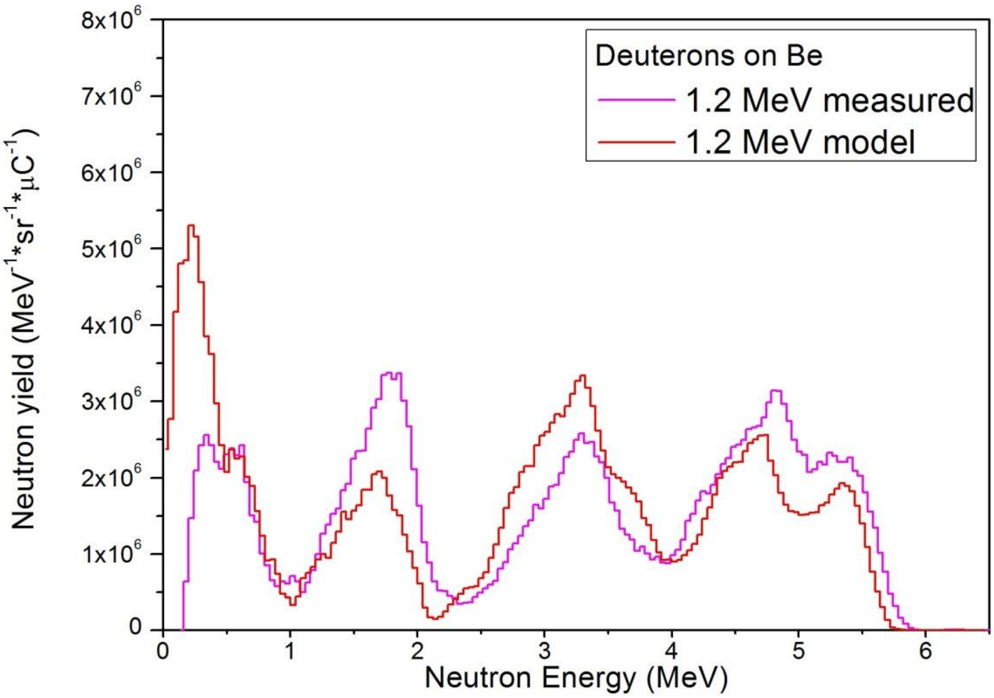

Fig.VI.17: Comparison between energy distribution of the yield of neutrons; 1.2 MeV deuterons simulated (red) and measured (violet).

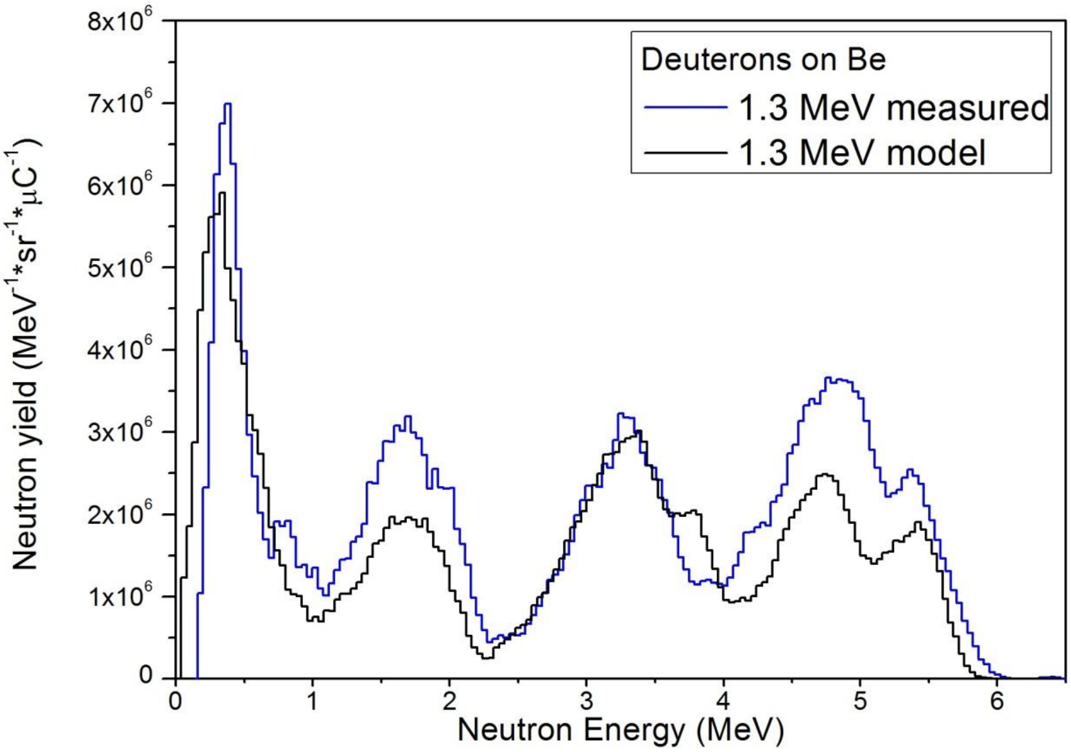

Fig.VI.18: Comparison between energy distribution of the yield of neutrons; 1.3 MeV deuterons simulated (black) and measured (blue).

It is important to underline that the simulated distributions were calculated by considering equally probable neutron energy groups, due to the lack of information about the actual cross section of the different reaction channels.

As for the ^{9}Be(p,xn)^{9}B, all the ^{9}Be(d,n)^{10}B spectra measured by the ACSpect were acquired directly in real-time.

CONCLUSIONS

At present, no instruments allow to perform real-time direct spectrometry with high resolution using a compact device.

In order to develop a spectrometer able to reach these targets, an innovative detection system based on the recoil-proton method was proposed.

The basic idea was to use a converter constituted by a plastic scintillator able to measure the energy released in the converter itself by recoil-protons generated by impinging neutrons. A monolithic silicon telescope, which measures the residual proton energy (ΔE stage and E stage) and discriminates gammas from neutrons, is placed at a proper distance from the scintillator in order to limit the detection to protons emitted at small angles. Event-by-event, the sum of the energy deposited in each stage gives the total energy of the recoil-proton, therefore the energy of the impinging neutron (since the emission angle is fixed).

A model of the system was developed in order to better understand the system behavior of a recoil-proton spectrometer based on a monolithic silicon telescope. This model takes into account all different stages, calculates the energy depositions and the final neutron spectra. The model allowed to verify the promising performances of the proposed spectrometer.

Two different types of photomultipliers were studied in order to characterize the first stage of the ACSpect. The SiPM proved to have worse resolution and to be very sensitive to radiation damage, therefore a PMT has been selected.

An innovative procedure for event discrimination was developed, exploiting the MST structure and the time-energy correlation between the three stages, leading to an effective proton selection. Another innovative procedure was developed to manage the non-linear behavior of the plastic scintillator. By combining the information measured by the PMT and E_{TOT}, it calculates the total energy of the recoil-proton. These two procedures, together with the optimized layout of the system, are the key of the achieved results of the ACSpect.

The system was tested with monoenergetic neutrons, proving its linear behavior and a FWHM of 235 keV at 3.309 MeV (7.1% of resolution).

A three-stages neutron spectrometer, operating in vacuum, for direct spectrometry was proposed in 2010 by Tomita et Al.. This system proved to obtain a resolution of ~200 keV and a detection efficiency of 10-^{7}-10-^{6} counts per neutron. To obtain this results, the system needs a very thin plastic converter (100 μm) and a large overall system, compared to the ACSpect (2 mm of converter, 122x173x51 mm of overall vessel).

The measurements performed with continuously distributed neutrons generated by protons on a Beryllium target showed a good agreement with literature data obtained through time-of-flight techniques.

The measured distribution of neutrons generated by deuterons on Beryllium showed a good consistency with literature time-of-flight data.

The ACSpect proved to be a simple and compact system, capable to perform direct real-time neutron spectrometry with a satisfactory resolution.

REFERENCES

[1] F.D. Brooks, H. Klein, *Neutron spectrometry – Historical review and present status*, Nucl. Instrum. Meth. A 476 (2002) 1-11.

[2] R. Böttger, H. Klein, A. Chalupka, B. Strohmaier, *Investigation of the Spectral Fluence of Neutrons from Spontaneous Fission of* ^{252}*Cf by Means of Time-of-Flight Spectrometry*, Nucl. Sci. Eng. 106 (3) (1990) 377-398.

[3] N. Colonna, G. Tagliente., *Response of liquid scintillator detectors to neutrons of En <1 MeV*, Nucl. Instrum. Meth., A 416 (1998) 109-114.

[4] J. Pulpan, M. Kralik, Nucl. Instrum. Meth. A 321 (1992) 223.

[5] S. Meigo, H. Takada, S. Chiba, et al., Nucl. Instrum. Meth. A 431 (1999) 521.

[6] T. Elevant, P. Van Belle, O.N. Jarvis, G. Sadler, Nucl. Instrum. Meth. A 364 (1995) 333.

[7] C. Manduchi, C. Ciricillo, E. Milli, S. Salviato, Nucl. Instrum. Meth. A 361 (1995) 548.

[8] T. Kurosawa, T. Nakamura, N. Nakao, et al., Nucl. Instrum. Meth. A 430 (1999) 400.

[9] T. Elevant, Nucl. Instrum. Meth. A 476 (2002) 485.

[10] W.B. Howard, S.M. Grimes, T.N. Massey, S.I. Al-Quraishi, D.K. Jacobs, C.E. Brient, J.C. Yanch, J.C., *Measurement of the Thick-Target* ^{9}*Be(p,n) Neutron Energy Spectra*, Nucl. Sci. Engin. 138(2) (2001) 145-160.

[11] R.L. Bramblett, R.I. Ewing, T.W. Bonner, *A new type of neutron spectrometer*, Nucl. Instrum. Meth. 9 (1960) 1-12.

[12] H. Toyokawa, A. Uritani, C. Mori, N. Takeda, K. Kudo, Radiat. Prot. Dosim. 70 (1997) 365.

[13] S. Yamaguchi, A. Uritani, H. Sakai, et al., Nucl. Instrum. Meth. A 422 (1999) 600.

[14] R. Bedogni, D. Bortot, A. Pola, M.V. Introini, A. Gentile, A. Esposito, J.M. Gómez-Ros, M. Palomba, A. Grossi, *A new active thermal neutron detector*, Radiat. Prot. Dosim. (2013).

[15] A. Pola, D. Bortot, M.V. Introini, R. Bedogni, A. Gentile, A. Esposito, J.M. Gómez-Ros, E. Passoth, A. Prokofiev, *Compact thermal neutron sensors for moderator-based neutron spectrometers*, Radiat. Prot. Dosim. (2013).

[16] R. Bedogni, J.M. Gómez-Ros, D. Bortot, A. Pola, M.V. Introini, A. Esposito, A. Gentile, G. Mazzitelli, B. Buonomo, *Development of single-exposure, multidetector neutron spectrometers: the NESCOFI@BTF project*, Radiat. Prot. Dosim. (2013).

[17] B. Wiegel, A.V. Alevra, *NEMUS - The PTB Neutron Multisphere Spectrometer: Bonner Spheres and More*, Nucl. Instrum. Meth. A 476 (2002) 36-41.

[18] B. Wiegel, A.V. Alevra, B.R.L. Siebert, *Calculations of the Response Functions of Bonner Spheres with a Spherical* ^{3}*He Proportional Counter Using a Realistic Detector Model*, PTB-Bericht PTB-N-21 (1994).

[19] G. Pichenot, B. Asselineau, O. Besida, et al., Nucl. Instrum. Meth. A 476 (2002) 165.

[20] H. Ing, T. Clifford, T. McLean, et al., Radiat. Prot. Dosim. 70 (1997) 273-278.

[21] W. Rosenstock, T. Koble, G. Kruzinski, G. Jaunich, Radiat. Prot. Dosim. 70 (1997) 299.

[22] J.A. Harvey, N.W. Hill, *Scintillation detectors for fast neutron physics*, Nucl. Instrum. Meth. 162 (1979) 507-530.

[23] H. Klein, S. Neumann, *Neutron and photon spectrometry with liquid scintillation detectors in mixed fields*, Nucl. Instrum. Meth. A 476 (2002) 132-142.

[24] R. Nolte, H.J. Brede, U.J. Schrewe, H. Schuhmacher, *Neutron spectrometry with liquid scintillation detectors at neutron energies between 20 and 70 MeV: a status report*, PTB Braunschweig Report PTB-N-9, 1993.

[25] S. Meigo, *Measurements of the response function and the detection effciency of an NE213 scintillator for neutrons between 20 and 65 MeV*, Nucl. Instrum. Meth. A 401, 365 (1997).

[26] H. Schuhmacher, H.J. Brede, V. Dangendorf, et al., Nucl. Instrum. Meth. A 421 (1999) 284.

[27] Physics, Part 1, Interscience, New York (1960) 387-411.

[28] J.B. Czirr and G. L. Jensen, *A compact neutron coincidence spectrometer, its measured response functions and potential applications*, Nucl. Instrum. Meth. A 349 (1994) 532.

[29] E.A. Kamykowski, *Comparison of calculated and measured spectral response and intrinsic efficiency for a boron-loaded plastic neutron detector*, Nucl. Instrum. Meth. A 317 (1992) 559.

[30] T. Aoyama, K. Honda, C. Mori, K. Kudo, N. Takeda, Nucl. Instrum. Meth. A 333 (1993) 492.

[31] A. Bertin, M. Bruschi, V.M. Bystritsky, et al., *Performances of a Coincidence Neutron Spectrometer with Double Pulse-Shape Discrimination*, Nucl. Instrum. Meth. A 337 (1994) 445.

[32] R. Aleksan, J. Bouchez, M. Cribier et al, *Measurement of fast neutrons in the Gran Sasso laboratory*, Nucl. Instrum. Meth. A 274 (1989) 203-206.

[33] S. Agosteo, G. D’Angelo, A. Fazzi, A. Foglio Para, A. Pola, P. Zotto, *Neutron Spectrometry with a Monolithic Silicon Telescope*. Radiat. Prot. Dosim. 126 (2007) 210-217.

[34] S. Agosteo, P. Colautti, J. Esposito, A. Fazzi, M.V. Introini, A. Pola, *Characterization of the energy distribution of neutrons generated by 5 MeV protons on a thick beryllium target at different emission angles*, Appl. Radiat. Isot. 69 (12) (2011) 1664-1667.

[35] S. Tudisco, F. Amorini, M. Cabibbo, G. Cardella, G. De Geronimo, A. Di Pietro, G. Fallica, P. Figuera, A. Musumarra, M. Papa, G. Pappalardo, F. Rizzo, G. Valvo, *A new large area monolithic silicon telescope*, Nucl. Instrum. Meth. A 426 (1999) 436-445.

[36] S. Agosteo, A. Pola, *Analytical Model for a Monolithic Silicon Telescope. Response Function of the E Stage*, Radiat. Meas. 43 (2008) 1487- 1492.

[37] International Commission on Radiation Units, *Stopping Power and Ranges for Protons and Alpha Particles (Report 49)*, ICRU, Bethesda, MD (1993).

[38] J.F. Ziegler, J.P. Biersack, SRIM 2008, IBM (2008), www.srim.org

[39] J.F. Ziegler, J.P. Biersack, U. Littmark, *The Stopping and Range of Ions in Solids*, Pergamon Press, New York (1985).

[40] V. Montarese, *Studio di Fattibilità di uno Spettrometro Neutronico con Convertitore Attivo*, Master Thesis, Politecnico di Milano, Dipartimento di Energia, Sezione di Ingegneria Nucleare (2011) (ITALIAN).

[41] S. Agosteo, A Foglio Para, *Metrology and Spectrometry of Neutrons in the MeV Range by Standard Photodiodes*, Proceedings of SIMAI 2002, VI Congresso Nazionale della Società Italiana di Matematica Applicata e Industriale, Chia, Italy, (2002).

[42] A. Pola, *Semiconductor detectors for neutron spectrometry and microdosimetry*, PhD. Thesis, Politecnico di Milano, Dipartimento di Ingegneria Nucleare (2006).

[43] Saint-Gobain Crystals, www.crystals.saint-gobain.com/Plastic_Scintillators.aspx, Plastic Product Brochure.

[44] Saint-Gobain Crystals, www.crystals.saint-gobain.com/Plastic_Scintillators.aspx, BC-404 scintillator.

[45] www.hamamatsu.com/eu/en/product/category/3100/3003/3044/H10720-110/index.html

[46] www.hamamatsu.com/eu/en/product/category/3100/3001/R9880U-110/index.html

[47] M. Ghioni, A. Gulinatti, I. Rech, F. Zappa and S. Cova, *Progress in Silicon Single-Photon Avalanche Diodes*, IEEE J. Sel. Topics Qantum Electron., vol. 13, no. 4, 852-862 (2007).

[48] F. Zappa, S. Tisa, A. Tosi, S. Cova, *Principles and features of single-photon avalanche diode arrays*, Sensors and Actuators A: Physical 01/2007 (2007).

[49] S.M. Sze, *Physics of Semiconductor Devices*, J. Wiley and Sons, 1981.

[50] G.F. Knoll, *Radiation detection and measurement 4th ed.*, New York, John Wiley and Sons (2010).

[51] D. Renker, *Geiger-mode avalanche photodiodes, history, properties and problems*, Nucl. Intrum. Meth., A 567 (2006) 48-56.

[52] S. Cova, et al., NIST workshop on Single Photon Detectors (2003).

[53] National Instrument LabVIEW, www.ni.com/labview

[54] J.B. Birks, Proc. Phys. Soc. A64: 874 (1951).

[55] J.B. Birks, The Theory and Practice of Scintillation Counting, London: Pergamon (1964).

[56] L. Torrisi, *Plastic scintillator investigations for relative dosimetry in proton-therapy*, Nucl. Instrum. Meth. B 523 (2000) 161-170.

[57] www.cremat.com/CR-110.pdf

[58] cremat.com/CR-150.htm

[59] www.picotech.com

[60] H. Tomita, H. Iwai, T. Iguchi, M. Isobe, J. Kawarabayashi, C. Konno, Development of neutron spectrometer toward deuterium plasma diagnostics in LHD, Review of Scientific Instruments 81, 10D309 (2010).

[61] C. Ceballos, J. Esposito, *The BSA modelling for the accelerator-based BNCT facility at INFN LNL for treating shallow skin melanoma*, Appl. Radiat. Isot. 67 (7-8) (2009) S274 – S277.

[62] M.E. Capoulat, D.M. Minsky, A.J. Kreiner, M.V. Introini, A. Pola, M. Lorenzoli, S. Agosteo, *Measurement of the Double-Differential Neutron Yield of the* ${}^{9}Be(d,n)^{10}B$ *Reaction in the Low Bombarding Energy Regime*, LNL Annual Report 2012, INFN-LNL-239 (2013) 45-46.

[63] M.E. Capoulat, D.M. Minsky, A.J. Kreiner, *Applicability of the* ${}^{9}Be(d,n)^{10}B$ *reaction to AB-BNCT skin and deep tumor treatment*, Appl. Radiat. Isot. 69 (2011) 1684-1687.

[64] M.E. Capoulat, et. al., Proceedings of the 6º Young Researchers BNCT Meeting (2011) 33.

[65] M.S. Herrera, M.E. Capoulat, S.J. González et al., 15º International Congress on Neutron Capture Therapy, Tsukuba, Japan (2012).

[66] J. Guzek, *Elemental Radiography Using Fast Neutron Beams*, University of the Witwatersrand PhD. Thesis (1999).

[67] M.A. Lone, C.B. Bingham, J.S. Fraser, H.R. Schneider, T.K. Alexander, A.J. Fergusson, A.B. McDonald, *Thick target neutron yields and spectral distributions from the* ${}^{7}Li({}^{d}_{p},n)$*and* ${}^{9}Be({}^{d}_{p},n)$ *reactions*, Nucl. Instrum. Meth. 143 (1977) 331-344.

[68] M.A. Lone, A.J. Fergusson, B.S. Robertson, *Characteristics of Neutrons from Be Targets Bombarded with Protons, Deuterons and Alpha Particles*, Nucl. Instrum. Meth. 189 (1981) 515-523.

[69] T. Inada, K. Kawachi, T. Hiramoto, *Neutrons from Thick Target Beryllium (d,n) Reactions at 1.0 MeV to 3.0 MeV*, J. Nucl. Sci. Tech., Vol. 5(1) 22-29 (1968).

[70] S. Whittlestone, *Neutron Distribution from the Deuteron Bombardment of a Thick Beryllium Target*J. Phys. D: Appl. Phys., Vol 10 1715-1723 (1977).

[71] D.L. Smith, J.W. Meadows, P.T. Guenther, *Neutron Emission from the* ${}^{9}Be(d,n)^{10}B$ *Thick-Target Reaction for 7 MeV Deuterons*, Nucl. Instrum. Meth. A 241 (1985) 507-510.

[72] D.L. Smith, J.W. Meadows, P.T. Guenther, *Neutron Emission from the* $^{9}Be(d,n)^{10}B$ *Thick-Target Reaction for 7 MeV Deuterons*, Nucl. Instrum. Meth. A 241 (1985) 507-510.

[73] F.M. Baumann, G. Domogala, H. Freiesleben, H.J. Paul, S. Puhlvers, H. Sohlbah, *The* $^{9}Be(d,n)^{10}B$ *Reaction as Intense Neutron Source with Continuous Energy Spectrum*, Nucl. Instrum. Meth. A 247 (1986) 359-366.

[74] H.J. Brede, G. Dietze, K. Kudo, U.J. Schrewe, F. Tancu, C. Wen, *Neutrons yield from thick Be targets bombarded with deuterons or protons*, Nucl. Instrum. Meth. A 274 (1989) 332-344.

[75] J.W. Meadows, *The* $^{9}Be(d,n)^{10}B$ *Thick Target Neutron Spectra for Deuterons Energies Between 2.6 and 7.0 MeV*, Nucl. Instrum. Meth. A 324 (1993) 239-246.

[76] J. Guzek, U.A.S. Tapper, W.R. McMurray, J.I.W. Watterson, *Characterization of the* $^{9}Be(d,n)^{10}B$ *reaction as a source of neutrons employing commercially available radio frequency (RFQ) quadrupole linacs*, Proceedings International Conference Neutrons in Research and Industry, 9-15 June 1996, Crete, Greece, Vol. 2867 509-512 (1996).

[77] J.I.W. Watterson, R.C. Lanza, J. Guzek, W.R. McMurray, E. Iverson, U.A.S. Tapper, *Small deuteron accelerator as a source of slow neutrons*, Proceedings International Conference Neutrons in Research and Industry, 9-15 June 1996, Crete, Greece, Vol. 2867 533-536 (1996).

[78] www.nndc.bnl.gov/nudat2/